Three-dimensional simulations of magneto-convection in the solar photosphere

Dissertation
zur Erlangung des Doktorgrades
der Mathematisch-Naturwissenschaftlichen Fakultäten
der Georg-August-Universität zu Göttingen

vorgelegt von
Alexander Vögler
aus Fulda

Göttingen 2003

Bibliographische Information Der Deutschen Bibliothek
Die Deutsche Bibliothek verzeichnet diese Publikation in der Deutschen Nationalbibliographie; detaillierte bibliographische Daten sind im Internet über `http://dnb.ddb.de` abrufbar.

Copyright © Copernicus GmbH 2004

ISBN 3-936586-26-8

Copernicus GmbH, Katlenburg-Lindau
Satz & Coverdesign: Alexander Vögler
Druck: Schaltungsdienst Lange, Berlin

Printed in Germany

D7

Referent:	Prof. Dr. F. Kneer
Korreferent:	Prof. Dr. M. Schüssler
Tag der mündlichen Prüfung:	11.7.2003

Contents

Summary **1**

1 Introduction **3**

2 The equations of radiative MHD **8**
- 2.1 Basic assumptions of magnetohydrodynamics . . . 8
- 2.2 The MHD equations . . . 11
- 2.3 The equation of state . . . 13
- 2.4 The radiative source term . . . 15

3 The MHD code **18**
- 3.1 Spatial discretization and parallelization . . . 19
- 3.2 Temporal discretization . . . 21
- 3.3 Artificial diffusivities . . . 23
- 3.4 Boundary conditions . . . 26
  - 3.4.1 Upper boundary . . . 26
  - 3.4.2 Lower boundary . . . 28
  - 3.4.3 Side boundaries . . . 32

4 Numerical radiative transfer **34**
- 4.1 The numerical scheme . . . 34
- 4.2 Numerical treatment of frequency dependence . . . 41
  - 4.2.1 Opacity distribution functions . . . 42
  - 4.2.2 The opacity binning method . . . 46
- 4.3 Tests of the opacity binning method . . . 50
  - 4.3.1 1D tests . . . 51
  - 4.3.2 Results of 2D calculations . . . 60
  - 4.3.3 The opacity binning method in the limit of a large number of bins . . . 65
  - 4.3.4 Error timescales . . . 73

5 Results of simulation runs **76**
- 5.1 “Plage” run with $B_0 = 200$ G . . . 78

5.1.1 Morphology and statistical properties 78
5.1.2 Relation between magnetic field strength and emergent intensity 90
5.2 Simulation runs with B_0 =10 G and 50 G 100
5.3 Effects of non-grey radiative transfer 106

6 Outlook 113

References 115

Danksagung 121

Lebenslauf 123

Summary

In this thesis, three-dimensional numerical simulations were carried out in order to study the interaction between convective flows and magnetic fields in the photosphere of the Sun.

- An already existing MHD code was modified and extended in order to adapt it to the requirements of realistic solar simulations. A radiative transfer module was developed, which solves the radiative transfer equation under the assumption of local thermal equilibrium and accounts for the frequency dependence by means of opacity binning. Further modifications were made regarding the inclusion of partial ionization effects, the development of an open lower boundary condition, and the stabilization of the numerical scheme in simulations of strongly stratified media using the concept of hyperdiffusivities.

- Tests of the opacity-binning method used to approximate the frequency dependence of the radiative transfer were carried out, which assessed the quality of the approximation in realistic situations and confirmed the applicability of the method in multidimensional simulations.

- The simulation of a typical solar “plage” region with an average magnetic field strength of 200 Gauss in a box extending 6 Mm in both horizontal and 1.4 Mm in the vertical direction shows the amplification of a homogeneous initial field and the formation of a magnetic network embedded in the network of intergranular downflows. The magnetic field forms thin, sheet-like structures as well as micropores with diameters up to 1000 km and maximum field strengths around 2000 Gauss. Morphology, time evolution, and statistical properties of magnetic structures are analyzed and the relation between field strength and brightness of magnetic features is studied.

- A comparison of simulations using the frequency dependent (“non-grey”) radiative transfer with “grey” simulations shows that the non-grey effects lead to a significant reduction of temperature fluctuations in the upper photosphere and enhance the heating of magnetic elements due to the increased absorption of “hot” radiation.

Chapter 1

Introduction

The term "magneto-convection" is commonly used to describe physical processes resulting from the interaction of convective flows with a magnetic field in an electrically well-conducting fluid. In the solar photosphere and convection zone, the low values of viscosity and magnetic diffusivity lead to high (hydrodynamic and magnetic) Reynolds numbers and give rise to highly nonlinear dynamics and the formation of structures and patterns on a large range of length- and timescales. The hierarchy of magnetic structures in the photosphere ranges from sunspots with umbral field strenghts around 3000 G, diameters of up to 30000 km and lifetimes of weeks, to small-scale magnetic elements in the magnetic network of the "quiet Sun" with sizes smaller than 100 km and field strengths around 1500 G, which evolve on the timescale of a few minutes. From the point of view of theoretical magneto-convection, the relevant processes connected with these structures include, among others, the spatial distribution of magnetic field and formation of intermittent structures by means of flux expulsion, the generation of magnetic flux by turbulent fast-dynamo action, the supression of convective energy transport by magnetic fields, and the dynamics of wave excitation, instabilities and magnetic reconnection.

Based on the seminal studies of linear stability of thermal magneto-convection by Chandrasekhar (1961), two branches of numerical research in the field of solar magneto-convection have developed. The first branch, using highly idealized models which do not aim at an approximation of solar conditions, was developed out of sheer necessity, since the limitation of computing power at that time made a simplification of models mandatory. With the advent of ever more powerful computers in the 1980s, a second line of research emerged, which attempts to model the physical processes on the Sun as realistically as possible. Despite of the progress made in the field of realistic simulations, idealized studies have, until the present day, not lost their relevance. While they cannot be compared directly to observations, they allow to isolate certain physical processes and are amenable to analytical tools like linear stability analysis and bifurcation theory, thus providing valuable insight into the underlying physical mechanisms.

The application of the theory of magneto-convection on solar phenomena was pioneered by Parker (1963), who pointed out that the observed supergranular network of magnetic fields can be understood in terms of magnetic flux transported into the the downflow lanes of a cellular flow pattern. The first time-dependent numerical simulation of magneto-convection was carried out by Weiss (1966). His purely kinematic model (neglecting the backreaction of the Lorentz force on the fluid) showed how horizontal flows concentrate a vertical field in the up- and downflow regions of a prescribed cellular flow field. The system reaches a steady state which is characterized by the balance between advection and diffusion.

Galloway et al. (1977) extended the studies to the dynamical regime. Their axisymmetric simulations of thermal convection in the (quasi-incompressible) Boussinesq approximation showed that the magnetic field forms a flux tube in the downflow region near the symmetry axis. The Lorentz force suppresses the fluid motions the flux tube, resulting in a separation of strong fields and motions.

Hurlburt & Toomre (1988) took into account the effects of compressibility. Using a two-dimensional Cartesian box, they simulated the flux-expulsion process in a stratified medium extending over a few pressure scale heights. Since hot upwellings expand while the cooler and denser falling material contracts, the inclusion of compressibility breaks the symmetry between up- and downflows. The pressure maxima occuring both over up- and downflows are associated with an increase in density, which works against buoyancy in upflows ("buoyancy breaking") and cooperates in downflows, thus enhancing the asymmetry. Since the vertical magnetic field residing in downflow regions suppresses horizontal motions while leaving vertical velocities unaffected, the upper part of a flux sheet becomes partially evacuated during its formation, and the compression by the external pressure forces further increases the field strength.

In a more recent study, Tao et al. (1998) considered strongly nonlinear compressible magneto-convection (with a Rayleigh number of $Ra = 10^5$) in a wide three-dimensional simulation box. They find a separation in two "phases": most of the magnetic flux gathers to form regions of strong field interspersed with weak small-scale motions in the form of small convective plumes. The remaining part of the box is occupied by weakly magnetized, extended upflow plumes separated by narrow downflow lanes, a situation not unlike the difference in appearance of granular patterns in "quiet Sun" and "plage" regions.

Cattaneo et al. (2003) conducted an extensive parameter study of three-dimensional thermal magneto-convection in the Boussinesq approximation. The simulations were carried out in the turbulent regime with high Rayleigh numbers ($Ra = 5 \cdot 10^5$), requiring a correspondingly high grid resolution of $512 \times 512 \times 97$. Depending on the amount of magnetic flux imposed, the solutions show a large variety of magnetic structures and flow patterns, from the dynamo regime (zero mean field) with small-scale field concentrations formed in the downflow network as the result of turbulent fast-dynamo action, to magnetically dominated convection in the strong-field regime. For a comprehensive overview over the field of idealized simulations, the reader is referred to the reviews by Proctor & Weiss (1982), Proctor (1992) and Weiss (1997).

In contrast to these idealized simulations, “realistic” simulations include elaborate physics like radiative transfer, partial ionization, and “open” boundary conditions in order to approximate the real Sun. The analysis of such simulations with tools for spectral line and polarization diagnostics allows us to directly relate the results to observations. In one respect, however, all “realistic” simulations fail to model the solar conditions. As a consequence of the low values of the actual diffusivities, it is impossible to resolve the diffusive length scales (of the order of centimeters for the viscous scale) and, at the same time, capture the spatial extent of the structures of interest (several megameters). For this reason, all realistic simulations are effectively large-eddy simulations, which, in one way or the other, parametrize the effects of the sub-grid scales, hopefully providing a realistic description of their influence on the resolved scales.

The earliest realistic 3D simulations were carried out by Nordlund (1983), who imposed an external magnetic field on a three-dimensional simulation of solar granulation, including non-grey radiative transfer, the anelastic approximation and a rather low horizontal resolution of 250 km. This simulation illustrated the tendency of magnetic field to be swept into the intergranular downflow lanes, where it is constantly redistributed.

Fully compressible simulations by Nordlund & Stein (1990) with improved horizontal resolution of 50 km showed that a strong field (500 G on average) has a stabilizing effect on the downflow network, which tends to fragment and form isolated downdrafts in the absence of fields. Bercik et al. (1998) extended this study by varying both the strength and the orientation of the imposed magnetic field. They find a transition from normal granulation to “abnormal” granulation with pore-like structures. In a more recent simulation with a rather coarse horizontal resolution of 100 km, Stein et al. (2002) studied the details of micropore formation. The results show, how micropores are formed at downflow vertices as a result of magnetic flux converging on a shrinking granule.

The process of convective intensification of magnetic field was studied in more detail by Grossmann-Doerth et al. (1998), who found clear signatures of the “convective collapse” process (e.g. Parker 1978, Spruit 1979) in two-dimensional high-resolution simulations including radiative transfer. The growing magnetic field supresses the lateral convective influx of energy into the flux sheet; as a result, the radiative cooling cannot be balanced and the ensuing enhancement of superadiabaticity drives a strong downflow, which leads to partial evacuation and field amplification.

While the studies mentioned so far investigated the formation of magnetic structures and the process of field intensification, other simulations focused on the structure and dynamics of already formed magnetic elements. Deinzer et al. (1984a,b) carried out two-dimensional simulations of flux sheets, using an adaptive mesh in order to resolve steep gradients at the sheet's edges, with radiation in the diffusion approximation. The results show that the interior of the sheet is heated by inflow of radiation from the hot walls, while the cooling immediately outside drives a baroclinic flow in form of a strong downflow jet.

Knölker & Schüssler (1988) varied the width of the sheets and found that the brightness (vertical emergent intensity) of magnetic elements decreases with increasing size; structures larger than 500 km appear darker than the average intensity, the intensity emerging along oblique rays is, however, increased.

Employing tools for spectral and polarization diagnostics, Knölker et al. (1991) and Grossmann-Doerth et al. (1994) used two-dimensional simulations with full (grey) radiative transfer as the basis for calculating synthetic line profiles of polarized light ("Stokes-V profiles"). They found that observed Stokes-V profiles of plage and network fields, which show a distinct area asymmetry in combination with a negligible zero-crossing Doppler shift, can be explained in terms of a static magnetic element, which expands with height and is surrounded by nonmagnetic downflows ("canopy effect"). Their simulation results also illustrated the effect of radiative illumination of the sheet's interior by absorption of "hot" radiation from the bottom and walls.

Two-dimensional high-resolution simulations by Steiner et al. (1998) revealed details of the complex interaction of a flux sheet with its surroundings. The stochastic forces exerted by the convective motions can induce a strong horizontal swaying and bending of the sheet; occasional compressions of the sheet lead to upflows inside, which can steepen to form shocks with a characteristic signature in synthesized Stokes-V profiles.

Using a different two-dimensional code, Gadun et al. (2001) carried out simulations with an initial field of mixed polarity. The results show a permanent transformation of strong vertical into weak horizontal field and vice versa. The authors relate this process of flux "recycling" to observed emergence rates of small-scale flux in the quiet Sun.

The work presented here follows the line of realistic modelling. The main goal of this PhD project was to develop a three-dimensional MHD simulation code for applications in the solar photosphere and convection zone, which meets the requirements of realistic simulations and is designed for use on parallel computers. Building on an existing MHD code developed at the University of Chicago, several extensions and modifications were added to adapt the code to the conditions of the solar photosphere. The most important modification was the development of a radiative transfer module which calculates the heating and cooling of the plasma due to the interaction with radiation. An accurate modelling of this energy exchange is of crucial importance in the photospheric layers, where the transition from convective to radiative energy transport takes places. Emphasis was placed on an adequate representation of the frequency dependence of the radiative transfer, in order to include the effects of spectral lines ("non-grey" effects), which have important consequences for the temperature structure of the upper photosphere.

Chapter 2 presents a brief overview over the basic physics of radiative magneto-hydrodynamics and the system of equations solved by the code. In Chapter 3 the numerical methods employed by the MHD code are discussed. Chapter 4 is devoted to the numerical treatment of the radiative transfer, with particular emphasis on the strategies to approximate the frequency dependence. Apart from a description of the numerical methods, we present test calculations, which confirm the applicability of the non-grey approximation in simulations. In Chapter 5, the first simulation results obtained with the code are presented and the relevance of the non-grey radiative transfer for the results is assessed.

Chapter 2

The equations of radiative magnetohydrodynamics

2.1 Basic assumptions of magnetohydrodynamics

The simplest way of describing a plasma and its interaction with electric and magnetic fields is the *magnetohydrodynamic approximation* (MHD), which combines the equations of hydrodynamics with the pre-Maxwell equations. Starting from the Maxwell equations

$$\nabla \times \mathbf{B} = \frac{4\pi}{c}\mathbf{j} + \frac{1}{c}\frac{\partial \mathbf{E}}{\partial t} \tag{2.1}$$

$$\nabla \times \mathbf{E} = -\frac{1}{c}\frac{\partial \mathbf{B}}{\partial t} \tag{2.2}$$

$$\nabla \cdot \mathbf{E} = 4\pi\varrho \tag{2.3}$$

$$\nabla \cdot \mathbf{B} = 0 \tag{2.4}$$

with the electric field $\mathbf{E}$, the magnetic field $\mathbf{B}$, current density $\mathbf{j}$ and electrical charge density ϱ, the following assumptions are made:

(a) The fluid motions are non-relativistic, i.e.

$$\frac{v}{c} \ll 1 \tag{2.5}$$

and under change of the reference frame $\mathbf{E}$ and $\mathbf{B}$ transform according to

$$\mathbf{E}' = \mathbf{E} + \frac{1}{c}\mathbf{v} \times \mathbf{B} \tag{2.6}$$

$$\mathbf{B}' = \mathbf{B} - \frac{1}{c}\mathbf{v} \times \mathbf{E}, \tag{2.7}$$

where $\mathbf{v}$ is the relative velocity between the two frames of reference.

(b) Let L and T be typical spatial and temporal scales on which a quantity changes; then

$$\frac{L/T}{c} \ll 1 \tag{2.8}$$

holds. This implies that all phase velocities are non-relativistic, hence electromagnetic waves do not occur in MHD.

(c) The plasma is assumed to be highly conducting and charge-neutral. In plasmas charge separation is negligible as long as only spatial and temporal scales much larger than the Debye length $\lambda_D = (kT/8\pi n_e e^2)^{1/2}$ and the inverse plasma frequency $\omega_p^{-1} = (m_e/4\pi e^2 n_e)^{1/2}$, respectively, are considered. For typical photospheric values $T = 5 \cdot 10^3$ K and $n_e = 10^{14}$ cm^{-3} one has $\lambda_D \simeq 10^{-4}$ cm and $\omega_p^{-1} \simeq 10^{-11}$ s. Since the photospheric length- and timescales of interest exceed these values by many orders of magnitude, the assumption of charge-neutrality is justified. Owing to the high electrical conductivity electric fields are negligible. Formally, this follows from an order-of-magnitude estimate of Eq. (2.2), which governs the electric field in the absence of free charges:

$$\frac{E}{L} \approx \frac{B}{cT}, \tag{2.9}$$

hence

$$\frac{E}{B} \approx \frac{L}{cT} \ll 1\ . \tag{2.10}$$

In MHD, terms which are of second order in small quantities are neglected. From Eq. (2.1) an estimate of the displacement current yields

$$\frac{\left|\dot{\mathbf{E}}/c\right|}{|\nabla \times \mathbf{B}|} \approx \frac{E/T}{cB/L} \approx \frac{E}{B}\frac{L}{cT} \approx \left(\frac{E}{B}\right)^2 \ll 1\ . \tag{2.11}$$

Dropping the displacement current, $\dot{\mathbf{E}}/c$, Eq. (2.1) becomes

$$\nabla \times \mathbf{B} = \frac{4\pi}{c}\mathbf{j}\ . \tag{2.12}$$

Likewise, the $\mathbf{v} \times \mathbf{E}$ term in Eq. (2.7) is dropped, as follows from

$$\frac{|\mathbf{v} \times \mathbf{E}|}{c\,|\mathbf{B}|} \approx \frac{v}{c}\frac{E}{B} \ll 1\,. \tag{2.13}$$

The transformation law Eq. (2.7) then reads

$$\mathbf{B}' = \mathbf{B}\,. \tag{2.14}$$

One further assumes that in the rest frame of the fluid (denoted by primed quantities) Ohm's law $\mathbf{j}' = \sigma\mathbf{E}'$ holds (σ is the electrical conductivity). From Eqs. (2.12) and (2.14) one has

$$\mathbf{j}' = \mathbf{j}, \tag{2.15}$$

and with Eq. (2.6) Ohm's law in a moving reference frame reads

$$\mathbf{j} = \sigma(\mathbf{E} + \frac{1}{c}\mathbf{v}\times\mathbf{B})\,. \tag{2.16}$$

Taking the curl of Eq. (2.16), substituting $\mathbf{j}$ and $\nabla\times\mathbf{E}$ from Eqs. (2.12) and (2.2), respectively, and defining the magnetic diffusivity $\eta = c^2/4\pi\sigma$, one obtains the *induction equation*

$$\frac{\partial\mathbf{B}}{\partial t} = \nabla\times(\mathbf{v}\times\mathbf{B}) - \nabla\times(\eta\nabla\times\mathbf{B}), \tag{2.17}$$

which governs the time evolution of the magnetic field for a given velocity field, $\mathbf{v}$. The first term on the r.h.s. describes the inductive effect of the velocity field, the second term accounts for diffusion of magnetic field due to the finite conductivity of the plasma. The order-of-magnitude estimate for the ratio of these terms is called *magnetic Reynolds number* R_m:

$$\frac{|\nabla\times(\mathbf{v}\times\mathbf{B})|}{|\nabla\times(\eta\nabla\times\mathbf{B})|} \approx \frac{VB/L}{\eta B/L^2} = VL/\eta =: R_m \tag{2.18}$$

Estimates for the photosphere and upper convection zone suggest magnetic Reynolds numbers of the order of $10^3 - 10^6$ (Stix 1989, p. 253), so the diffusion term is almost negligible in these regions. In the high-R_m regime *Alfven's theorem of flux-freezing* applies (e.g. Choudhuri 1998, p. 282): magnetic field lines are transported by the fluid as if frozen in and fluid motions relative to the magnetic field are possible only along the direction of field lines.

2.2 The MHD equations

According to the remarks made in the previous section, charge separation of the plasma can be neglected in the present context, and since we are not interested in the individual properties of the fluid's different components, a 1-fluid model is appropriate to describe the plasma. Consequently, the standard equations of hydrodynamics, with magnetic force and energy terms added, together with the induction equation for the magnetic field, constitute the complete set of MHD equations, stated here for a system in an inertial frame of reference with a constant gravitational acceleration:

The continuity equation

The continuity equation

$$\frac{\partial \varrho}{\partial t} + \nabla \cdot (\varrho \mathbf{v}) = 0 \tag{2.19}$$

represents mass conservation.

The equation of motion

$$\frac{\partial \varrho \mathbf{v}}{\partial t} + \nabla \cdot \left[\varrho \mathbf{v}\mathbf{v} + \left(p + \frac{|\mathbf{B}|^2}{8\pi} \right) \underline{\mathbf{1}} - \frac{\mathbf{B}\mathbf{B}}{4\pi} \right] = \varrho \mathbf{g} + \nabla \cdot \underline{\underline{\tau}} \, . \tag{2.20}$$

p is the gas pressure and $\mathbf{g}$ the gravitational acceleration. $\mathbf{vv}$ and $\mathbf{BB}$ are dyadic products and $\underline{\mathbf{1}}$ is the 3×3 unit matrix. Here the magnetic force (Lorentz force) has been split into the gradient of the magnetic pressure

$$p_{\mathrm{mag}} = \frac{|\mathbf{B}|^2}{8\pi}, \tag{2.21}$$

and the term $-\nabla \cdot (\mathbf{BB}/4\pi)$, which represents a tension along magnetic field lines. The last term on the r.h.s. of Eq. (2.20) is the viscous force. For a compressible gas, the components of the vicous stress tensor $\underline{\underline{\tau}}$ are given by

$$\tau_{ij} = \mu \left(\frac{\partial v_i}{\partial x_j} + \frac{\partial v_j}{\partial x_i} - \frac{2}{3} \, \delta_{ij} \, (\nabla \cdot \mathbf{v}) \right), \qquad i, j = 1, 2, 3 \tag{2.22}$$

where μ is the *dynamic viscosity.* The importance of the viscous term is measured by the *Reynolds number*, defined as the order-of-magnitude ratio of the advective and viscous terms in Eq. (2.20):

$$Re := \frac{\varrho V^2/L}{\mu V/L^2} = \frac{\varrho V L}{\mu} = \frac{V L}{\nu} \tag{2.23}$$

with the *kinematic viscosity*

$$\nu := \frac{\mu}{\varrho}. \tag{2.24}$$

Values for the Reynolds number in the solar photosphere have been estimated to be of the order of $Re \approx 10^8$ (e.g. Komm et al. 1991), so that viscous forces play a negligible role.
Rotational terms can be ignored in the momentum balance despite the fact that the Sun is a rotating system. This is justified since the effects of the Sun's rotation can be neglected on typical scales of solar granulation:

(i) the centrifugal acceleration $\mathbf{\Omega} \times (\mathbf{\Omega} \times \mathbf{r})$ is several orders of magnitude smaller than the gravitational acceleration in the photosphere:

$$\frac{|\mathbf{\Omega} \times (\mathbf{\Omega} \times \mathbf{r})|}{|\mathbf{g}|} \approx \frac{\Omega^2 R_\odot}{g_\odot} \approx 10^{-4} \tag{2.25}$$

with $\Omega \simeq 3 \cdot 10^{-6}\,\mathrm{s}^{-1}$, $R_\odot \simeq 7 \cdot 10^{10}$ cm and $g_\odot \simeq 2.74 \cdot 10^4\,\mathrm{cm\ s}^{-2}$.

(ii) for the typical length scales and velocities of solar granulation, the advection term in Eq. (2.20) is large compared to the Coriolis force term $-2\mathbf{\Omega} \times \mathbf{v}$. With $L \simeq 10^8$ cm and $V \simeq 10^5\,\mathrm{cm\ s}^{-1}$, the ratio of these two terms, the *Rossby number Ro*, is

$$Ro := \frac{V^2/L}{\Omega V} = \frac{V}{\Omega L} \approx 10^2 - 10^3\ . \tag{2.26}$$

The energy equation

$$\begin{aligned}\frac{\partial e}{\partial t} \ &+\ \nabla \cdot \left[\mathbf{v}\left(e + p + \frac{|\mathbf{B}|^2}{8\pi}\right) - \frac{1}{4\pi}\mathbf{B}(\mathbf{v} \cdot \mathbf{B})\right] \\ &=\ \frac{1}{4\pi}\nabla \cdot (\mathbf{B} \times \eta \nabla \times \mathbf{B}) \ +\ \nabla \cdot (\mathbf{v} \cdot \underline{\underline{\tau}}) \ +\ \nabla \cdot (K \nabla T) \\ &+\ \varrho(\mathbf{g} \cdot \mathbf{v}) \ +\ Q_{\mathrm{rad}}\ .\end{aligned} \tag{2.27}$$

Here the energy balance is stated for the total energy density per volume, e, which is the sum of internal, kinetic and magnetic energy densities: $e = e_{\mathrm{int}} + e_{\mathrm{kin}} + e_{\mathrm{mag}}$. T is the temperature and K the thermal conductivity. Q_{rad} is the radiative source term which accounts for heating and cooling due to the plasma's interaction with radiation. This term is discussed in detail in Sec. 2.4. Throughout the solar convection zone and photosphere, heat transfer due to thermal conduction is by far less efficient than both radiative heat transfer and convective energy transport. The former follows from the fact that the mean free path of photons is much larger than that of particles. The latter is expressed by the *Péclet number, Pe,* which is defined as the product of the *Prandtl number*

$$Pr := \frac{c_p \mu}{K} = \frac{\nu}{\kappa_{cd}} \tag{2.28}$$

(κ_{cd} being the thermal diffusivity due to conduction) and the Reynolds number:

$$Pe := Pr \cdot Re = \frac{\nu}{\kappa_{cd}} \cdot \frac{VL}{\nu} = \frac{VL}{\kappa_{cd}} \tag{2.29}$$

Pe measures the ratio of convective and conductive energy transport. The Prandtl number based on heat conduction is of the order of 10^{-3} (Choudhuri 1998, p. 398, with $c_p \simeq 10^9\,\mathrm{erg\,K^{-1}g^{-1}}$), and with $Re \approx 10^8$ one obtains $Pe \approx 10^5$, so that conductive heat transfer is negligible.[1]

The equation of state

In order to close the system of MHD equations (2.17), (2.19), (2.20) and (2.27), an equation of state which describes the relations between the thermodynamical quantities of the fluid must be specified. Since the MHD equations have been written with ϱ and e_{int} as the fundamental thermodynamical quantities whose time development is explicitly described, one needs relations which specify the other occurring thermodynamical quantities, namely T and p, as functions of ϱ and e_{int}:

$$T = T(\varrho, e_{\mathrm{int}}) \tag{2.30}$$

and

$$p = p(\varrho, e_{\mathrm{int}}) \tag{2.31}$$

2.3 Determining the equation of state

At temperatures typically encountered in the photosphere and convection zone, the solar plasma is partly ionized and the simple thermodynamical relations for an ideal gas do not apply. As hydrodynamical calculations have shown, the changes in the thermodynamical properties of the matter have considerable consequences for the character of convection. In the upper convection zone, about 2/3 of the enthalpy flux is transported by latent heat. Buoyancy driving is strongly enhanced since partial ionization reduces the adiabatic gradient ∇_{ad}, and the increase in specific heat tends to suppress the radiative damping of temperature fluctuations (Rast & Toomre 1993a,b, Rast et al. 1993).

In the following, a brief outline is given how temperature and pressure can be derived from e_{int} and ϱ, if only the first ionization of a number of elements is taken into account. For the simulations presented here, the eleven most abundant elements in the solar photosphere were included. The internal energy per mass unit $\varepsilon_{\mathrm{int}} = e_{\mathrm{int}}/\varrho$ can be written as

$$\varepsilon_{\mathrm{int}} = \frac{3}{2\varrho}\left(n_e + n_a\right) kT + \frac{1}{\varrho}\sum n_i^* \chi_i, \tag{2.32}$$

---

[1] In the solar context the definition of the Prandtl number is often based on the thermal diffusivity due to *radiation*. In this case estimates of Pr are much smaller and a typical value for the photosphere is $Pr \approx 10^{-8}$ (Komm et al. 1991).

AN	Name	ν_i	χ_i $[eV]$
1	H	0.934042096	13.600
2	He	0.064619943	24.580
6	C	0.000371849	11.256
7	N	0.000091278	14.529
8	O	0.000759218	13.614
12	Mg	0.000035511	7.644
11	Na	0.000001997	5.138
20	Ca	0.000002140	6.111
26	Fe	0.000039844	7.896
14	Si	0.000033141	8.149
13	Al	0.000002757	5.984

Table 2.1: *Relative abundances and ionization energies of first ionization for the eleven most abundant elements in the solar photosphere.*

where the sum runs over the particle species (labeled with index i) , n_i^* is the number density of ionized particles of type i, and χ_i is the corresponding ionization energy. $n_a = \sum n_i$ is the number density of nuclei, n_e the number density of electrons. Defining the ionization degree, $x_i = n_i^*/n_i$, and the relative abundance, $\nu_i = n_i/n_a$, Eq. (2.32) can be rewritten as

$$\varepsilon_{\text{int}} = \frac{3kT}{2\mu_a m_0}\left(1 + \sum x_i\nu_i\right) + \frac{1}{\mu_a m_0}\sum x_i\nu_i\chi_i, \tag{2.33}$$

where μ_a is the mean molecular weight of the neutral gas ($\mu_a = 1.29$ for solar composition) and m_0 is the atomic mass unit. The ionization degrees, x_i, are determined by the set of Saha equations

$$\frac{x_i}{1-x_i}\sum x_i\nu_i = \frac{u_{i1}(T)}{u_{i0}(T)}\frac{\mu_a m_0}{\varrho}\frac{2\left(2\pi m_e kT\right)^{3/2}}{h^3}\exp\left(-\chi_i/kT\right). \tag{2.34}$$

The temperature dependence of the partition functions u_{i1}, u_{i0} can be obtained from the literature (e.g., Irwin 1981). For temperatures exceeding about 16000 K, the elements are almost fully ionized and the temperature dependence can be neglected. In order to obtain the temperature from ϱ and e_{int}, the nonlinear system of equations (2.33) and (2.34) needs to be solved iteratively. Once the temperature is known, the gas pressure follows from

$$p = \left(n_e + n_a\right)kT = \frac{\varrho}{\mu_a m_0}\left(1 + \sum x_i\nu_i\right)kT. \tag{2.35}$$

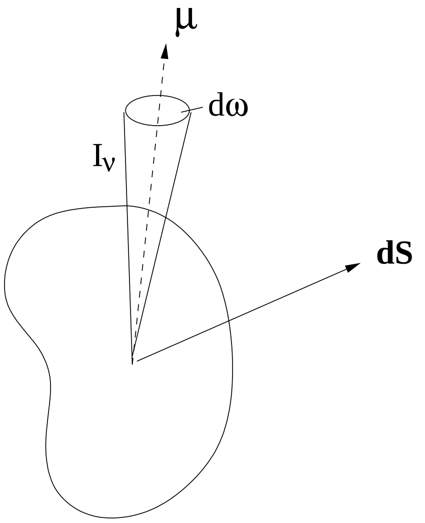

Figure 2.1: *The unit vector* $\boldsymbol{\mu}$ *points to the direction of radiation. The vector* **dS** *is perpendicular to the area element.*

2.4 The radiative source term

The photosphere is the region where most of the radiation leaves the Sun and where radiation takes over from convection as the dominant energy transport mechanism. The energy exchange between gas and radiation determines the temperature structure of the photosphere and is responsible for the entropy drop which acts as the main driver of convection. Therefore any realistic simulation must include the radiative energy exchange rate, Q_{rad}, as a source term in the energy equation. Since the mean free path of photons goes to infinity as the atmosphere becomes transparent in the photosphere, radiative transfer at this height is essentially non-local, rendering the diffusion approximation of radiative energy transport inadequate. Hence, starting point for determining Q_{rad} is the (time- and frequency-dependent) radiative transfer equation (RTE hereafter),

$$\left(\frac{1}{c}\frac{\partial}{\partial t} + \boldsymbol{\mu}\cdot\nabla\right) I_\nu = \kappa_\nu \varrho (S_\nu - I_\nu) \ . \tag{2.36}$$

The *specific intensity* I_ν is defined such that the amount of energy $d\mathcal{E}_{rad}$ transported by radiation along direction $\boldsymbol{\mu}$ in the frequency interval $(\nu, \nu + d\nu)$ across an area element dS into a solid angle $d\omega$ in a time interval dt is

$$d\mathcal{E}_{rad} = I_\nu(\mathbf{x}, \boldsymbol{\mu}, t)(\boldsymbol{\mu}\cdot\mathbf{dS})\, d\omega\, d\nu\, dt \tag{2.37}$$

(see Fig. 2.1). S_ν is the source function and κ_ν is the opacity of the material. Since the travel time of a photon through the photosphere is much shorter than any other relevant timescale, the radiation field can be assumed to adjust instantaneously to any change of the thermodynamical state of the gas, i.e. the time derivative in Eq. 2.36 can be neglected and we obtain

$$\boldsymbol{\mu} \cdot \nabla I_\nu = \kappa_\nu \varrho (S_\nu - I_\nu) \ . \tag{2.38}$$

Defining the optical depth of a path element ds as

$$d\tau_\nu := \kappa_\nu \varrho \, ds \ , \tag{2.39}$$

the RTE can be written in the form

$$\frac{dI_\nu}{d\tau_\nu} = S_\nu - I_\nu \ . \tag{2.40}$$

This equation has the (formal) solution

$$I_\nu(\tau_\nu) = I_\nu(0) \, e^{-\tau_\nu} + \int_0^{\tau_\nu} S_\nu(t_\nu) \, e^{-(\tau_\nu - t_\nu)} \, dt_\nu \ . \tag{2.41}$$

If one assumes that the matter is in *local thermal equilibrium* (LTE), the source function is given by the Planck function

$$S_\nu = B_\nu \ . \tag{2.42}$$

For the remaining part of this thesis we shall always assume LTE. The essential premise of LTE is that elastic collisions between particles represent the dominant interaction on a microscopic level. Then the velocity distribution of particles is Maxwellian and the ionization states and population numbers of atomic, ionic, and molecular energy levels are determined by Saha-Boltzmann statistics corresponding to the local temperature. Significant departures from LTE must be expected in the upper photosphere, especially in strong lines where scattering dominates over thermal emission and disturbs the detailed energy balance of LTE. This effect can be neglected as long as these lines do not contribute significantly to the total (frequency-integrated) energy exchange rate, Q_{rad}. Since in LTE the source function is independent of the radiation field, Eq. (2.41) can be integrated in a straightforward manner. The numerical treatment of radiative transfer discussed in Chapter 4 is based on this formal solution. Once the radiation field is known, the radiative energy flux,

$$\mathbf{F}_\nu = \int_{4\pi} I_\nu(\boldsymbol{\mu}) \, \boldsymbol{\mu} \, d\omega \ , \tag{2.43}$$

and the average intensity,

$$J_\nu = \frac{1}{4\pi} \int_{4\pi} I_\nu(\boldsymbol{\mu}) \, d\omega \ , \tag{2.44}$$

can be calculated. The radiative heating rate then follows either from

$$Q_{\mathrm{rad}} = -\int_{\nu} (\nabla \cdot \mathbf{F}_{\nu})\, d\nu \tag{2.45}$$

or from the equivalent expression

$$Q_{\mathrm{rad}} = 4\pi\kappa\varrho \int_{\nu} \kappa_{\nu}(J_{\nu} - B_{\nu})\, d\nu \quad . \tag{2.46}$$

Chapter 3

The MHD code

This chapter discusses the numerical methods of the MHD code. The code used here is based on a code for general MHD applications, which was developed by T. Linde and A. Malagoli at the University of Chicago. This basic code solves the MHD equations (2.17), (2.19), (2.20), and (2.27) without radiative source term, assuming constant scalar diffusion coefficients μ, K, and η and using the equation of state for an ideal gas. The numerical discretization and parallelization of this code is described in sections 3.1 and 3.2. The code in its original form did not meet the particular requirements of "realistic" solar simulations regarding physical processes to be included, boundary conditions and numerical stability. So one of the goals of this PhD project was to implement the modifications and extensions necessary to make the basic code usable for applications in the solar photosphere and convection zone:

(i) The most extensive addition was the development of a non-local and non-grey radiative transfer module. While all other terms in the system of MHD equations can be expressed *locally* by the physical quantities and their derivatives, the radiative source term is essentially non-local and, accordingly, the numerical treatment is very different from that of the other terms. In fact, the radiative transfer part of the code constitutes a largely separate module. It is discussed in detail in Chapter 4.

(ii) The equation of state was replaced by a realistic one following the outline in section 2.3. From a technical point of view this implies that conversions between thermodynamical quantities are based on pre-compiled tables from which the required quantities are interpolated during runtime of the code. The tables used in the code were calculated by S. Shelyag (Max-Planck-Institut für Aeronomie).

(iii) The strong stratification of the sun, especially in the photosphere, leads to wave amplification and shock formation in the low-density upper photospheric layers, which any code designed to include these regions must handle. Initial tests of the code showed that numerical stability had to be improved by introducing artificial diffusivities. These diffusivities are designed to prevent the build-up of energy at small scales and thus suppress spurious oscillations and "ringing" of shocks while leaving resolved strutures unaffected. The details are discussed in section 3.3.

(iv) Since simulations of solar magneto-convection can only cover a small part of the sun, the computational domain is not delimited by physical boundaries. On the other hand, a unique numerical solution of the system of partial differential equations requires the specification of boundary conditions at the boundaries of the simulation box. An attempt to resolve this dilemma is the concept of "open" boundary conditions which allow free in- and outflow of material through the boundaries. Such an open boundary was implemented for the bottom of the computational domain. In the simulations done here, it is located in the upper convection zone where warm up- and cool downflows account for most of the energy transported in and out of the simulated domain. Therefore, any closed boundary condition at the bottom would grossly distort the pattern of the velocity field and neglect the dominant mechanism of energy transport. The detailed numerical implementation of the boundary conditions is discussed in section 3.4.

The MHD code was tested with a series of standard test problems (e.g., Kelvin-Helmholtz instability, Orszag-Tang vortex, Sod's shocktube problem).

3.1 Spatial discretization and parallelization

The MHD code solves the system of MHD equations on a three-dimensional equidistant cartesian grid. The spatial discretization of the equations is based on the fourth-order centered-difference scheme on a 5-point stencil. Choosing i as the index denoting the grid position along a particular spatial direction, the first and second spatial derivatives of quantity u are given by

$$\left(\frac{\partial u}{\partial x}\right)_i = \frac{1}{12\Delta x}\left(-u_{i+2} + 8u_{i+1} - 8u_{i-1} + u_{i-2}\right) \tag{3.1}$$

and

$$\left(\frac{\partial^2 u}{\partial x^2}\right)_i = \frac{1}{12\Delta x^2}\left(-u_{i+2} + 16u_{i+1} - 30u_i + 16u_{i-1} - u_{i-2}\right), \tag{3.2}$$

respectively.

For partial differential equations which correspond to a conservation law, i.e. which are of the form

$$\frac{\partial u}{\partial t} + \frac{\partial f(u)}{\partial x} = 0, \tag{3.3}$$

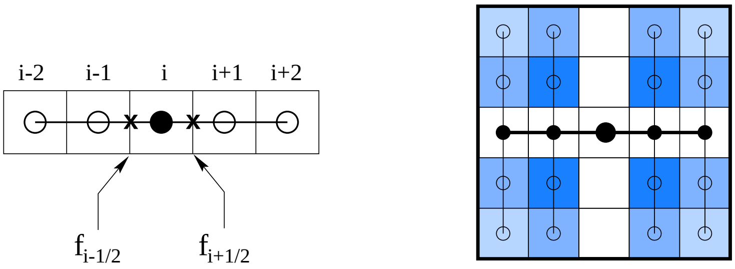

Figure 3.1: *Left: 5-point stencil centered around grid cell i for the fourth order scheme. The numerical flux f is defined on cell interfaces (marked by crosses). Right: The 5×5 stencil for mixed 2nd derivatives. Cells with same color shading have same weight. White cells do not contribute to the derivative.*

with a flux function $f(u)$, the centered difference scheme is equivalent to a finite volume scheme in conservative form. A straightforward calculation shows that the flux divergence $\partial f(u)/\partial x$ discretized according to Eq. 3.1 is identical to the difference expression

$$\left(\frac{\partial f(u)}{\partial x}\right)_i = \frac{1}{\Delta x}\left(f_{i+1/2} - f_{i-1/2}\right) \tag{3.4}$$

with the numerical flux

$$f_{i+1/2} = \frac{7}{12}\left(f(u_{i+1}) + f(u_i)\right) - \frac{1}{12}\left(f(u_{i+2}) + f(u_{i-1})\right) \tag{3.5}$$

defined on the cell interfaces (see Fig. 3.1, left panel). Therefore, any quantitity obeying a conservation law is exactly conserved numerically as long as the total integrated flux at the domain boundaries vanishes.

In a multidimensional domain mixed derivatives are calculated by straightforward successive application of Eq. 3.1 in different coordinate directions. From the linearity of Eq. 3.1 it follows that mixed derivatives commute, i.e.

$$\frac{\partial}{\partial x} \circ \frac{\partial}{\partial y} = \frac{\partial}{\partial y} \circ \frac{\partial}{\partial x}. \tag{3.6}$$

Fig. 3.1 (right panel) shows the 5 × 5 stencil for mixed 2nd derivatives.

The code is parallelized using a domain decomposition scheme. The computational domain is divided into a three-dimensional array of rectangular subdomains, each of which is assigned to a separate process on the computer. Parallelization is done with MPI and follows the distributed memory concept, i.e. each

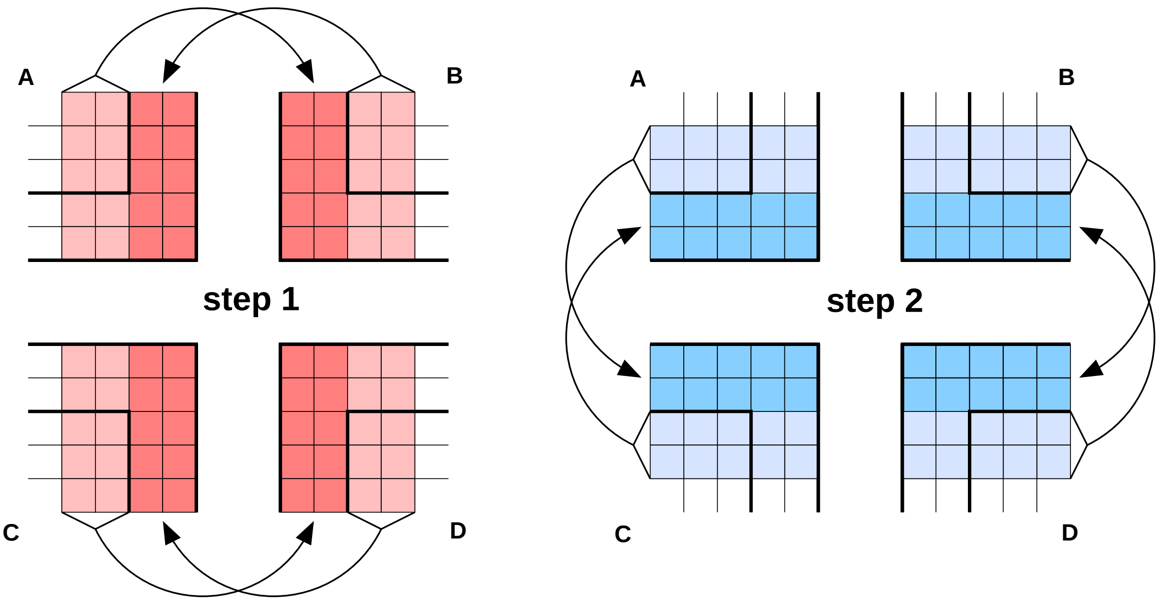

Figure 3.2: *Two-step communication between four adjacent processes A to D in two dimensions. Source regions are shaded in light colors, target regions in dark colors.*

process only possesses knowledge of the variables in its own subdomain. In order to apply the 5-point stencil of the fourth-order scheme to grid cells bordering on subdomain boundaries, knowledge of two layers of cells outside the subdomain is required. Therefore each subdomain is coated with two layers of "ghost" cells on each subdomain boundary. If it borders on a neighbouring domain, the required information is communicated between the neighbours and stored in the ghost layers before the numerical derivatives are evaluated. If the subdomain boundary coincides with a global boundary, the ghost cells are filled with values according to the boundary conditions. The information exchange is done separately for each coordinate direction (see Fig 3.2 for an illustration of the communication in 2 dimensions). Thus, corner values are sent to diagonal neighbours via successive 1D communication in all coordinate directions.

3.2 Temporal discretization

The numerical solution of the system is advanced in time using an explicit fourth-order Runge-Kutta scheme. Defining $\mathbf{U}_0$ as the vector which describes the state of the system for time t_0, i.e.

$$\mathbf{U_0} = (\varrho, \varrho\mathbf{v}, e, \mathbf{B})(x, y, z, t_0), \tag{3.7}$$

the system of partial equations can be written as

$$\frac{\partial \mathbf{U}}{\partial t} = \mathbf{R}(\mathbf{U}), \tag{3.8}$$

where the vector $\mathbf{R}(\mathbf{U})$ contains the spatial derivatives and additional source terms in the system of equations. Then the new state $\mathbf{U}_1$ for time $t_1 = t_0 + \Delta t$ is calculated in four steps:

$$\begin{aligned} \mathbf{U}_{\frac{1}{4}} &= \mathbf{U}_0 + \frac{\Delta t}{4}\,\mathbf{R}(\mathbf{U}_0), \\ \mathbf{U}_{\frac{1}{3}} &= \mathbf{U}_0 + \frac{\Delta t}{3}\,\mathbf{R}(\mathbf{U}_{\frac{1}{4}}), \\ \mathbf{U}_{\frac{1}{2}} &= \mathbf{U}_0 + \frac{\Delta t}{2}\,\mathbf{R}(\mathbf{U}_{\frac{1}{3}}), \end{aligned}$$

and finally

$$\mathbf{U}_1 = \mathbf{U}_0 + \Delta t\,\mathbf{R}(\mathbf{U}_{\frac{1}{2}}). \tag{3.9}$$

The maximum allowed size of the timestep, Δt, is usually given by a CFL-like criterion, which ensures that in a single timestep, flow velocities and wave speeds transport information across distances not larger than the mesh width. While it is not possible to derive a stringent criterion for a system of nonlinear equations, the analysis of *linear* advection-diffusion equations discretized with fourth-order centered differences provides a modified CFL criterion (Hirsch 1988). This can be used as a guideline for the system of MHD equations (2.17), (2.19), (2.20) and (2.27), which is also of advective-diffusive type. The timestep criterion used in our code reads

$$\Delta t_{\mathrm{max}} = \min(\Delta t_{\mathrm{ad}}, \Delta t_{\mathrm{diff}}), \tag{3.10}$$

with

$$\Delta t_{\mathrm{ad}} = \frac{8}{3} \cdot \frac{\min(\nu, \eta, \kappa)}{c_{\mathrm{tot}}^2} \tag{3.11}$$

and

$$\Delta t_{\mathrm{diff}} = \frac{2}{3}\left[\max(\nu, \eta, \kappa) \cdot \left(\frac{1}{\Delta x^2} + \frac{1}{\Delta y^2} + \frac{1}{\Delta z^2}\right)\right]^{-1}. \tag{3.12}$$

c_{tot} is the total wave speed:

$$c_{\mathrm{tot}} = v + c_{\mathrm{sound}} + c_{\mathrm{Alfvén}}. \tag{3.13}$$

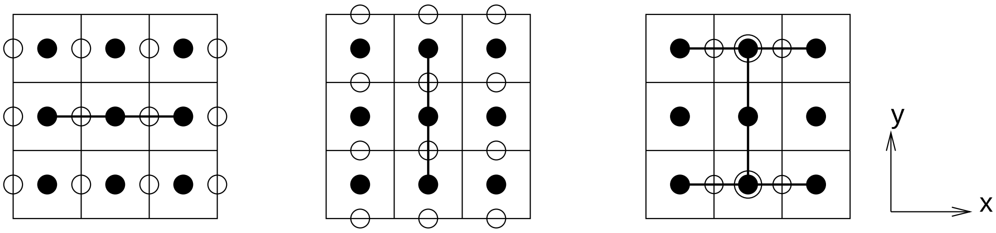

Figure 3.3: *The numerical stencil for the artificial diffusivities. Empty circles indicate the staggered grid on which the hyperdiffusive coefficients are defined. Left and middle panel: grid and stencil for the terms* $\partial_x(\nu\partial_x u)$ *and* $\partial_y(\nu\partial_y u)$*, respectively. Right panel: stencil for the term* $\partial_y(\nu\partial_x u)$ *with mixed derivatives.*

3.3 Artificial diffusivities

The low viscosity and corresponding high Reynolds number in the solar convection zone lead to structure formation down to a diffusive length scale of the order of centimeters. Since the computing power necessary to resolve these scales in a numerical simulation exceeds the capacity of contemporary computers by many orders of magnitude, all simulations of the solar photosphere and convection zone are necessarily *large-eddy* simulations, which simulate flows on resolvable scales and cut off the part of the energy spectrum which lies below the grid scale. In order to balance the cascading of energy to small scales due to the nonlinearity in the Navier-Stokes equations, any large-eddy simulation must provide for some kind of numerical viscosity to prevent the build-up of energy at the grid scale. From the numerical point of view, there are two approaches to achieve this: the first one uses numerical schemes with an inherent numerical viscosity, which keeps the solution stable (e.g. Riemann solvers). In this case, explicit viscous terms are not necessary and pure advection equations are solved. The drawback of this approach is that the implicit viscosity usually acts also on the resolved scales, resulting in relatively low effective Reynolds numbers of the computed solution. The other approach is based on numerical schemes which are highly non-diffusive (like e.g. higher-order centered-difference schemes) and use explicit viscous terms to dissipate energy at the grid scale. We follow the second approach and use the methods described by Stein & Nordlund (1998) and Caunt & Korpi (2001) as a guideline:

The diffusive terms in the momentum and energy equations are replaced by artificial equivalents; likewise, in the continuity equation an artificial diffusive term is introduced, which has no physical counterpart. In the induction equation, we retain the fourth-order centered-difference term with constant η and add artificial diffusion only near the lower boundary of the computational domain, where we found it necessary to stabilize the code.

For each physical quantity subject to diffusion and for each coordinate direction, a separate diffusion coefficient, consisting of a shock-resolving and a hyperdiffusive part, is defined:

$$\nu_l(u) = \nu_l^{\mathrm{shk}} + \nu_l^{\mathrm{hyp}}(u). \tag{3.14}$$

Here u stands for the quantity to be diffused and the index l indicates the coordinate direction.

The shock-resolving part is designed to have significant values in those regions, where converging flows with strong cell to cell velocity jumps lead to the build-up of strong gradients in advected quantities. The rate at which gradients grow due to converging flows is determined by the local value of the flow divergence. To limit the strength of gradients, the shock diffusivity is taken proportional to the absolute value of the divergence in regions of converging flow while it is set to zero elsewhere:

$$\nu_l^{\mathrm{shk}} = \begin{cases} c_{\mathrm{shk}} \cdot \Delta x_l^2 \cdot |\nabla \cdot \mathbf{v}| & \nabla \cdot \mathbf{v} < 0 \\ 0 & \nabla \cdot \mathbf{v} \geq 0 \end{cases}. \tag{3.15}$$

c_{shk} is a scaling factor of order unity and Δx_l is the grid spacing in direction l. With the shock-diffusivity defined this way the timescale for the build-up of gradients at the location of shocks is approximately balanced by the diffusion-timescale across the mesh width Δx_l, which ensures that the solution remains resolved at the shock. We included the shock diffusivity in the momentum and energy equations. In the other equations it was not found to be necessary for stability and therefore not included.

The hyperdiffusive part is defined on cell interfaces normal to the direction of diffusion. The staggered grid used for hyperdiffusion is shown in Fig. 3.3. For a physical quantity u and direction l it is given by

$$\nu_l^{\mathrm{hyp}}(u) = c_{\mathrm{hyp}} \cdot c_{\mathrm{tot}} \cdot \Delta x_l \cdot \frac{\max_3 \Delta_l^3 u}{\max_3 \Delta_l^1 u}. \tag{3.16}$$

Here c_{hyp} is a scaling factor of order unity, c_{tot} is the sum of flow velocity, speed of sound, and Alfvén velocity. At cell interface $i + \frac{1}{2}$ between cells i and $i + 1$ (i being the grid index of direction l), the expressions $\Delta_l^3 u$ and $\Delta_l^1 u$ are defined as the third and first differences of u, respectively:

$$(\Delta_l^3 u)_{i+\frac{1}{2}} = |3(u_{i+1} - u_i) - (u_{i+2} - u_{i-1})| \tag{3.17}$$

and

$$(\Delta_l^1 u)_{i+\frac{1}{2}} = |u_{i+1} - u_i|. \tag{3.18}$$

$\max_3$ indicates that the maximum over three adjacent interfaces is taken. The expression $\Delta_l^3 u / \Delta_l^1 u$ in Eq. 3.16, which is proportional to the ratio of third and first derivatives, detects small-scale fluctuations and makes sure that the hyperdiffusion assumes significant values only where numerical noise on the grid level needs to be dissipated while resolved structures remain largely unaffected. Setting the coefficients of hyperdiffusion proportional to $c_{\mathrm{tot}} \cdot \Delta x_l$ results in diffusive timescales across the mesh width Δx_l, that balance the timescale on which noise on the grid scale grows as the result of the information exchange between neighbouring grid cells.

With the artificial diffusion ν_l defined this way, the diffusive terms in the continuity and energy equations are given by

$$\left(\frac{\partial \varrho}{\partial t}\right)_{\mathrm{diff}} = \sum_l \frac{\partial}{\partial x_l}\left(\nu_l(\varrho)\frac{\partial \varrho}{\partial x_l}\right) \tag{3.19}$$

and

$$\left(\frac{\partial e}{\partial t}\right)_{\mathrm{diff}} = \sum_l \frac{\partial}{\partial x_l}\left(\varrho \nu_l(T)\,\frac{\partial c_p T}{\partial x_l}\right), \tag{3.20}$$

respectively. The diffusive terms for the vector quantities $\mathbf{v}$ and $\mathbf{B}$ have a more complicated structure. In the momentum equations they are given by

$$\left(\frac{\partial \varrho \mathbf{v}}{\partial t}\right)_{\mathrm{diff}} = \nabla \cdot \underline{\underline{\tau}}, \tag{3.21}$$

where $\underline{\underline{\tau}}$ is the symmetrized stress tensor

$$\tau_{kl} = \frac{1}{2}\varrho\left(\nu_k(v_l)\frac{\partial v_l}{\partial x_k} + \nu_l(v_k)\frac{\partial v_k}{\partial x_l}\right). \tag{3.22}$$

In the equation for the total energy, the dissipated energy is taken into account by a viscous heating term

$$\left(\frac{\partial e}{\partial t}\right)_{\mathrm{visc}} = \nabla \cdot \left(\mathbf{v} \cdot \underline{\underline{\tau}}\right). \tag{3.23}$$

The artifical diffusive term in the induction equation is given by

$$\left(\frac{\partial \mathbf{B}}{\partial t}\right)_{\mathrm{diff}} = -\nabla \times \boldsymbol{\mathcal{E}}. \tag{3.24}$$

The vector quantity $\boldsymbol{\mathcal{E}}$ is defined as

$$\boldsymbol{\mathcal{E}} = \begin{pmatrix} \nu_y(B_z)\partial_y B_z - \nu_z(B_y)\partial_z B_y \\ \nu_z(B_x)\partial_z B_x - \nu_x(B_z)\partial_x B_z \\ \nu_x(B_y)\partial_x B_y - \nu_y(B_x)\partial_y B_x \end{pmatrix}. \tag{3.25}$$

The dissipated energy is accounted for in the energy balance and appears in the energy equation as an Ohmic heating term:

$$\left(\frac{\partial e}{\partial t}\right)_{\mathrm{ohm}} = \frac{1}{4\pi}\nabla \cdot (\mathbf{B} \times \boldsymbol{\mathcal{E}})\,. \tag{3.26}$$

All artificial diffusion terms are discretized with second-order centered differences. At grid point i, a diffusion term of the form $\partial_x(\nu\partial_x u)$ is then calculated as

$$\left(\frac{\partial u}{\partial t}\right)_{\mathrm{diff},i} = \frac{1}{\Delta x}\left(\nu_{i+\frac{1}{2}} \cdot \frac{u_{i+1} - u_i}{\Delta x} - \nu_{i-\frac{1}{2}} \cdot \frac{u_i - u_{i-1}}{\Delta x}\right). \tag{3.27}$$

In a term with mixed derivatives like $\partial_y(\nu\partial_x u)$, the hyperdiffusion coefficient is interpolated from cell interfaces onto cell centers. The inner part of such a term is then discretized as

$$\left(\nu\frac{\partial u}{\partial x}\right)_i = \left(\frac{\nu_{i+\frac{1}{2}} + \nu_{i-\frac{1}{2}}}{2}\right) \cdot \left(\frac{u_{i+1} - u_{i-1}}{2\Delta x}\right). \tag{3.28}$$

All diffusive terms impose a timestep condition of the form

$$\Delta t_\nu < c_\nu \cdot \frac{\Delta x^2}{\nu}, \tag{3.29}$$

which is based on the diffusion time across the mesh width, Δx.

3.4 Boundary conditions

3.4.1 Upper boundary

The upper boundary of the computational domain is assumed to be closed, with stress-free conditions for the horizontal velocity components. In our simulations, the upper boundary is located in the upper photosphere near the temperature minimum, where densities are very low. Therefore, one expects, that possible inaccuracies in the modelling of the flow field in the uppermost layers of the computational domain due to the unrealistic assumption of a closed box have only a small influence on the deeper layers around $\tau = 1$, which we are primarily interested in. Physically, a closed boundary implies that the vertical convective fluxes of mass, energy and horizontal momentum vanish on the boundary itself. For this purpose, we set the vertical velocity and the vertical gradients of density and energy to zero:

$$v_z\,\big|_{\mathrm{top}} \equiv 0, \qquad \left.\frac{\partial \varrho}{\partial z}\right|_{\mathrm{top}} \equiv 0, \qquad \left.\frac{\partial \varepsilon}{\partial z}\right|_{\mathrm{top}} \equiv 0. \tag{3.30}$$

The numerical implementation of these conditions reads

$$[v_z]^{\mathrm{gc}}_{1,2} = -[v_z]^{\mathrm{dc}}_{1,2}, \qquad \varrho^{\mathrm{gc}}_{1,2} = \varrho^{\mathrm{dc}}_{1,2}, \qquad \varepsilon^{\mathrm{gc}}_{1,2} = \varepsilon^{\mathrm{dc}}_{1,2}, \tag{3.31}$$

where the superscripts dc and gc refer to domain cells and ghost cells respectively (see also Fig. 3.4). The stress free boundary conditions

$$\left.\frac{\partial v_x}{\partial z}\right|_{\mathrm{top}} \equiv 0, \qquad \left.\frac{\partial v_y}{\partial z}\right|_{\mathrm{top}} \equiv 0 \tag{3.32}$$

imply

$$[v_x]^{\mathrm{gc}}_{1,2} = [v_x]^{\mathrm{dc}}_{1,2}, \qquad [v_y]^{\mathrm{gc}}_{1,2} = [v_y]^{\mathrm{dc}}_{1,2}. \tag{3.33}$$

As a comparison with Eq. (3.5) shows, with this choice of boundary conditions the numerical fluxes corresponding to ϱv_z, $\varrho\varepsilon v_z$ and $\varrho v_{x,y} v_z$ vanish on the interface between ghost cells and domain cells, as required by the closed-box condition. For the magnetic field we assume that the field lines are vertical at the boundary, i.e.

$$B_{x,y}\,|_{\mathrm{top}} \equiv 0. \tag{3.34}$$

By virtue of solenoidality of $\mathbf{B}$, this implies

$$\left.\frac{\partial B_z}{\partial z}\right|_{\mathrm{top}} \equiv 0. \tag{3.35}$$

The corresponding conditions for the ghost cell values read

$$[B_z]^{\mathrm{gc}}_{1,2} = [B_z]^{\mathrm{dc}}_{1,2}, \qquad [B_{x,y}]^{\mathrm{gc}}_{1,2} = -[B_{x,y}]^{\mathrm{dc}}_{1,2}. \tag{3.36}$$

With this boundary condition free footpoint movement of the field lines is allowed.

While the symmetric choice of ε is consistent with the small vertical temperature gradients encountered in the upper photosphere, the symmetric conditons for ϱ, and hence, p, are certainly not realistic, since one expects a roughly exponential density and pressure stratification in this region. In order to avoid unphysical behaviour as a result of these assumptions, the vertical pressure gradient is treated separately at the upper boundary. Straightforward application of the fourth-order centered-difference stencil on the symmetric pressure values around the boundary would lead to unrealistic values of $(\nabla p)_z$ in the first two layers of domain cells. Therefore we replace it with the following first- and second-order expressions, which do not make use of the ghost cell pressure values:

$$\left[\frac{\partial p}{\partial z}\right]^{\mathrm{dc}}_1 = \frac{p^{\mathrm{dc}}_1 - p^{\mathrm{dc}}_2}{\Delta z}; \qquad \left[\frac{\partial p}{\partial z}\right]^{\mathrm{dc}}_2 = \frac{p^{\mathrm{dc}}_1 - p^{\mathrm{dc}}_3}{2\Delta z} \tag{3.37}$$

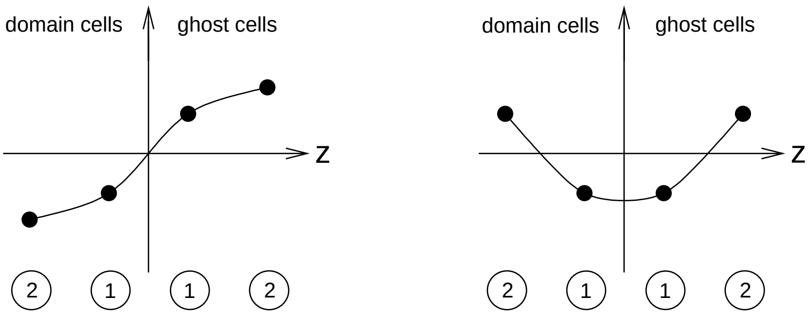

Figure 3.4: *Left: A quantity is set to zero on the boundary by filling the ghost cells with values antisymmetric with respect to the neighbouring domain cell values. Right: zero-gradient conditions are realized by filling the ghost cells symetrically.*

3.4.2 Lower boundary

The lower boundary of the computational domain is located in the convectively unstable upper layers of the convection zone, which are characterized by bulk fluid motions. Ideally, an implementation of an open lower boundary should allow for free motions across the boundary without interfering with the fluid. Some degree of interference is unavoidable, though, since in principle any formulation of an open boundary condition requires knowledge of the physical conditions outside the domain, which is not available. The missing information has to be replaced with reasonable assumptions regarding the physical properties of the fluid at the boundary.

The first assumption we make is that the total pressure $p_{\text{tot}} = p + |\mathbf{B}^2|/8\pi$ is constant across the lower boundary:

$$p_{\text{tot}}\,\big|_{\text{bot}} \equiv p_{\text{tot},0} \tag{3.38}$$

This is justified as long as fluid motions are slow compared to the speed of magneto-acoustic waves[1] $c_{\text{mag}} = \sqrt{c^2_{\text{Alfén}} + c^2_{\text{sound}}}$, since in this case fluctuations in p_{tot} are balanced on a timescale smaller than the hydrodynamical timescale. For the magnetic field the same conditions as for the upper boundary are specified [see Eq. (3.36)]. Forcing the magnetic field lines to be vertical on the boundary implies that no magnetic flux is advected into or out of the box by the convective flow. Equations (3.38) and (3.36) determine the local gas pressure at the boundary:

$$p\,\big|_{\text{bot}} = p_0 = p_{\text{tot},0} - \left.\frac{|\mathbf{B}^2|}{8\pi}\right|_{\text{bot}}, \tag{3.39}$$

---

[1] This assumption is certainly valid for the slowly drifting upflows. Violations might occasionally arise in isolated strong downflows.

which, in turn, fixes the ghost cell values for p:

$$p_{1,2}^{\mathrm{gc}} - p_0 = p_0 - p_{1,2}^{\mathrm{dc}} \tag{3.40}$$

Apart from these global conditions, regions with up- and downflows, respectively, are treated separately.

Downflows

In boundary regions with $v_z < 0$ the downflowing material should leave the box uninhibited. We allow a smooth outflow by setting

$$\left.\frac{\partial v_x}{\partial z}\right|_{\mathrm{bot}} = \left.\frac{\partial v_y}{\partial z}\right|_{\mathrm{bot}} = \left.\frac{\partial v_z}{\partial z}\right|_{\mathrm{bot}} \equiv 0. \tag{3.41}$$

In order to fix the energy values in the ghost cells, one needs to make an assumption regarding the vertical structure of the flow near the boundary. Since the radiative energy exchange and thermal diffusion are negligible at the depth level of the bottom boundary, both upflows and downflows are assumed to be isentropic, albeit with different values of the specific entropy. Consequently, one has to find ghost cell values for the internal energy density per unit mass, ε, such that

$$\left.\frac{\partial s}{\partial z}\right|_{\mathrm{bot}} \equiv 0 \tag{3.42}$$

is at least approximately fulfilled (s is the entropy density per unit mass). From one-dimensional model atmospheres (e.g. Spruit 1974) one can derive a relation of the form[2]

$$\varepsilon \propto p^{\xi} \tag{3.43}$$

with a value $\xi \approx 0.25$ that corresponds to a depth of $800 - 1000$ km in the convection zone. Using this relation, the numerical equivalent of Eq. (3.42) is given by

$$\varepsilon_{1,2}^{\mathrm{gc}} = \varepsilon_{1,2}^{\mathrm{dc}} \cdot \left(\frac{p_{1,2}^{\mathrm{gc}}}{p_{1,2}^{\mathrm{dc}}}\right)^{0.25} . \tag{3.44}$$

The ghost cell values for ϱ are then interpolated from tables, viz.

$$\varrho^{\mathrm{gc}} = \varrho(\varepsilon^{\mathrm{gc}}, p^{\mathrm{gc}}), \tag{3.45}$$

---

[2] Formally, this follows from the adiabatic relation $p \propto \varrho^{\gamma}$ and the corresponding equation for the energy density, $\varepsilon \propto \varrho^{\Gamma_\varepsilon - 1}$, with a different adiabatic exponent Γ_ε, which implies $\xi = (\Gamma_\varepsilon - 1)/\gamma$. For a partly ionized gas, both γ and Γ_ε are functions of the other thermodynamical variables, so the choice of a fixed value for ξ is an approximation. Spruit (1974) gives a value of $\gamma \approx 1.14$ at a depth of $800 - 1000$ km in his solar model. Γ_ε is somewhat larger because of the increase in latent heat under adiabatic compression. The choice of $\xi = 0.25$ corresponds to $\Gamma_\varepsilon \approx 1.3$.

while the internal energy density per volume, e_{int}, is simply given by

$$e_{\mathrm{int}}^{\mathrm{gc}} = \varrho^{\mathrm{gc}} \varepsilon^{\mathrm{gc}}. \tag{3.46}$$

Upflows

Owing to the strong stratification of the convection zone, upflows undergo a strong adiabatic expansion, which tends to smooth out any fluctuation that may have affected them during their rise. Therefore, one expects upflows entering the computational domain to be more or less homogeneous. In our implementation, the internal energy density (per mass) in upflows is assumed to be constant across the lower boundary and set to a global value, ε_0. Together with p_0, this fixes the entropy density, s_0, at the bottom. Again assuming an adiabatic flow and using the approximative relation (3.43), the ghost cells are filled with energy values that correspond to s_0:

$$\varepsilon_{1,2}^{\mathrm{gc}} = \varepsilon_0 \cdot \left(\frac{p_{1,2}^{\mathrm{gc}}}{p_0} \right)^{0.25} . \tag{3.47}$$

We require that all inflows be vertical with a smooth vertical profile of v_z:

$$v_x \,|_{\mathrm{bot}} = v_y \,|_{\mathrm{bot}} \equiv 0, \qquad \left. \frac{\partial v_z}{\partial z} \right|_{\mathrm{bot}} \equiv 0. \tag{3.48}$$

The parameter ε_0 determines the inflow of energy into the computational box and can be used to control the net vertical energy flux through the domain. We adjust the value of ε_0 in time in order to make sure that the time-averaged radiation flux density which leaves the box at the top is equal to the solar value $F_\odot = 6.34 \cdot 10^{10}$ erg s^{-1} cm^{-2}. Since the rate at which energy is radiated does not react instantaneously to changes in ε_0, the correction is done on the Kelvin-Helmholtz timescale τ_{KH} of the system, which corresponds to the timespan over which the net energy transported through the domain equals the total energy content of the system:

$$\tau_{\mathrm{KH}} = \frac{\int_{\mathrm{box}} e_{\mathrm{int}} \, dV}{\int_{\mathrm{top}} F_\odot \; dx \, dy}. \tag{3.49}$$

At each timestep, ε_0 is corrected according to

$$\varepsilon_0 \longrightarrow \varepsilon_0 \cdot \left(1 + \frac{\Delta t}{\tau_{\mathrm{KH}}} \cdot \frac{F_\odot - F_{\mathrm{top}}}{F_\odot} \right), \tag{3.50}$$

where F_{top} is the current value of the simulated radiation flux at the top of the domain.

In regions where the magnetic energy density exceeds the kinetic energy, convective motions are effectively suppressed. On the lower boundary, such strong field regions should not carry the same energy ε_0 as uninhibited upflows in weak-field regions. For this reason, we define a threshold value $B_{\mathrm{t}} = 800\,\mathrm{G}$ and treat regions with $v_z \geq 0$ and $|\mathbf{B}| > B_{\mathrm{t}}$ similar to downflows, setting $\partial_z s = 0$ and replacing Eq. (3.47) with Eq. (3.44).

Control of mass influx

Since our numerical simulations are carried out in a rather small computational box containing a limited number of convective flow cells, statistical fluctuations of the total mass in the simulated volume can become significant, if no measures are taken to control the mass flux across the lower boundary. We use the total pressure, $p_{\mathrm{tot},0}$, as control parameter to keep the total mass of the system constant. Let δM be the (relative) mass deficit inherited from the previous timestep:

$$\delta M = \frac{M - M_0}{M_0} \tag{3.51}$$

(M is the current total mass, M_0 the initial value). In order to allow for a smooth adjustment of $p_{\mathrm{tot},0}$, we require that the deficit δM be balanced on a timescale $\tau_M = 30$ sec. For each timestep the deficit to be corrected is

$$\delta M_{\mathrm{corr}} = \delta M \cdot \frac{\Delta t}{\tau_M}. \tag{3.52}$$

Based on the value of $p_{\mathrm{tot},0}$ from the previous timestep, this deficit is balanced by adjusting the pressure in the upflow regions:

$$p_{\mathrm{up}} = p_{\mathrm{tot},0} + \Delta p. \tag{3.53}$$

The resulting changes in ϱ^{gc} and, consequently, in the ghost-cell mass flux $f_\varrho^{\mathrm{gc}} = \varrho^{\mathrm{gc}}\, v_z^{\mathrm{gc}}$ allow for an efficient control of the mass influx[3]. Subsequently, the newly found p_{up} is used as the starting value $p_{\mathrm{tot},0}$ for the following timestep. Thus, the downflow regions always lag behind one timestep in the pressure adjustment. Since the pressure corrections for a single timestep are very small, this does not lead to the build-up of significant horizontal pressure gradients.

In order to determine p_{up}, we use the value of $p_{\mathrm{tot},0}$ from the previous timestep as initial guess and follow the procedure outlined above to determine $f_\varrho = \varrho v_z$ in the ghost cells. The resulting mass deficit for the current timestep is then

$$\Delta M_0 = \frac{\iint_{\mathrm{bot}} f_\varrho(x,y)\,dx\,dy}{M_0} \cdot \Delta t. \tag{3.54}$$

---

[3] In the context of a centered difference scheme, a uniform adjustment of $p_{\mathrm{tot},0}$ in up- and downflows simultaneously would affect ghost cell densities of in- and outgoing material in similar ways. The resulting changes in mass influx and outflux would largely cancel, rendering the pressure adjustment ineffective.

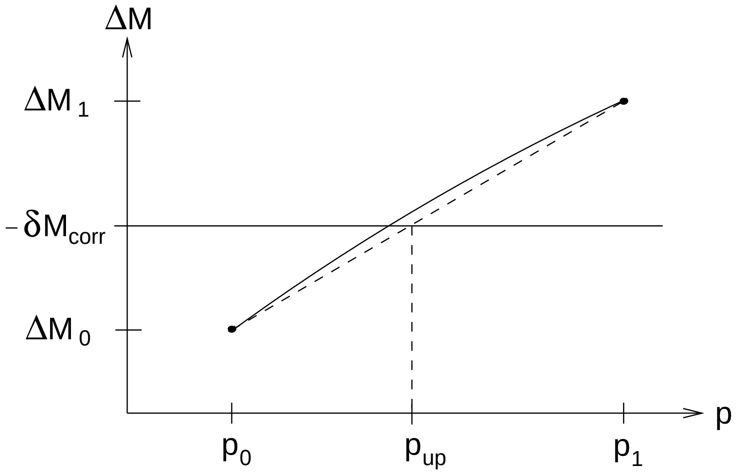

Figure 3.5: *Determining the pressure correction in upflow regions with a secant method: a new value p_{up} is obtained by linear interpolation of the mass deficit function $\Delta M(p)$ between the two previous guesses p_0 and p_1.*

Based on ΔM_0, a first guess for the modified pressure in upflows, p_1, is made, which results in a deficit ΔM_1. This can now be used as the basis for a secant method (see Fig. 3.5) which is iterated until a value of p_{up} is obtained, for which the condition

$$|\Delta M(p_{\mathrm{up}}) + \delta M_{\mathrm{corr}}| < \delta \tag{3.55}$$

with some tolerance δ for the relative mass fluctuations is fulfilled.
We found it sufficient to truncate the secant method after one iteration step. The final value for p_{up} is then given by (see Fig. 3.5)

$$p_{\mathrm{up}} = p_0 - (\delta M_{\mathrm{corr}} + \Delta M_0) \cdot \frac{p_1 - p_0}{\Delta M_1 - \Delta M_0} \tag{3.56}$$

With this method, relative mass fluctuations in our simulations do not exceed the order of 10^{-4}, which seems to be a reasonable compromise between accuracy and time efficiency.

3.4.3 Side boundaries

All quantities are taken to be periodic in both horizontal directions.

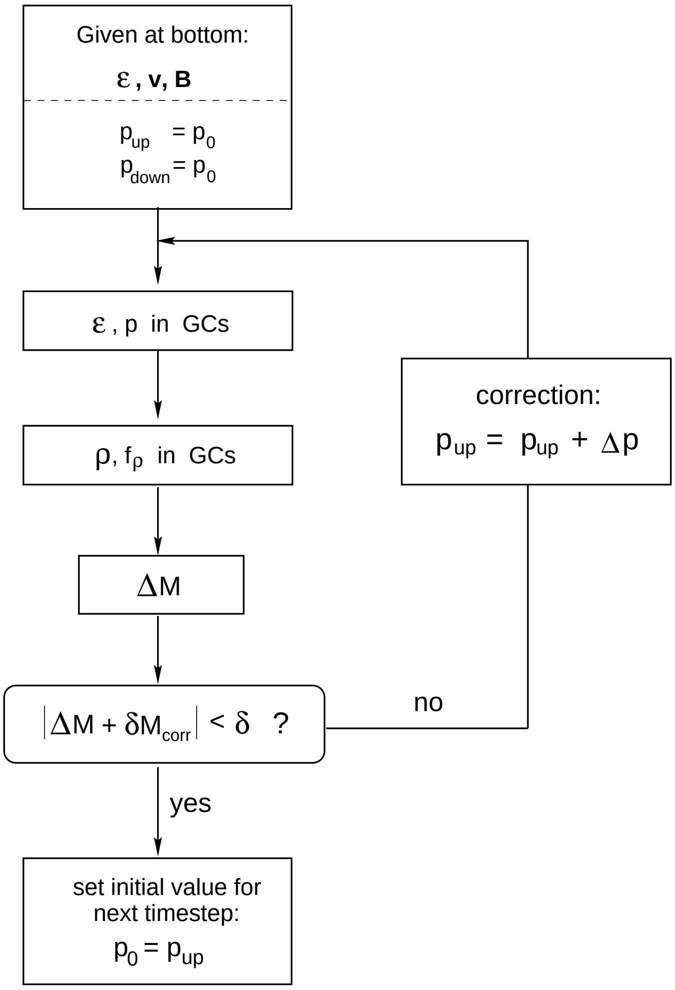
Given at bottom:
ε, v, B
p_up = p_0
p_down = p_0
ε, p in GCs
ρ, f_ρ in GCs
ΔM
|ΔM + δM_corr| < δ ?
no
yes
correction:
p_up = p_up + Δp
set initial value for next timestep:
p_0 = p_up

Figure 3.6: *Flow diagram of the pressure adjustment procedure*

Chapter 4

Numerical treatment of radiative transfer

In this chapter, the numerical methods employed to calculate the radiative source term, $Q_{\rm rad}$, are described. The scheme used to solve the radiative transfer equation is explained in Section 4.1. The opacity binning approach for approximating the frequency dependence is discussed in detail in Section 4.2. Section 4.3 presents test calculations concerning the performance of this method. The procedure in 4.1 works both for monochromatic rays and for frequency-integrated intensities, and whenever a frequency index is used in 4.1, it represents both possibilities.

4.1 The numerical scheme

Numerical simulations of solar magneto-convection require an accurate modelling of the radiative energy exchange, particularly in the photospheric layers where radiative cooling strongly influences the energy balance. As the mean free path of photons becomes large compared to the size of the grid cells with increasing height in the photosphere, radiative transfer can not be described as a local diffusion process. The necessity to propagate intensity information across distances of the order of the photon mean free path makes radiative transfer calculations numerically expensive and often the computation of the radiative source term is the most time-consuming part of a realistic simulation. Therefore, in the choice of a numerical method, efficiency considerations have high priority. Furthermore, the use of a domain decomposition scheme for parallelization demands a solver which is local and reduces the communication overhead to a minimum. Given these requirements, the method of choice is the short-characteristics formal solver (Mihalas et al. 1978, Olson & Kunasz 1987, Kunasz & Olson 1988, Kunasz & Auer 1988). It is based on the discretized form of the formal solution Eq. (2.41) of the radiative transfer equation. In order to calculate the intensity for a certain direction and frequency on a given gridpoint, the transfer equation is solved along the ray segment (short characteristic) between the gridpoint and the nearest upwind intersection of the ray with a cell boundary. The grid on which we solve the radiative transfer coincides with the cell corners of the grid used by the MHD solver. The values of T, p and ϱ on the radiative grid are interpolated from the adjacent MHD grid cells. An example for a short characteristic within a grid cell is shown in Fig. 7. Applying the formal solution to the short characteristic between points F and E, the intensity at point F is given by

$$I_F = I_E\, e^{-\Delta\tau_{EF}} + \int_{\tau_F}^{\tau_E} B(\tau)\, e^{\tau_F - \tau}\, d\tau \quad . \tag{4.1}$$

Here τ measures the optical depth *along the ray*, starting from point F, i.e.

$$\Delta\tau_{EF} = \tau_E - \tau_F = \int_F^E \kappa(s)\varrho(s) ds \quad . \tag{4.2}$$

The first term on the r.h.s. of Eq. (4.1) accounts for the intensity entering the grid cell at point E, attenuated by absorption along the ray segment $\overline{EF}$, while the integral term represents the radiation which is emitted between points E and F. Unless the ray direction is aligned with one of the coordinate directions (or one of the diagonals of the grid cell), the point of intersection E is located on a cell interface and the intensity I_E needs to be interpolated from the gridpoints at the interface corners (points A to D in Fig. 7). On a 2D grid, linear or parabolic[1] interpolation can be used. On the 3D grid used here, we calculate I_E by bilinear interpolation on the rectangle $\overline{ABCD}$.[2]
For the evaluation of the integral contribution, $\int_F^E B(\tau)\, e^{\tau_F - \tau}\, d\tau$, and the optical depth interval, $\Delta\tau_{EF}$, we adopt the linear method described by Kunasz & Auer (1988): density, opacity and source function are approximated as linear functions along the ray segment $\overline{EF}$, which leads to analytical expression for $\Delta\tau_{EF}$ and the integral.[3]

---

[1] An alternative higher-order interpolation is the monotonic interpolation method by Steffen (1990), which eliminates the possibility of unphysical negative intensity values.

[2] The upwind-interpolation involved in the short-characteristics solver introduces an inaccuracy in form of an artificial broadening of rays, which is not present in the usual long-characteristics approach, where for each gridpoint and direction the transfer equation is solved along a ray across the whole domain. The gain in efficiency by using the interpolation, however, is tremendous: While the computational cost of the long-characteristics scheme scales as the total number of gridpoints *times* the typical number of points along a full ray, the short-characteristics solver scales only as the number of gridpoints. As an alternative to linear or bilinear interpolation, a $\kappa\varrho$-weighted interpolation can be used, which tends to reduce the ray-broadening effect at the expense of one additional lookup of κ per gridpoint, frequency, and ray direction.

[3] Bruls et al. (1999) suggest a higher-order method, which uses parabolic interpolation for κ and B and switches to linear interpolation only when strongly non-monotonic behaviour of κ or B is expected. While this approach promises higher accuracy than the linear method, the lack of a stringent switching criterion, which rules out unphysical negative values for source function

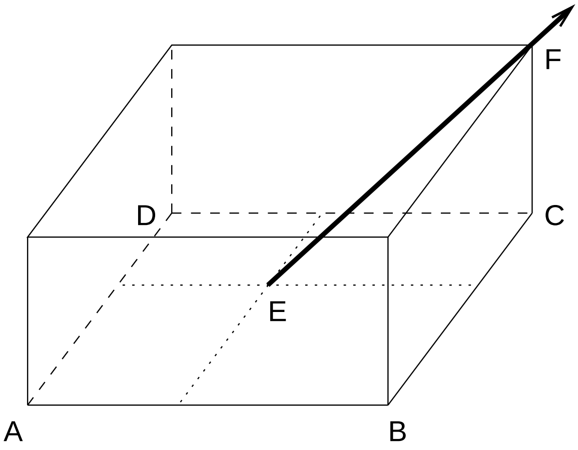

Figure 4.1: *The intensity at gridpoint F is obtained by solving the transfer equation along the short characteristic* $\overline{EF}$. *The intensity at the upwind point E is interpolated from the (already known) intensity values at the surrounding gridpoints, A to D.*

The distance from point F to the nearest upwind intersection of the ray with a cell interface orthogonal to coordinate direction i is given by

$$\Delta s_i = \frac{\Delta x_i}{\mu_i} \qquad (\mu_i \neq 0) \ , \tag{4.3}$$

where μ_i are the directional cosines of the direction considered. For a given ray direction $\boldsymbol{\mu}$, the cell boundary on which the upwind interpolation needs to be performed is determined by the minimum of the Δs_i: the ray in direction $\boldsymbol{\mu}$ intersects the cell interface, which is orthogonal to coordinate direction i, if

$$\Delta s_i = \min(\Delta s_j) \qquad j \in \{1, 2, 3\} \ . \tag{4.4}$$

On a grid with constant mesh width in all coordinate directions, the upwind interface and the interpolation coefficients do not depend on the grid position but are determined by the ray direction alone and can be calculated in advance. Since the interpolation of the upwind intensity requires knowledge of the intensity at the four surrounding gridpoints (points A to D in Fig. 7), the grid must be traversed in a manner which makes sure that the required upwind information is always available. To this end, for a given ray direction, the scheme starts in

---

or opacity, renders it unreliable in simulations where large temperature gradients can lead to strong cell-to-cell variations of κ and B. An alternative way of solving the radiative transfer equation along short characteristics was proposed by Dedner & Vollmöller (2001), who obtained high accuracy by combining an implicit Runge-Kutta method with a higher-order interpolation of the upwind intensity, albeit at higher computational costs compared to the linear method.

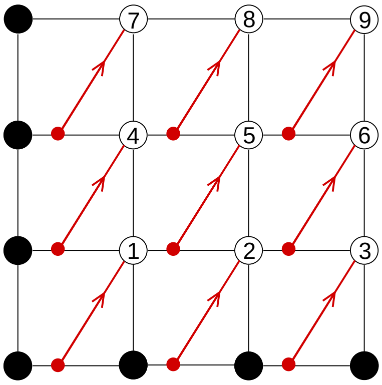

Figure 4.2: *The walking order of the Short Characteristics method in a 2D grid for a ray direction pointing into the upper right quadrant. Black circles represent gridpoints on the upwind boundaries, where the intensity values are assumed to be known.*

each subdomain at those boundaries, through which the radiation flows in (the "upwind" boundaries). The intensity values at these boundaries are assumed to be known. Then the traversal of the subdomain systematically proceeds in the downwind direction, propagating the boundary information across the grid (see Fig. 4.2 for a 2D example). Since the correct initial values on the upwind boundaries of a subdomain are a priori unknown unless these boundaries coincide with the top or bottom of the computational box, this procedure must be iterated until convergence on the boundaries is obtained. As illustrated in Fig. 4.3, the intensities at a given upwind boundary are updated after each iteration with the new values provided by the neighbouring subdomain. Clearly, the number of iterations required depends on the accuracy of the initial guess. We use a linear extrapolation of the boundary values of the previous two timesteps. With this choice, on average 2 - 3 iteration steps per frequency and ray direction are sufficient to keep the relative error in intensity below 10^{-3}.

At the global top and bottom boundaries of the computational domain the incoming intensity must be specified in order to bootstrap the short-characteristics scheme. As long as the medium is optically thin at a given frequency (or frequency bin[4]) ν at the top of the box, the incoming radiation from outside the computational domain is negligible and the boundary condition

$$I_\nu(\boldsymbol{\mu})\,|_{\text{top}} = 0 \qquad \forall\, \mu_z < 0 \tag{4.5}$$

can be used. In the simulations shown in Chapter 5 this assumption is valid for all frequency bins except the one representing the strongest line opacities. For this bin the $\tau_\nu = 1$ level is close to the top of the box and setting the incoming

---

[4] See Sec. 4.2 for a detailed explanation of the concept of frequency bins.

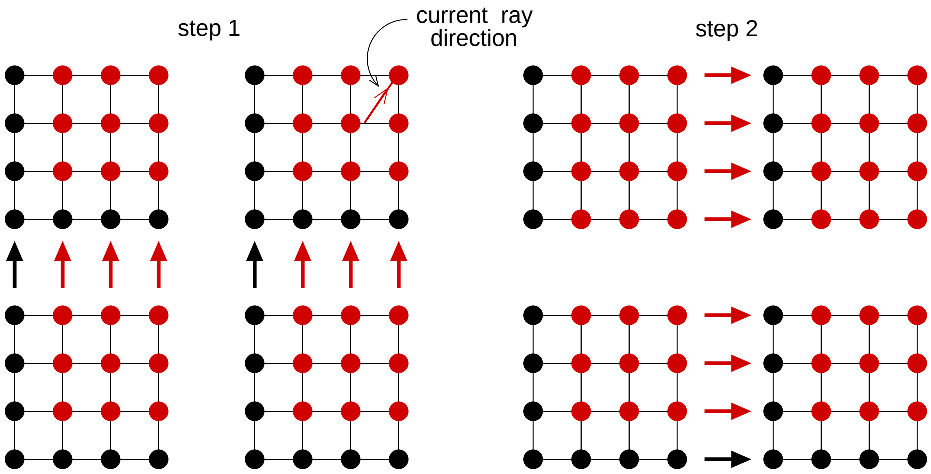

Figure 4.3: *A 2D example for the information exchange between four adjacent subdomains, for a ray pointing into the upper right quadrant. After the subdomains have been traversed independently and simultaneously, each process sends the updated intensities to its neighbour in the downwind direction. Black circles represent old values, red circles contain updated information. Likewise, black and red arrows transfer, respectively, old and new data. For each coordinate direction, the communication is performed in a separate step. After the second step the values in the top right subdomain are completely updated.*

radiation to zero would lead to artificial cooling of the uppermost layers. In order to derive a more realistic boundary condition, we assume that above the computational domain there is a nearly isothermal plane-parallel layer with temperature $T_{\rm top}$, whose optical thickness in the most opaque bin is $\tau_{\rm top}$. According to the formal solution (2.41) of the RTE, the radiation entering the box from such a layer is

$$I_\nu(\boldsymbol{\mu})\,|_{\rm top} = -\frac{1}{\mu_z}\int_0^{\tau_{\rm top}} B_\nu(\tau)\, e^{(\tau_{\rm top}-\tau)/\mu_z}\, d\tau \qquad \forall\, \mu_z < 0 \ . \tag{4.6}$$

Setting $B_\nu(\tau)$ to the constant value $B_\nu(T_{\rm top})$, the integral in Eq. (4.6) yields

$$I_\nu(\boldsymbol{\mu})\,|_{\rm top} = B_\nu(T_{\rm top})\,\left(1 - e^{\tau_{\rm top}/\mu_z}\right) \qquad \forall\, \mu_z < \ \ 0 \ . \tag{4.7}$$

In our simulations we use this relation with $\tau_{\rm top} = 0.2$ and $T_{\rm top} = 4000$ K as boundary condition for the strongest opacity bin.[5] The bottom of the simulation

---

[5] The assumption of a constant temperature is reasonable since the top of the computational domain is located near the temperature minimum. The value $\tau_{\rm top} = 0.2$ corresponds to the optical depth τ_ν of the strong-opacity bin at the same geometrical height in 1D solar standard atmospheres.

μ_x	μ_y	μ_z	weight
$\sqrt{7/9}$	$1/3$	$1/3$	$1/3$
$1/3$	$\sqrt{7/9}$	$1/3$	$1/3$
$1/3$	$1/3$	$\sqrt{7/9}$	$1/3$

Table 4.1: *Direction-cosines and point weights for the A4 angular quadrature of Carlson (1963).*

box is located in the optically thick regions where the diffusion approximation holds. At the bottom, incoming radiation is set to the local value of the source function:

$$I_\nu(\mathbf{x}, \boldsymbol{\mu}) \,|_{\mathrm{bot}} = B_\nu(\mathbf{x}) \qquad \forall\, \mu_z > 0 \ . \tag{4.8}$$

In order to obtain the mean intensity, J, and the radiation flux, $\mathbf{F}$, the intensity $I(\boldsymbol{\mu})$ has to be integrated over the 4π steradian solid angle of the unit sphere. The angular integration is expressed as a quadrature sum over a discrete set of directions, $\boldsymbol{\mu}_m$, with associated point weights, w_m. For each direction and each frequency point (or bin) the short-characteristics scheme described above is performed separately. We use the angular quadrature formulae of type A of Carlson (1963). In this scheme, the directions in one octant are arranged in a triangular pattern and the quadrature is invariant under rotations over multiples of $\pi/2$ around any coordinate axis. A summary of the construction procedure is given by Bruls et al. (1999). For the simulations shown in Chapter 5, the A4 quadrature set with three directions per octant was used. With the quadrature weights normalized to unity and the index m running over the set of directions, mean intensity and radiation flux are then calculated as

$$J = \sum_m w_m I_m \tag{4.9}$$

and

$$\mathbf{F} = 4\pi \sum_m w_m \boldsymbol{\mu}_m I_m \ \ , \tag{4.10}$$

respectively (the frequency index ν has been dropped here).
Once the angular integration has been performed, the radiative heating rate for frequency ν can be derived from the two alternative expressions

$$Q_\nu^J = 4\pi\kappa_\nu\varrho\,(J_\nu - B_\nu) \tag{4.11}$$

and

$$Q_\nu^F = -\nabla\cdot\mathbf{F}_\nu \ \ . \tag{4.12}$$

While the radiation field is defined on cell corners, the MHD solver requires cell-centered (or cell-averaged) values of the radiative heating rate. Cell-centered values for Q^J are obtained by averaging over the values at the eight surrounding cell corners. In the case of Q^F, first average values for the components of $\mathbf{F}$ are calculated on the centers of cell interfaces, then the derivatives are obtained by first-order finite differences between the averaged flux components on opposite cell interfaces.

As pointed out by Bruls et al. (1999), Q^J suffers from severe accuracy problems in the optically thick regime, since here J_ν approaches B_ν and the difference of these two almost equal quantities is amplified by a factor $\kappa_\nu \varrho$ which grows exponentially with depth. On the other hand, Q^F is less accurate than Q^J in the optically thin layers of the upper photosphere, since small inaccuracies in the orientation of the flux vector can lead to significant errors when the divergence of the nearly constant radiative flux is determined, while the difference $J_\nu - B_\nu$ is only slightly affected. Following the suggestion by Bruls et al. (1999), we make a smooth transition from Q^J to Q^F for each frequency (or frequency bin) separately, depending on the local optical depth scale for the frequency considered, using Q^F in regions with $\tau_\nu \geq 0.1$ and Q^J otherwise. The total (frequency-integrated) radiative heating rate is calculated using the hybrid expression

$$Q_{\text{tot}} = \sum_\nu e^{-\tau_\nu/\tau_0}\, Q^J_\nu + (1 - e^{-\tau_\nu/\tau_0})\, Q^F_\nu \tag{4.13}$$

with $\tau_0 = 0.1$.

4.2 Numerical treatment of frequency dependent radiative transfer

The photosphere is the layer within the solar atmosphere where the transition from mainly convective to radiative energy transport occurs. Hence the radiation field plays a crucial role in the overall energy balance of the photosphere and requires a detailed modeling in numerical simulations aiming at a realistic description of the solar conditions. In the framework of (magneto-)convection simulations, the radiation field enters the set of MHD equations via the radiative heating rate per unit volume, Q_{rad}. As outlined in Sec. 2.4, the heating rate is obtained by solving the radiative transfer equation (2.38) for a number of frequencies and directions. From this, $\mathbf{F}_\nu$ (or J_ν) and finally the frequency-integrated heating rate, Q_{rad}, can be derived. Since the total opacity in the solar atmosphere includes the contributions of about 10^6 atomic and molecular spectral lines, roughly 10^6-10^7 frequency points are necessary to model the detailed frequency dependence. While this direct approach is feasible when one-dimensional static models are calculated, the computational cost is intolerable in time-dependent two- or three-dimensional simulations. The most radical simplification of the problem is achieved by the grey approximation, which replaces the frequency-dependent opacity by an averaged value, e.g. the Rosseland mean. The grey approach in combination with the diffusion approximation may be appropriate in the optically dense subphotospheric regions, where the radiative transfer can be described as a local diffusion process; it is, however, unsatisfactory in the optically thinner regions where the radiation transfer becomes nonlocal. Here it is also necessary to explicitly account for line opacities, since line-blanketing effects have a considerable impact on both the photospheric dynamics and the emergent intensities. It is well known that the inclusion of line opacities in calculations of stellar model atmospheres strongly modifies the resulting teperature profiles, leading to considerably cooler outer layers, while the temperature is raised in deeper regions (the line cooling and backwarming effects, e.g. Mihalas 1978, p. 167). Therefore, a statistical treatment of line opacities, which conserves the non-grey character of the radiation transport while drastically reducing the computational expense, is highly desirable. Among the strategies devised to tackle this problem are the method of opacity sampling (see, e.g., Sneden et al. 1976), the concept of Opacity Distribution Functions (ODFs, Strom & Kurucz 1966, Mihalas 1967), and the opacity binning (or multi-bin/multi-group) method (Nordlund 1982, Ludwig 1992, Ludwig et al. 1994). In the context of time-dependent three-dimensional simulations, for which the radiative transfer must be solved for every timestep, the only feasible approach – given the currently available computing resources – is opacity binning, since it implies the most drastic reduction in computational cost and allows for a satisfactory approximation of the frequency-dependence with only a few representative frequency bins.

Since our simulation project aims at simulations that include the upper photospheric layers, where the effects of frequency-dependence are expected to be most pronounced, the implementation of the opacity binning method and its inclusion in the radiative transfer module was mandatory. While the opacity binning approach has been tested and sucessfully applied to calculations of 1D static model atmospheres (Ludwig 1992), the application in the context of time-dependent 2D/3D simulations is accompanied by new sources of errors not encountered in the static 1D case like, for instance, strong lateral variations of the atmospheric properties. In order to test the performance of our implementation of the multi-bin method and gain confidence in the applicability of this approach in our simulations, we performed a series of tests of opacity binning for several 1D and 2D cases with the solution based on Opacity Distribution Functions (ODFs) serving as the reference solution. In the following two sections, the ODF concept and our implementation of the opacity binning method are described. The test results are presented in Sec. 4.3.

We always assume local thermodynamic equilibrium (LTE), implying $S_\nu = B_\nu$, thereby neglecting scattering effects. Line scattering becomes important in chromospheric heights where radiative cooling takes place in a few strong spectral lines, but these regions are currently beyond the scope of our project. The assumption of LTE also implies that the number densities of ions and the population numbers of excitation states are instantaneous functions of the local thermodynamical state of the system only. For this reason, the opacities can be obtained from pre-compiled tables without having to solve the system of rate equations for each gridpoint and timestep during a simulation run, which is an important requirement for the practicability of the aforementioned methods.

4.2.1 Opacity distribution functions

The concept of opacity distribution functions (Strom & Kurucz 1966, Mihalas 1967) is based on the fact that physically relevant quantities of the radiation field like mean intensity, $J = \int J_\nu d\nu$, and total heating rate, $Q = 4\pi\varrho \int \kappa_\nu (J_\nu - B_\nu) d\nu$, are integrals over frequency and hence should not depend crucially on the detailed frequency structure of the opacity. The basic idea of the ODF approach is to replace the complicated opacity line spectrum by a (piecewise) smooth function which approximately reproduces the correct frequency integrals. In the following, the procedure for obtaining ODFs from the detailed spectrum is illustrated for the mean intensity, J, in a 1D plane-parallel atmosphere.

Using the wavelength λ as independent variable, the monochromatic mean intensity is given by

$$J(z,\lambda) = \frac{1}{2} \int_0^\infty B(z',\lambda)\, E_1 \left|\tau_\lambda(z') - \tau_\lambda(z)\right|\, \kappa(z',\lambda)\varrho(z')dz' \qquad (4.14)$$

where z is the geometrical height, $\tau_\lambda(z) = -\int_\infty^z \kappa(z',\lambda)\,\varrho(z')dz'$ the monochromatic optical depth, and $E_1(x) = \int_x^\infty t^{-1}e^{-t}dt$ the first exponential integral (see e.g. Mihalas 1978, p. 40). Now the λ-axis is divided into typically $10^2 - 10^3$ intervals $\Delta\lambda_i$ such that, within each interval, the detailed wavelength dependence of $B(z,\lambda)$ can be neglected. The contribution, J_i, of a particular interval to the wavelength-integrated mean intensity is then given by

$$J_i(z) = \int_{\lambda_i}^{\lambda_i+\Delta\lambda_i} d\lambda \int_0^\infty B_i(z')E_1\left|\tau_\lambda(z') - \tau_\lambda(z)\right| \kappa(z',\lambda)\varrho(z')dz' \;\;, \tag{4.15}$$

where $B_i(z)$ is a mean value of $B(z,\lambda)$ taken over $\Delta\lambda_i$. Since $\tau = -\int_\infty^z \kappa\,\varrho\,dz$, the wavelength enters the integrand solely via $\kappa(z,\lambda)$ and the factor $E_1\kappa\varrho$ is a (complicated) function f of $\kappa{\cdot}\varrho$ alone. If it is assumed that, within each interval, the wavelength dependence of the opacity is independent of depth and that a relation of the form

$$\kappa(z,\lambda) = Z(z)\cdot L(\lambda) \tag{4.16}$$

holds, we then have

$$J_i(z) = \int_{\lambda_i}^{\lambda_i+\Delta\lambda_i} d\lambda \int_0^\infty B_i(z')\, f(L(\lambda)Z(z')\varrho(z'))\,dz' \tag{4.17}$$

$$= \int_{\lambda_i}^{\lambda_i+\Delta\lambda_i} g(L(\lambda))\,d\lambda \;\;. \tag{4.18}$$

with $g(L)$ representing the spatial integral, which, for a given height z, only depends on the value of L. Using a discrete approximation of the above integral,

$$J_i(z) = \sum_{j=1}^{N} g(L(\lambda_{ij}))\Delta\lambda_{ij} \;, \tag{4.19}$$

with $N \approx 10^4$ in order to resolve the detailed structure of $L(\lambda)$, the sum is rearranged according to a discretization L_k of L: the subintervals $\Delta\lambda_{ij}$ are grouped in such a way that for given k those subintervals $\Delta\lambda_{ij}$, for which $L(\lambda)$ lies within $\Delta L_k = [L_k, L_{k+1}[$, constitute a separate subset, $\Delta\lambda_{i\,j(k)}$ (see Fig. 4.4).
Thus,

$$J_i(z) = \sum_k g(L_k)\sum_j \Delta\lambda_{i\,j(k)} \tag{4.20}$$

$$= \sum_k g(L_k)w_k\cdot\Delta\lambda_i \;\;. \tag{4.21}$$

The weight factors $w_k = \sum_j \Delta\lambda_{i\,j(k)}/\Delta\lambda_i$ can be interpreted as the probability for L to lie inside the interval ΔL_k when randomly choosing a wavelength $\lambda \in \Delta\lambda_i$. The rearrangement of the sum in Eq. (4.19) is equivalent to a reordering of $L(\lambda)$

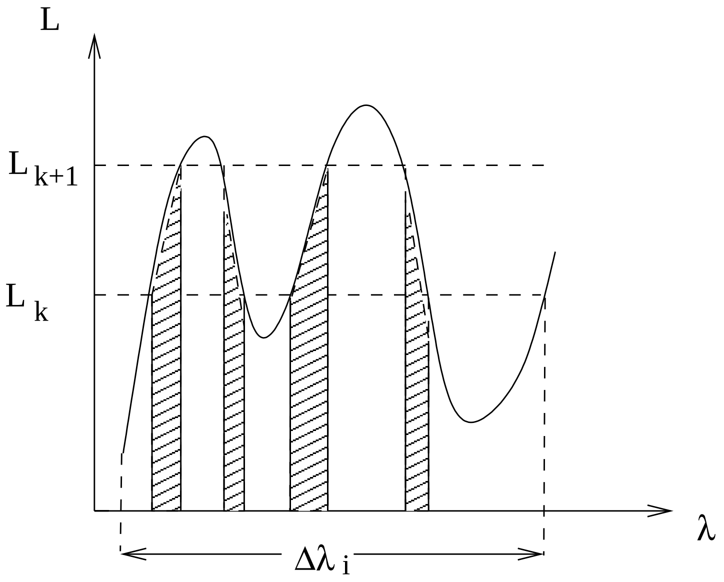

Figure 4.4: *Sorting of wavelengths according to a discretization of L. The hatched areas mark those parts of the ODF interval* $\Delta\lambda_i$ *for which the opacity values lie in the interval* $[L_k, L_{k+1}[$. *They are subsequently reordered to form subinterval* $\Delta\lambda_{i\,j(k)}$.

within $\Delta\lambda_i$, the opacity values being sorted according to their strength. This results in a smooth, monotonous function, $K(\lambda)$. If $\Delta\lambda_i$ is mapped onto the unit interval $[0,1]$, the corresponding function $\tilde{K}(w)$ ($w \in [0,1]$) is a distribution function that determines the integral probability of finding an opacity value $\tilde{K}$ or less (see Fig. 4.5). Adopting this notation, one obtains

$$J_i(z) = \Delta\lambda_i \cdot \int_0^1 g(\tilde{K}(w))\, dw \simeq \Delta\lambda_i \cdot \sum_{l=1}^{M} g(\tilde{K}_l)\Delta w_l \quad . \tag{4.22}$$

In practice, a moderate number of steps ($M \approx 10-12$) is sufficient to approximate the smooth function $\tilde{K}(w)$.

In general the transfer equation is solved separately for each ODF-step with indices i,l :

$$\frac{dI_{i\,l}}{ds} = -\kappa_{i\,l}\varrho\,(I_{i\,l} - B_i) \tag{4.23}$$

The total wavelength-integrated intensity is then given by the weighted sum over all ODF-intervals $\Delta\lambda_i$ and all steps l within each interval:

$$I_{\text{tot}} = \sum_i \Delta\lambda_i \sum_l w_l I_{i\,l} \tag{4.24}$$

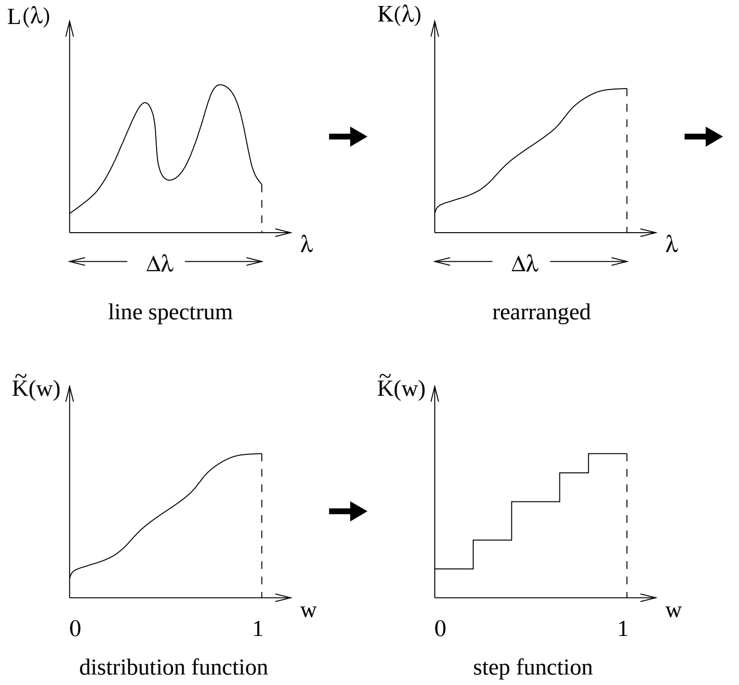

Figure 4.5: *From the wavelength-dependent opacity to the tabulated ODF: Within ODF interval $\Delta\lambda$, the detailed line spectrum is rearranged to form a monotonically increasing function. The corresponding integral probability distribution is then approximated by a step function.*

The step functions κ_{il} for all $\Delta\lambda_i$ are available in tabulated form on a (p, T) grid. Compared to evaluating the expression in Eq. (4.19), the computational effort has been reduced by a factor 10^3. However, Eq. (4.16), which is the crucial prerequisite for the simplification, does not hold strictly. Changes in the states of excitation and ionisation of the gas, overlapping lines of two elements with different opacity variations with depth, or relative line shifts due to velocity gradients lead to changes of the line spectrum with height within a single ODF-interval, $\Delta\lambda_i$. While calculations of static model atmospheres (Gustafsson et. al. 1975) showed good agreement between ODF-based results and models taking into account the detailed line spectrum, velocity gradients may introduce an additional error in time dependent MHD-simulations. A systematic study of this effect for typical velocity gradients in the solar photosphere will be necessary to assess the magnitude of the incurred error.[6] In the limit of vanishing ODF interval sizes, $\Delta\lambda_i \to 0$, the exact solution is recovered, since B and κ approach constant values within each interval (implying that the requirement (4.16) is trivially fulfilled).

---

[6] A possible remedy for the error caused by relative doppler-shifts of spectal lines was outlined by Baschek et al. (1997) and Wehrse et al. (2000) who, for simplified models, derived an approximate description of the radiative transfer in moving media.

4.2.2 The opacity binning method

In this section we describe the opacity binning approach proposed by Nordlund (1982) in the form developed by Ludwig (1992). The basic idea is to divide the frequency spectrum into typically 3-5 non-contiguous subsets (called "bins" or "groups"), Ω_i, according to the strength of the corresponding opacities. This way, continuum opacities and lines of different strengths are pooled in seperate bins and represented by bin-specific average opacities. Introducing the bin-integrated quantities $I_i = \int_{\Omega_i} I_\nu d\nu$ and $B_i = \int_{\Omega_i} B_\nu d\nu$, and assuming that the classification into bins remains fixed for all points along a ray, the radiative transfer equation can for each bin be written in the form

$$\begin{aligned} \frac{dI_i}{ds} &= -\int_{\Omega_i} \kappa_\nu \varrho (I_\nu - B_\nu) d\nu \\ &\simeq -\overline{\kappa}_i \varrho (I_i - B_i) \ . \end{aligned} \tag{4.25}$$

The introduction of a bin-averaged opacity $\overline{\kappa}_i$ in Eq. (4.25) is the essential step in the opacity-binning approach, because here a large part of the frequency integration has been done before the integration along the ray is carried out. For a given ray, Eq.(4.25) is solved once for each bin, thereby drastically reducing the computational effort. This procedure is strictly correct only if κ_ν is constant over the whole bin, so one makes the implicit assumption that the depth-dependence of κ_ν (and thus of the τ_ν scales) is similar for the frequencies within one bin. Because of the inevitable variations of κ_ν within a given bin, it is necessary to define a bin-averaged opacity. In optically thick regions the angle-averaged intensity J_ν approaches B_ν and the bin-specific heating rate, $Q_{\mathrm{rad},i} = \int_{\Omega_i} \kappa_\nu \varrho (J_\nu - B_\nu) d\nu$, tends to zero, so the definition of a mean opacity is not critical in this regime. The obvious choice is the Rosseland mean, because radiative transfer is effectively local and can be described as a diffusive process for $\tau_\nu \gg 1$:

$$\mathbf{F}_\nu = -\frac{4\pi}{3\kappa_\nu} \frac{dB_\nu}{dT} \nabla T \ . \tag{4.26}$$

For the bin-integrated radiative flux one obtains

$$\mathbf{F}_i = -\frac{4\pi}{3\overline{\kappa}_R} \int_{\Omega_i} \frac{dB_\nu}{dT} d\nu \, \nabla T \tag{4.27}$$

with the Rosseland mean defined by

$$\frac{1}{\overline{\kappa}_{R,i}} = \frac{\int_{\Omega_i} \frac{1}{\kappa_\nu} \frac{dB_\nu}{dT} d\nu}{\int_{\Omega_i} \frac{dB_\nu}{dT} d\nu} \ . \tag{4.28}$$

This definition gives the correct bin-integrated radiative fluxes.

In the regime $\tau_\nu \lesssim 1$, the diffusion approximation breaks down and the Rosseland mean is no longer applicable. Being a harmonic mean, it tends to underestimate the line opacities. For optically thin regions, an averaging presciption can be obtained by requiring that the correct energy balance within each bin is maintained:

$$\int_{\Omega_i} \kappa_\nu (J_\nu - B_\nu) d\nu = \overline{\kappa} \int_{\Omega_i} (\overline{J}_\nu - B_\nu) d\nu \ . \tag{4.29}$$

Here, $\overline{J}_\nu$ is the integrated intensity that results from using $\overline{\kappa}$ instead of κ_ν (the source function is still frequency-dependent, hence the index ν in $\overline{J}_\nu$). If one further assumes that

$$\int_{\Omega_i} \overline{J}_\nu d\nu \simeq \int_{\Omega_i} J_\nu d\nu \ , \tag{4.30}$$

then Eq. (4.29) is equivalent to

$$\int_{\Omega_i} (\kappa_\nu - \overline{\kappa})(J_\nu - B_\nu) d\nu = 0 \ . \tag{4.31}$$

J_ν is not known a priori, but for $\tau_\nu \ll 1$ it can be approximated by expanding $B_\nu(\tau_\nu)$ in a Taylor series and applying the Λ_ν-operator that connects B_ν and J_ν [see e.g. Mihalas (1978), p. 59 for details]. The result is

$$J_\nu - B_\nu \simeq -\frac{1}{2} B_\nu \ . \tag{4.32}$$

By inserting Eq. (4.32) into Eq. (4.31) and solving for $\overline{\kappa}$, the Planck mean,

$$\overline{\kappa}_{P,i} = \frac{\int_{\Omega_i} \kappa_\nu B_\nu d\nu}{\int_{\Omega_i} B_\nu d\nu} \ , \tag{4.33}$$

is obtained. This “derivation” is far from rigorous and should be understood as an indication that the Planck mean can be expected to yield a reasonable approximation of Q_{rad} for $\tau_\nu \ll 1$.

Ludwig (1992) proposes a hybrid scheme that models a steep transition from $\overline{\kappa}_P$ to $\overline{\kappa}_R$ at a threshold optical depth of $\tau_0 = 0.35$:

$$\overline{\kappa}_i = 2^{-\frac{\tau_i}{\tau_0}} \overline{\kappa}_{P,i} + \left(1 - 2^{-\frac{\tau_i}{\tau_0}}\right) \overline{\kappa}_{R,i} \ . \tag{4.34}$$

The index i indicates that the means $\overline{\kappa}_{P,i}$ and $\overline{\kappa}_{R,i}$ are to be evaluated for each frequency bin, Ω_i. For each bin, $\overline{\kappa}_i$ can be tabulated on a (p, T) grid for subsequent use in simulations. Since the optical depth τ_i corresponding to local values of p and T is not known prior to a simulation run, it has to be estimated. Assuming that the gas is hydrostatically stratified and that the depth-dependence of $\overline{\kappa}_{R,i}\varrho$ is dominated by an exponential increase of ϱ with geometrical depth, Ludwig (1992) found the approximate expression

$$\tau_i \simeq \frac{\overline{\kappa}_{R,i}\, p}{g_\odot} \ , \tag{4.35}$$

where $g_\odot$ is the gravitational acceleration in the photosphere.

A key step in the opacity binning method is the choice of an appropriate criterion for sorting frequencies into bins. The rationale for any sorting rule must be to group together opacities that are of the same order of magnitude and show similar behaviour as a function of depth. A simple choice is the so-called *κ-sorting*; starting from the choice of a fixed height z_0 (or, alternatively, a representative pair of values p_0 and T_0) in a reference atmosphere, the frequency bins are then constructed according to the spectral shape of $\kappa_\nu(z_0)$. A number of threshold values κ^l (the superscript l labeling the bin, not to be mistaken as an exponent), which divide the range of opacity values into intervals, are selected. A frequency ν becomes part of a given bin if $\kappa_\nu(z_0)$ lies within the corresponding interval:

$$\nu \in \Omega_l \qquad \text{if} \qquad \kappa^l \leq \kappa_\nu(z_0) < \kappa^{l+1} \quad . \tag{4.36}$$

A reasonable choice for z_0 is the height where the continuum at 5000 Å forms, $\tau_{5000}(z_0) \approx 1$. Here a large part of the emerging flux originates and the energy exchange between gas and radiation field plays an important role, requiring an accurate modelling of the opacities. The threshold values κ^l have to cover several orders of magnitude in order to account for the line opacities becoming important at greater heights.

It is a disadvantage of the κ-sorting procedure that it does not provide a reasonable selection criterion for frequencies that are optically thick ($\tau_\nu \gg 1$) at z_0. The opacity values at z_0 for such frequencies have no significant impact on the radiative energy exchange, since the main contribution for a given frequency ν to the heat exchange comes from a height around $\tau_\nu \approx 1$. It seems therefore preferable to sort the frequencies according to the opacity in the layer $\tau_\nu \approx 1$ instead of using a fixed geometrical reference height. This *τ-sorting*, suggested by Ludwig (1992), applies the following strategy. First a 1D reference atmosphere is chosen. Then $\kappa_\nu \varrho$ is integrated along z for all frequencies and the geometrical height corresponding to $\tau_\nu = 1$ is determined. Measuring height in terms of a reference optical depth scale τ_{ref} (e.g. the Rosseland optical depth or the continuum optical depth at 5000 Å), threshold heights τ^l_{ref} are chosen. Then ν belongs to bin Ω_l, if $\tau_\nu = 1$ is reached within the corresponding interval of the reference optical depth:

$$\nu \in \Omega_l \qquad \text{if} \qquad \tau^l_{\text{ref}} \geq \tau_{\text{ref}}(\tau_\nu = 1) > \tau^{l+1}_{\text{ref}} \quad . \tag{4.37}$$

If one assumes that the τ_ν scales are mainly determined by an exponential depth-dependence of ϱ, then an approximate relation similar to Eq. (4.35) holds. This implies that τ-sorting, like κ-sorting, groups together opacities of the same order of magnitude. If τ-sorting is applied, all opacity values between $\tau_\nu = 0$ and $\tau_\nu = 1$ contribute to the selection process, in contrast to κ-sorting, and the frequencies of one bin have the same optical depth for the most relevant height, namely

$\tau_{\text{ref}}(\tau_\nu = 1)$. Consequently, one may expect that in the region $0 < \tau_\nu \leq 1$, where a non-grey description of radiative transfer is important, the τ_ν-scales within a given bin are similar, which is the major requirement for the validity of the opacity-binning approach. For greater depths, the way frequencies are gathered may be inappropriate, but this shortcoming is less severe as radiation transfer becomes increasingly grey in these regions.

The τ-sorting procedure can be realized in a convenient way by using ODFs. For each ODF step with indices (i, j), $\kappa_{ij}\varrho$ is integrated along z, which gives τ_{ij} as a function of height in the reference atmosphere (see Fig. 4.6). The ODF steps are then sorted into bins Ω_l. Bin-integrated quantities are obtained as weighted sums over the ODF steps in a given bin, viz.

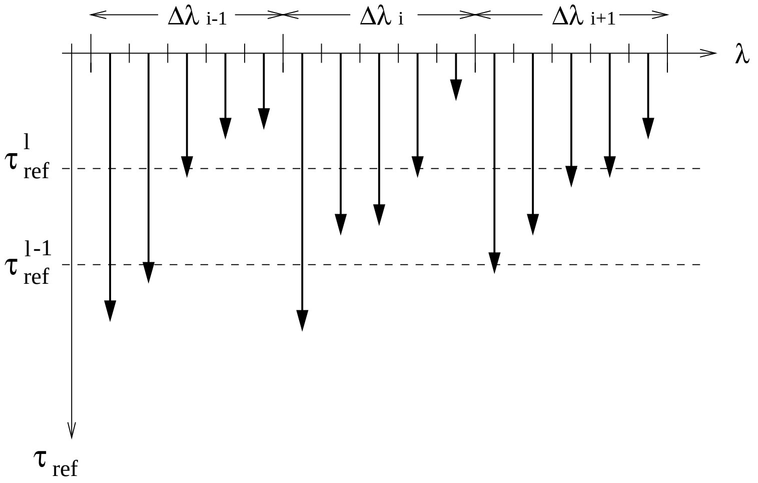

Figure 4.6: *Schematic illustration of the τ-sorting procedure using ODFs. Within each ODF interval $\Delta\lambda_i$, the ODF steps $\Delta\lambda_{ij}$ are sorted to frequency bins Ω_l, depending on the height where $\tau_{ij} = 1$ is reached (indicated by bold arrows).*

$$B_l = \sum_i \Delta\lambda_i B_{\Delta\lambda_i} \sum_{j(i,l)} w_{j(i,l)} \tag{4.38}$$

and

$$\overline{\kappa}_{P,l} = \frac{1}{B_l} \sum_i \Delta\lambda_i B_{\Delta\lambda_i} \sum_{j(i,l)} w_{j(i,l)} \kappa_{i\,j(i,l)} \quad , \tag{4.39}$$

where, for a given bin index l, the index $j(i, l)$ runs over those steps in $\Delta\lambda_i$, which are elements of Ω_l. $B_{\Delta\lambda_i}$ denotes the average of B over the ODF interval $\Delta\lambda_i$.

In contrast to the ODF approach, the opacity binning solution can not be expected to converge to the exact solution (i.e. the solution based on the detailed reference spectrum which was used in the sorting process) in the limit of a very large number of opacity bins. This is due to the fact that, even for infinitely small intervals between bin-levels $\tau^l_{\rm ref}$ (or κ^l in the case of κ-sorting), each bin will comprise frequencies from different parts of the spectrum with different height profiles of the corresponding opacities. It should be noted that using ODFs as basis for sorting frequencies may introduce an additional error since the rearrangement of spectral lines inherent in the ODF concept might affect the way frequencies are classified. Since the ODF solution approximates the exact solution well, the error incurred this way is probably small compared to the consequence of the binning procedure.

The choice of a reference atmosphere is another possible source of error connected with the τ-sorting scheme. It is plausible that the opacity binning method with τ-sorting shows good results in calculations of static 1D model atmospheres if the "exact" solution (i.e., the 1D atmosphere resulting from the ODF approach) is chosen as the reference atmosphere. In multidimensional time-dependent simulations, however, the physical parameters may deviate considerably from a 1D reference stratification. As a consequence, the assignment of frequencies to bins might lead to an inappropriate representation of the opacities. In order to test the applicability of the τ-sorting procedure in non-planeparallel cases, we performed test calculations for some typical two dimensional situations. These tests are presented in Sec. 4.3.2.

4.3 Tests of the opacity binning method

This section presents the results of tests that were carried out in order to assess the performance of our implementation of the opacity binning method. While the systematic study by Ludwig (1992) used temperature structures of one-dimensional radiative-equilibrium atmospheres as a criterion for the quality of opacity-binning models, we focus on the radiative heating rate, which is the quantity that directly enters the system of MHD equations. In Sec. 4.3.1 we present one-dimensional test calculations, which aim at an optimal approximation with a small number of bins. These tests are extended to typical two-dimensional situations in Sec. 4.3.2, where a simplified flux-sheet model and a snapshot from a time-dependent 2D simulation are considered. In Sec. 4.3.3 we study the convergence properties of different opacity binning schemes in the limit of a large number of bins and present an approach for defining average opacities which can enhance the quality of the opacity binning approximation. In Sec. 4.3.4 we give an estimate for the characteristic timescales connected with the errors occuring in opacity binning calculations.

We calculate $Q_{\rm rad}$ by solving the radiative transfer equation with the linear short-characteristics method described in Sec. 4.1. All tests in plane-parallel atmospheres use a Gaussian quadrature with ten direction-cosines per hemisphere for the angular integration (Lowan et al. 1942). For the two-dimensional calculations of Sec. 4.3.2, we use linear interpolation of the upwind intensity and the A8 angular quadrature of Carlson (1963) with ten ray directions per octant.

As reference solutions serving as a basis for evaluating the opacity binning results, we use the radiative heating rates calculated using ODFs. ODFs also serve as the reference "line" spectrum on which the multi-bin sorting procedure is performed. We use the ODF table for solar composition and a microturbulence parameter of 2 km s^{-1}, which is part of the ATLAS9 stellar atmosphere package of Kurucz (1993). The ODFs cover the wavelength range from 8.98 nm to 10000 nm, which is divided into 328 intervals. The interval size is roughly proportional to wavelength. In the most relevant spectral range 300 - 1000 nm the spectral resolution is 10 nm. Within each of the 328 ODF intervals, the distribution function is approximated by 12 steps, i.e., the line spectrum is approximated by 328×12 "frequency points" (the frequency information is lost within each ODF interval as a result of the reordering of opacity values). The ODFs are tabulated as functions of gas pressure and temperature. The continuum opacities were extracted from the relevant routines of the ATLAS9 code (Kurucz 1993) and stored as a table on the same pressure/temperature grid as used for the ODFs.

4.3.1 1D tests

As a first step, the ODF and opacity binning methods have been applied to a one-dimensional solar model atmosphere (Maltby et al. 1986). The main goal of this test is to verify the result of Ludwig (1992), who found that a 5-bin description gives a satisfactory approximation of the ODF reference solution.

In order to illustrate the importance of non-grey radiative transfer, Fig. 4.7 shows the frequency-integrated radiative heating rate, Q_{rad}, calculated with ODFs and, for comparison, using the Rosseland mean opacity.

Both curves show the characteristic cooling located around the height $z = 0$ (corresponding to $\tau_{5000} = 1$), where the atmosphere becomes transparent in the visible continuum and most of the emerging solar flux originates. The largest difference between the curves is found in the optically thin region around $0 \lesssim z \lesssim 200$ km. Here Q_{ODF} is less negative than Q_{grey}, which is due to the backwarming effect of the spectral lines. The line-cooling effect in higher layers, accompanying the backwarming, can be seen in Fig. 4.8. Here the difference $Q_{\text{ODF}} - Q_{\text{grey}}$ is plotted as a function of the logarithmic gas pressure, which serves as a height scale. The transition from backwarming to line-cooling takes place at $\log p \approx 4.35$, which corresponds to a geometrical height of $z \approx 200$ km and a continuum optical depth of $\log \tau_{5000} \approx -1.7$. In order to assess the plausibility of these values, Fig. 4.9 shows the corresponding flux-constant temperature stratifications that result from the ATLAS9 stellar atmosphere code. The transition from backwarming to line-cooling takes place at $\log p \approx 4.0$ which agrees rather well with the result for our test atmosphere.

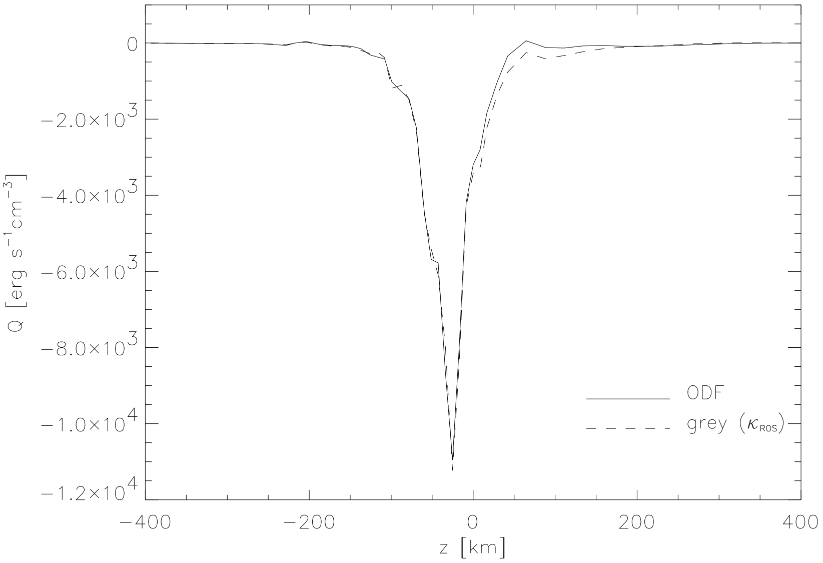

Figure 4.7: *The total radiative heating rate as a function of geometrical height for the 1D atmosphere of Maltby et al. (1986). The ODF solution and the grey case with the Rosseland mean opacity are shown. In the height range between* $z = 0$ *and* $z = 200$ *km, the line opacities lead to a backwarming effect of the ODF case relative to the grey one.* $z = 0$ *corresponds to the continuum optical depth* $\tau_{5000} = 1$.

Based on the use of ODFs, opacity binning and τ-sorting have then been applied, with $Q_{\rm ODF}$ serving as the quasi-exact reference solution. Fig. 4.10 shows $(Q - Q_{\rm ODF})/\varrho$ for the Rosseland solution and for τ-sorted multi-bin models with the number of opacity bins increasing from 3 to 6. The threshold values separating the bins in the multi-bin models are spaced apart by $\Delta \log \tau_{5000} = 1.5$, the lowest threshold value being $\log \tau_{5000} = 0$ for all models, i.e. $\log \tau^l = -l \cdot \Delta$ with $l = 0, \cdots, N-2$ and $\Delta = 1.5$, where N is the number of bins. This choice corresponds to a roughly equidistant spacing of levels on the geometrical height scale as well, with $\Delta z \approx 150 \cdots 200$ km. The 3- and 4-bin models show a strong cooling above, respectively, $z \approx 550$ km and $z \approx 700$ km. In these cases, the strong line opacities which become transparent in the upper part of the atmosphere are only crudely represented by the highest opacity bin, which results in a bad approximation of $Q_{\rm rad}$ at large heights. In the height range $0 < z < 700$ km the models with 5 and 6 bins are clearly more accurate than the grey solution. The quality of the the 5- and 6-bin approximations is comparable, significant differences occur only above $z \approx 600$ km as a result of the additional threshold of the 6-bin model at $\log \tau_{5000} = -6$ (corresponding to $z \approx 760$ km). Likewise, the 3- and 4-bin solutions differ from the 6-bin model only in the height range

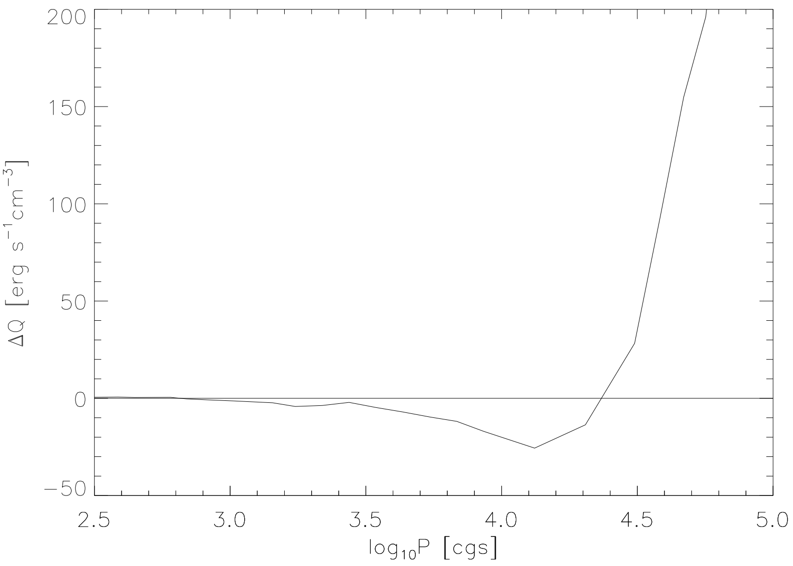

Figure 4.8: *The difference* $Q_{\mathrm{ODF}} - Q_{\mathrm{grey}}$ *plotted against the logarithmic pressure scale; the height in the atmosphere increases towards the left. The transition from backwarming to line-cooling occurs at* $\log_{10} p \approx 4.35$*, which corresponds to* $z \approx 220$ *km.*

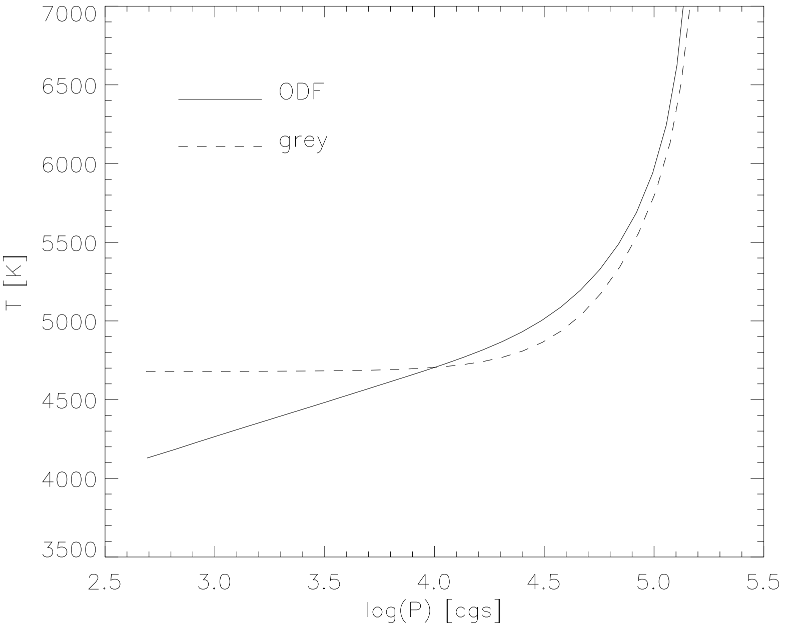

Figure 4.9: *Flux-constant temperature stratifications resulting from ATLAS9, for the ODF-based solution and the grey case using the Rosseland mean opacity; the hight in the atmosphere increases towards the left. The inclusion of line opcaities in the ODF-solution leads to considerable cooling in the upper layers and a temperature increase below.*

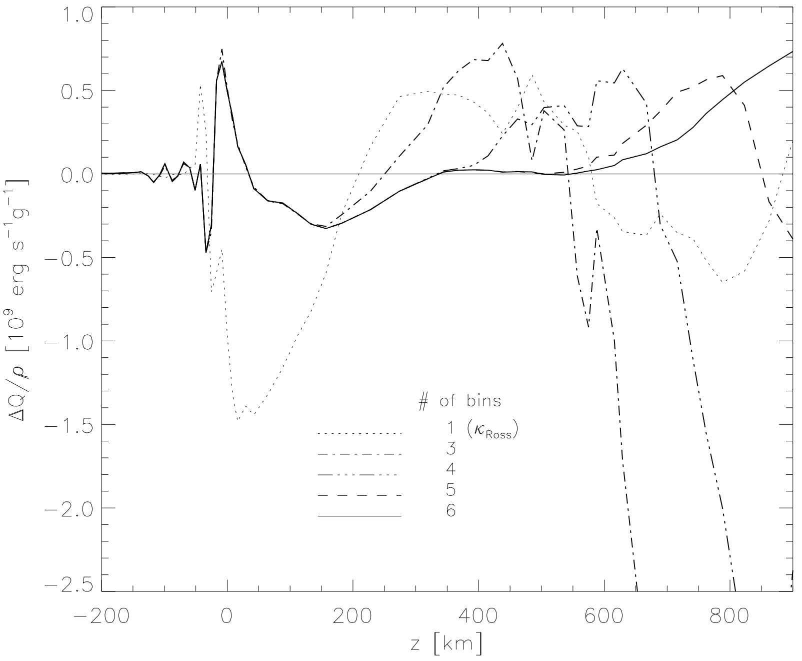

Figure 4.10: $(Q - Q_{\rm ODF})/\varrho$ *as a function of height* z*. The grey solution and four* τ*-sorted multi-bin models with 3,4,5, and 6 frequency bins are shown. The spacing between threshold levels separating the bins is* $\Delta \log \tau_{5000} = 1.5$*, and the lowest level is* $\log \tau_{5000} = 0$ *for all multi-bin cases.*

above, respectively, $z \approx 150$ km and $z \approx 400$ km, corresponding that parts of the atmosphere which are covered by the respective highest bins of the 3- and 4-bin models. Fig. 4.11 shows the attempt to model $Q_{\rm rad}$ with a small number of bins distributed equidistantly over the height range $z > 0$. The threshold values (in $\log \tau_{5000}$) were chosen as follows:

2 bins: -3
3 bins: -1.5 , -4.5
4 bins: -1, -3,-5

It turns out that the 2-bin model is less accurate than the Rosseland solution. Obviously, switching from the Rosseland to the Planck mean results in a bad representation of opacities in cases where the number of bins is small and the classification of frequencies is accordingly crude. While the 3-bin solution shows a relatively large error above $z \approx 600$ km, the performance of the 4-bin solution is comparable to the cases with 5 and 6 bins in Fig. 4.10. Calculations with larger numbers of equidistantly spaced bins did not show any significant further improvement (see Sect. 4.3.3). So, for the atmosphere model considered here, the

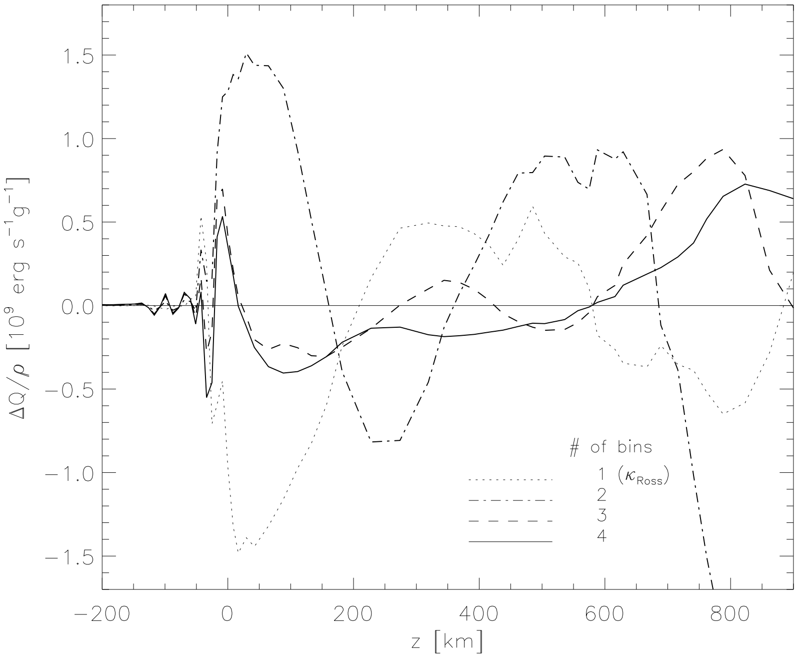

Figure 4.11: *$(Q - Q_{\mathrm{ODF}})/\varrho$ as a function of height z. The grey solution and τ-sorted multi-bin models with 2, 3, and 4 frequency bins evenly distributed over the range* $\log \tau_{5000} < 0$ *are shown.*

optimal number of frequency bins is found to be 4 – 6. However, as the results of Fig. 4.10 suggest, the optimal number depends on the vertical extent of the atmosphere considered. The computational domain of the simulations discussed in Chapter 5 approximately extends to a height of 600 km above $\tau_{5000} = 1$, and a four-bin modelling was found to be appropriate (see Chapter 5 for details of the simulation setup).

In the optically thick regime, $\tau_{5000} > 1$ ($z < 0$), the solutions for different total numbers of bins agree well with each other, the relative error $|(Q - Q_{\mathrm{ODF}})/Q_{\mathrm{ODF}}|$ does not exceed the order of 10^{-2}. This is in agreement with the fact that the frequency dependence has almost no influence on the radiative transfer at large optical depths and any multi-bin model can be expected to yield good results at these depths as long as the Rosseland mean is used for calculating bin-averaged opacities.

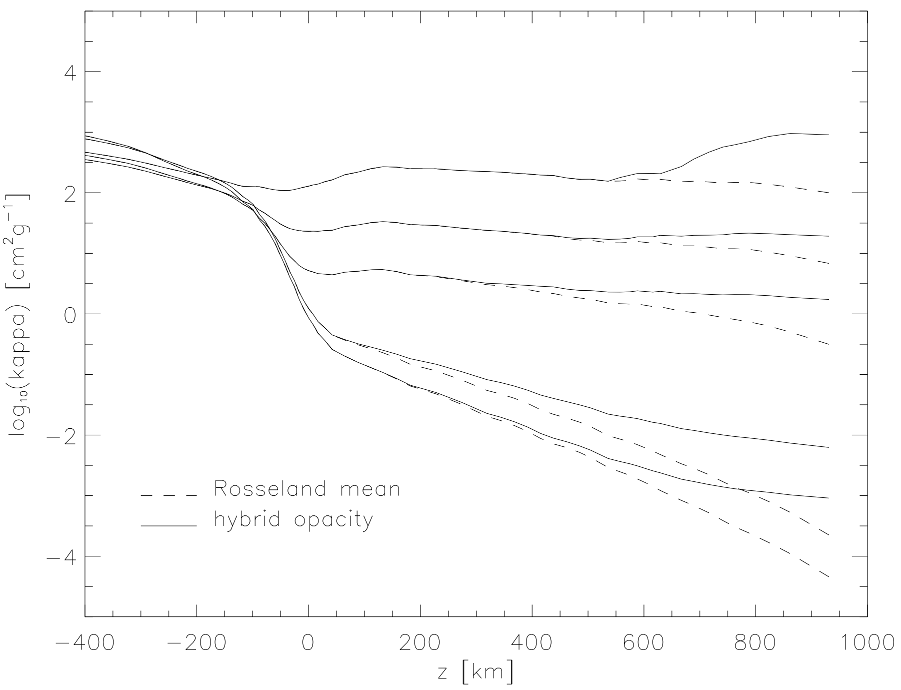

Figure 4.12: *The bin-averaged opacities as a function of height for the 5 bin solution. Both the Rosseland mean and the hybrid opacity defined in Eq. (4.34) are shown. For $z < 0$, the opacity values become similar for all bins, resulting in an effectively grey treatment of the radiative transfer.*

The trend towards an effectively grey radiative transfer in multi-bin models for large optical depths can be seen in Fig. 4.12, which shows the bin opacities as a function of geometrical height for the 5-bin model. As a consequence of τ-sorting, for $z > 0$ each bin is associated with a certain magnitude of the opacity. The height where the Planck mean replaces the Rosseland mean grows with increasing strength of the corresponding bin opacity, the transition being located at $\tau \approx 0.35$ on the optical depth scale of each bin. For $z < 0$, the association of a given bin to opacities of a certain order of magnitude is lost and the opacity values of different bins approach each other. This can be attributed to the fact that, for $\tau > 1$, τ-sorting is no longer a reasonable criterion for sorting frequencies, since the opacities in the optically thick regime do not contribute to the selection process. Consequently, the 5-bin model effectively leads to a grey representation of the opacities in these regions.

Finally, we tested whether an even better approximation around $\tau \approx 1$ can be obtained with the 5-bin model by splitting the lowest (continuum) bin into a low-frequency and a high-frequency part. Fig. 4.13 shows the bin-sorted opacity spectrum at two different heights in the atmosphere. The two continuum windows, located at the ODF index-range of 150-175 (corresponding to $\log\lambda[\text{Å}] \approx 3.49 \sim 3.74$) and 225-270 (corresponding to $\log\lambda[\text{Å}] \approx 4.05 \sim 4.45$) respectively, constitute seperate frequency bins. The two sub-bins have a different dependence on depth, so that a splitting appears to be reasonable. In Fig. 4.14, the depth dependence of the opacity for the two sub-bins and the undivided continuum bin is shown. The opacity of the undivided bin remains quite close to the lower of the two sub-bins over the whole height-range. This can be explained by the fact that, for $z < 0$, the Rosseland mean favours smaller opacities, while for $z > 0$ the Planck function B assumes larger values in the low-frequency bin, which therefore contributes more to the Planck mean. As can be seen in Fig. 4.15, introducing sub-bins improves the approximation of Q_{ODF} compared to the 5-bin solution. The improvement is most significant in the height range $0 - 400$ km; above 400 km the effect is negligible since there both continuum sub-bins are optically thin and do not contribute to the radiative energy exchange. It is however doubtful whether this improvement justifies the additional computational effort.

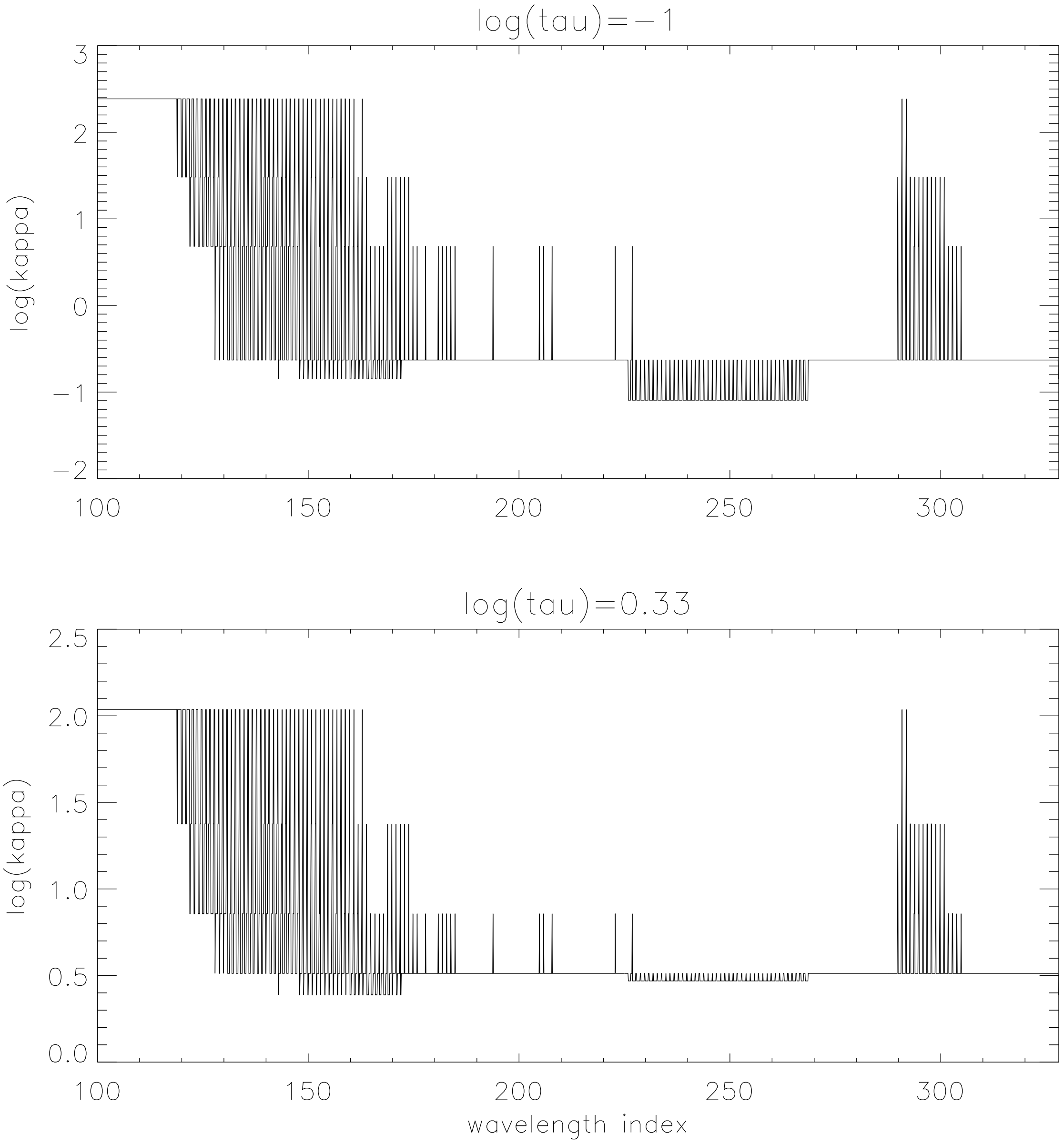

Figure 4.13: *The bin-sorted opacity spectrum at two different heights for the model with split continuum. The heights correspond to optical continuum depths of log(*τ_{5000}*) = -1 and 0.33, respectively. As a result of the sorting and averaging procedure, the opacity values that occur in these spectra form a discrete set. Note the relative change with depth of the two continuum levels in the frequency windows with indices* $150 - 175$ *and* $225 - 270$.

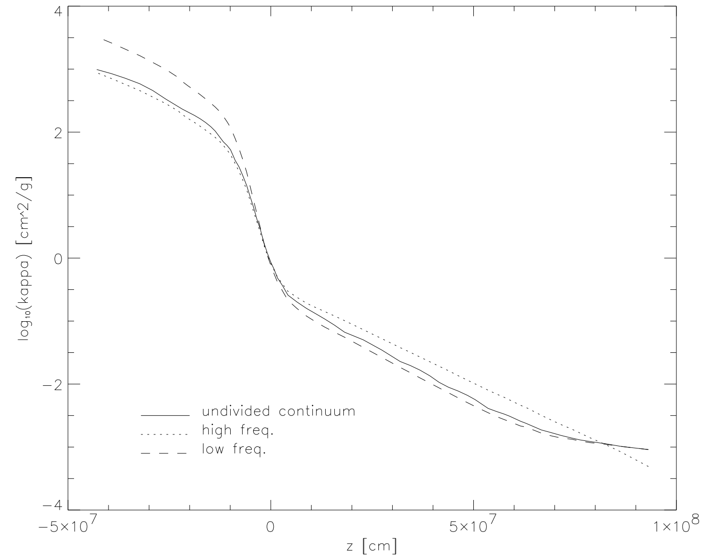

Figure 4.14: *The opacity of the unsplit continuum (solid) and the low- and high-frequency sub-bins (dashed and dotted) as a function of height for a 5-bin model without and with frequency-split continuum bin, respectively. The curve for the unsplit bin closely follows the lower of the two sub-bin curves.*

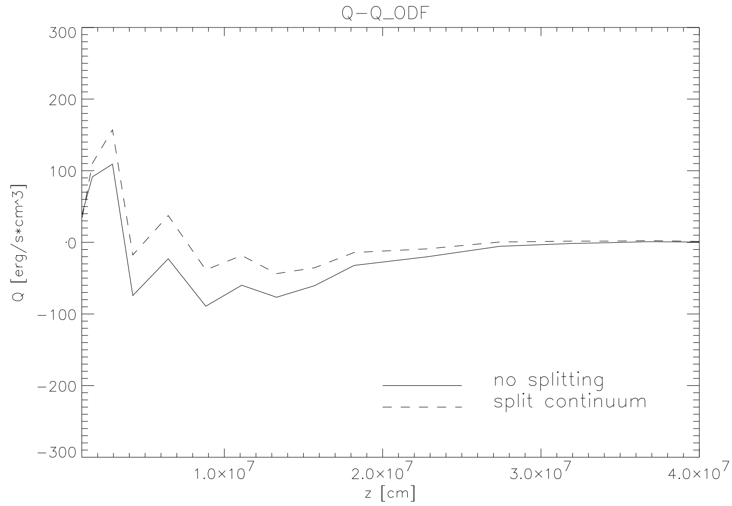

Figure 4.15: $Q - Q_{\mathrm{ODF}}$ *for the 5-bin case with and without continuum-splitting. For* $z > 30$ *km, the solution with splitting yields the better approximation to the ODF reference solution.*

4.3.2 Results of 2D calculations

The previous section has shown that, in a plane-parallel atmosphere, a substantial improvement of the radiative heating rates in comparison to the grey case can be achieved already with a moderate number of frequency bins. In this section, we consider two-dimensional situations in order to assess the error incurred by using a 1D reference atmosphere in the τ-sorting procedure. For calculations with opacity-binning, the same bin parameters as in the previous section have been used.

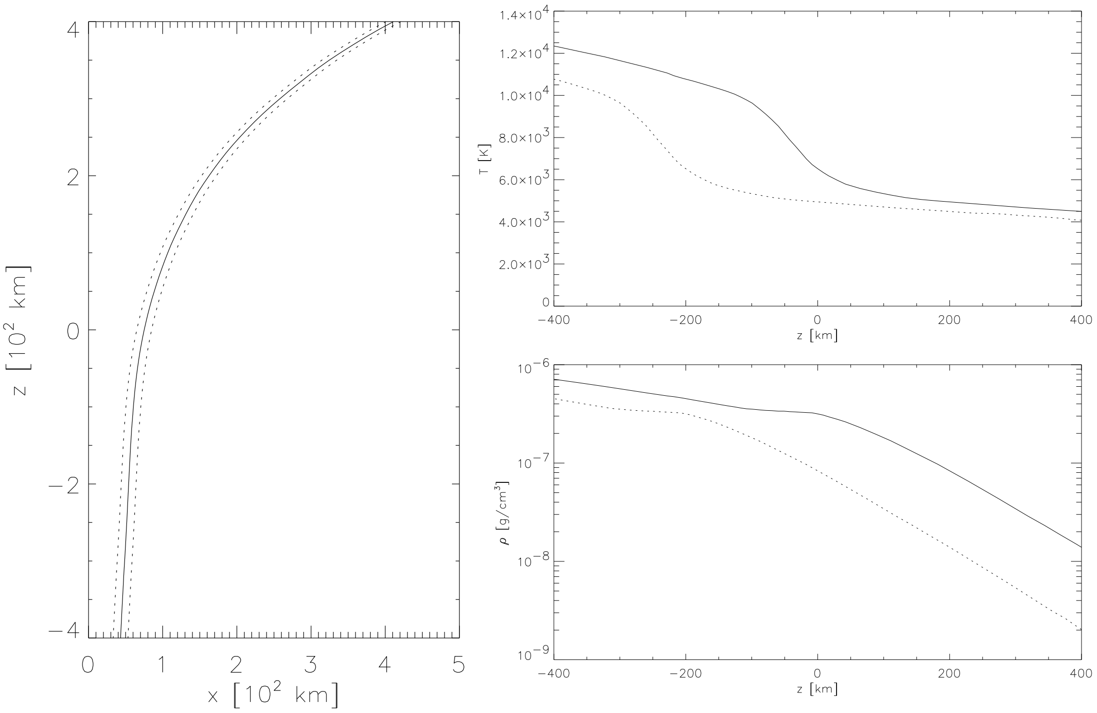

Figure 4.16: *Left panel: The solid line marks the boundary between sheet and surrounding atmosphere; only the right half of the sheet is shown. The dotted lines are shifted by 10 km in the horizontal direction. Right panels: Temperature (top) and density (bottom) as function of height z on the symmetry axis ($x = 0$) of the magnetic sheet (dotted) and in the exterior at $x = 500$ km (solid).*

As a first step we investigated a simple model of a 2D magnetic flux sheet. Based on the 1D atmosphere used in the previous section, the stratification in the interior of the sheet is shifted downwards by 200 km relative to the surrounding atmosphere (the “Wilson depression”; see Fig. 4.16, right panels). The width of the sheet as a function of height results from magnetic flux conservation together with the condition of total (magnetic + gas) pressure equilibrium between the interior and the exterior of the sheet. The equilibrium condition reads

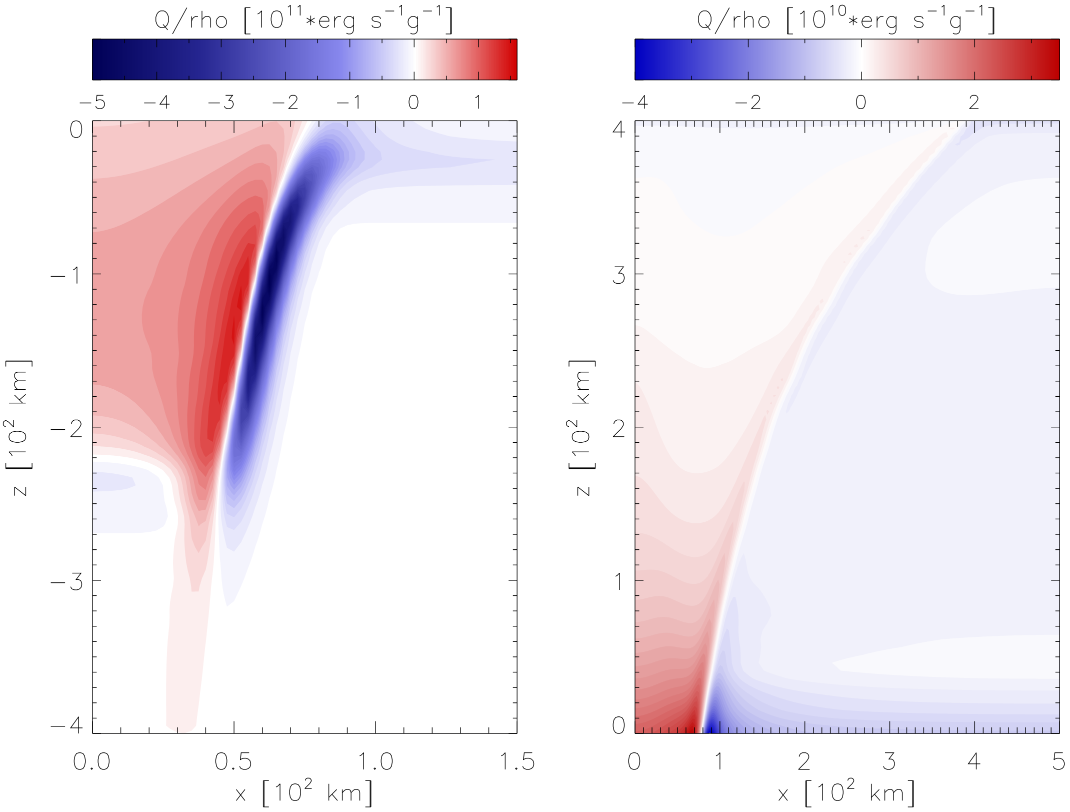

Figure 4.17: *Q_{rad}/ϱ for the ODF based reference solution in a magnetic flux sheet model. The left and right panels show the lower part ($z < 0$) and upper part ($z > 0$) of the sheet, respectively.*

$$\frac{B_{\text{in}}^2(z)}{8\pi} = \Delta p(z) \quad , \tag{4.40}$$

where B_{in} is the field strength in the sheet and $\Delta p = p_{\text{ex}} - p_{\text{in}}$ is the difference between external and internal gas pressure. Substituting $B_{\text{in}}(z)$ from the above equation in the expression for flux conservation

$$B_{\text{in}}(z)w(z) = B_{\text{in}}(0)w(0) \tag{4.41}$$

($w(z)$ is the width of the sheet), one obtains

$$w(z) = \sqrt{\frac{\Delta p(0)}{\Delta p(z)}}\, w(0) \quad . \tag{4.42}$$

At the height $z = 0$, corresponding to $\tau_{5000} = 1$ in the exterior, the flux sheet has a width of 150 km. The sheet is fanning out with increasing height as the magnetic pressure necessary to balance the jump in gas pressure decreases (see Fig. 4.16, left panel). At the interfaces between the interior and the exterior of the sheet, the atmospheric parameters are smoothed out horizontally over a distance of several tens of kilometers:

$$T(x) = T_{\mathrm{in}} + (T_{\mathrm{ex}} - T_{\mathrm{in}}) \cdot \frac{1}{2} \left[\mathrm{ERF} \left(\frac{x - x_{\mathrm{b}}}{\Delta x} \right) - 1 \right] \quad , \tag{4.43}$$

and likewise for pressure and density; x_{b} is the horizontal position of the sheet boundary, for the smearing parameter Δx we used a value of 10 km. Owing to the mirror symmetry of the sheet, the calculations can be restricted to one half of the flux sheet, with symmetrical boundary conditions imposed on the sheet's symmetry axis (located at $x = 0$). A cartesian grid with 201×161 grid points and horizontal and vertical resolutions of, respectively, 2.5 km and 5 km was used.
In Fig. 4.17, the heating rates for the ODF reference solution are shown. For $z > -200$ km, the sheet interior is heated as a result of the lateral radiative energy exchange with the hotter exterior. Correspondingly, the outside regions close to the sheet boundary are subject to strong cooling. The weak cooling, which occurs below $z = -200$ km inside the sheet around the symmetry axis, is caused by radiative energy losses as the interior becomes optically thin at these heights. Fig 4.18 shows Q_{rad} along horizontal cuts through the (half) sheet at three different heights. At $z = -150$ km, the agreement between the ODF reference and both the grey and multi-bin solutions is very good. Corresponding to the horizontal temperature gradient, a heating peak inside the sheet and a stronger cooling region outside form near the sheet boundary. At this height, the outside atmosphere and most of the boundary region are optically thick and the radiative transfer is essentially grey, so that Q_{rad} is well represented even without a detailed treatment of the frequency dependence. The maximum relative errors near the heating and cooling peaks range between 5 and 10 percent.

At $z = 100$ km, both multi-bin solutions qualitatively reproduce the ODF case. The grey (Rosseland) case is much less accurate than the 3- and 5-bin solutions. The heating peak at the boundary is shifted outwards by approximately 10 km, the peak value being reduced by 15 percent with respect to the ODF case, while the small cooling dip outside is not captured at all. The relative errors of the multi-bin solutions are largest at the cooling dip around $x = 120$ km with 30 and 20 percent for the 3- and 5-bin solutions, respectively. At the heating peak ($x = 105$ km) the errors do not exceed 10 percent. At a still greater height of 250 km, both the 3- and 5-bin approximations yield acceptable results, though neither captures the full extent of the cooling peak outside the sheet boundary. Around the heating peak ($x = 200$ km) and in the outside region ($x > 250$ km), the 5-bin solution achieves a clear improvement over the 3-bin case. The error of the grey solution is large by comparison, and the ODF solution is not even approximately reproduced. The heating peak *inside* the sheet has vanished;

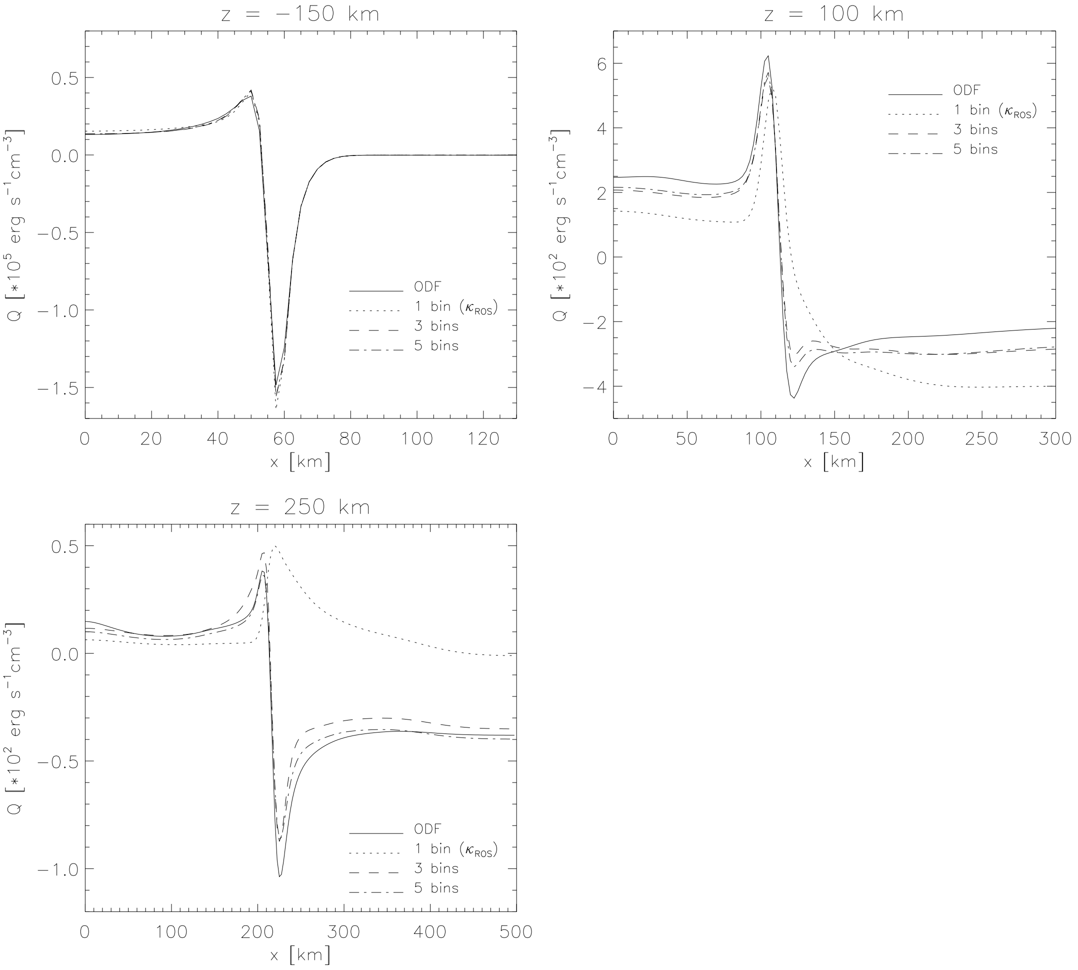

Figure 4.18: *Horizontal profiles of $Q_{\rm rad}$ at three different heights in the 2D atmosphere with an embedded flux sheet. $x = 0$ corresponds to the symmetry axis of the sheet.*

instead, heating takes place immediately *outside* the sheet, where the correct solution shows considerable cooling. This behaviour can be explained by the fact that, on the basis of the Rosseland mean, the interior of the sheet is transparent at a height of 250 km; accordingly, the interaction between gas and radiation is very weak within the sheet, resulting in small values of $Q_{\rm rad}$. In the optically thicker regions immediately outside the sheet, radiation originating from deeper, hotter regions at the *opposite* sheet boundary and crossing the sheet almost unattenuated, leads to a net heating effect. The error of the grey solution far outside the sheet ($x = 500$ km) is in agreement with the results of the 1D calculations at the same height in the atmosphere; this is plausible since far away from the sheet the radiative transfer is essentially one-dimensional. This example clearly demonstrates how important a nongrey approach to radiative transfer can be in

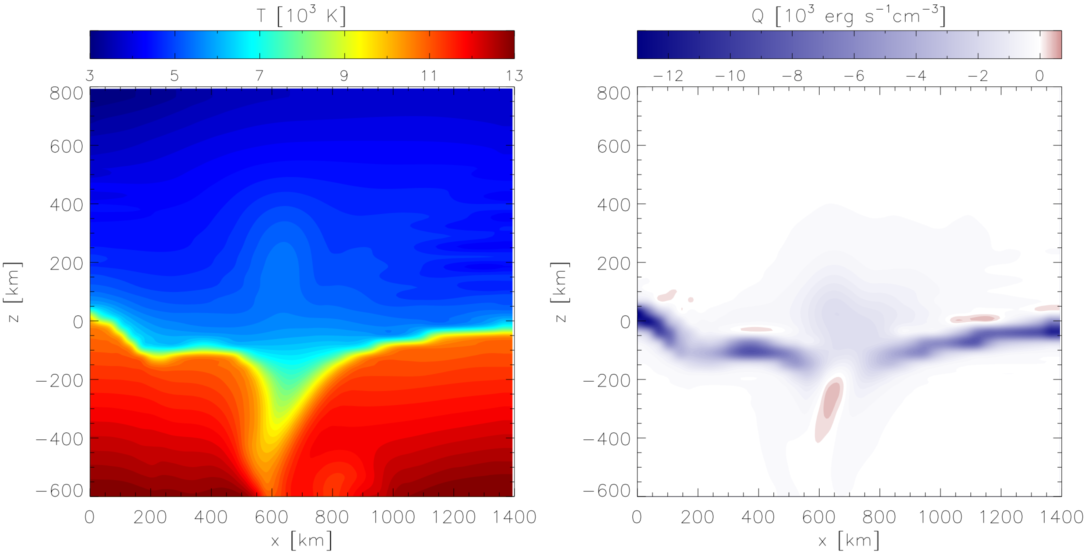

Figure 4.19: *Left: Temperature plot of a* 1.4×1.4 Mm^2 *cut-out from a two-dimensional simulation snapshot (Ploner et al. 1999). Right: The corresponding ODF based radiative heating rate.*

optically thin regions in order to obtain accurate values of $Q_{\rm rad}$.

As a further step towards more realistic situations we tested the opacity binning models in calculations that used a snapshot from a 2D simulation of granulation by Ploner et al. (1999) (Fig. 4.19), which has no relation to the one-dimensional reference atmosphere used for τ-sorting. The vertical and horizontal extent of the computational domain is 1400×1400 km^2 with a grid resolution of 35 km. Fig. 4.20 shows $Q_{\rm rad}$ in horizontal cuts at heights of approximately 100 and 500 km above $\tau_{5000} = 1$, respectively. The same τ-sorted opacity-tables as in the previous calculation have been used. In accordance with the results for the flux sheet, all solutions (including the grey case) agree quite well with each other at the lower level, although the errors of the grey case become more pronounced towards the horizontal boundaries of the domain. The differences between the 3- and 5- bin solutions are only marginal. At 500 km above $\tau_{5000} = 1$, the Rosseland solution, similar to the optically thin case in Fig. 4.18, completely fails to reproduce the ODF reference solution. On the other hand, the 5-bin solution excellently agrees with the reference curve and is clearly superior to the 3-bin model.

In summary, the τ-sorted 5-bin model apparently yields good approximations of $Q_{\rm rad}$ to the quasi-exact ODF case over a large height range in 'realistic' 2D atmospheres. The advantage over a grey radiative transfer based on the Rosseland mean is most pronounced at large photospheric heights where spectral lines are the dominant opacity sources.

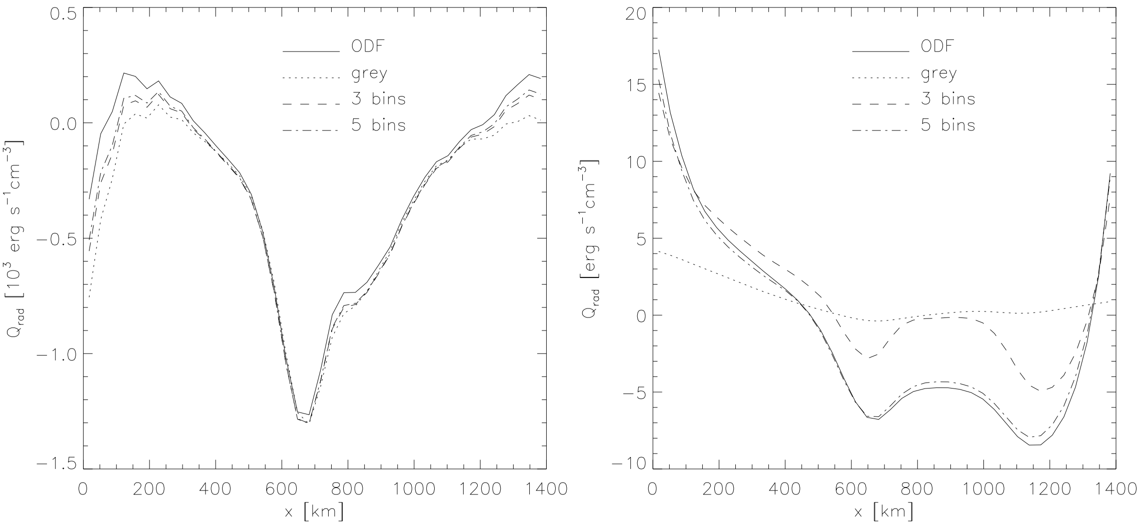

Figure 4.20: *Horizontal profiles of* Q_{rad} *for a snapshot from a 2D simulation, at heights of* 100 *km (left) and* 500 *km (right) above* $\tau_{5000} = 1$.

4.3.3 The opacity binning method in the limit of a large number of bins

While the 5-bin τ-sorting scheme shows acceptable results for computing radiative heating rates in both 1D and 2D, one might ask whether any further improvement can be achieved by increasing the number of frequency bins. Full (M)HD simulations with more than a handful of bins are not feasible with the computing power available today, but with increasing computational resources, this question may become relevant in the future. In this section we study the performance of τ-sorting and also κ-sorting in multi-bin models with increasing numbers of bins.

We first applied the τ-sorting procedure to a high-resolution 1D atmosphere with $\Delta z = 0.5$ km, which was interpolated from the reference stratification used in the previous sections. Fig. 4.21 shows $(Q - Q_{\text{ODF}})/\varrho c_V T$, i.e. the error in Q divided by the internal energy density of the gas, which gives the rate by which the internal energy is modified by the error in Q. The 5-bin solution uses the parameters specified above, while for larger numbers of bins the optical depth-levels separating the bins are spread evenly on the $\log \tau_{5000}$-scale across the upper part of the atmosphere, $\tau_{5000} < 1$. The 5-bin solution gives the best result for $z \approx 200$ km $-$ 600 km, while the error increases for greater heights. For increasing numbers of bins, the solutions seem to converge towards a limiting solution, which, however, clearly deviates from Q_{ODF}. This does not come as a surprise as the multi-bin approach, on theoretical grounds, can not be expected to reproduce the exact solution, even in the limit of infinitely large bin numbers (see the remark at the end of sec. 4.2.2). In Fig. 4.22, the error rate is plotted for

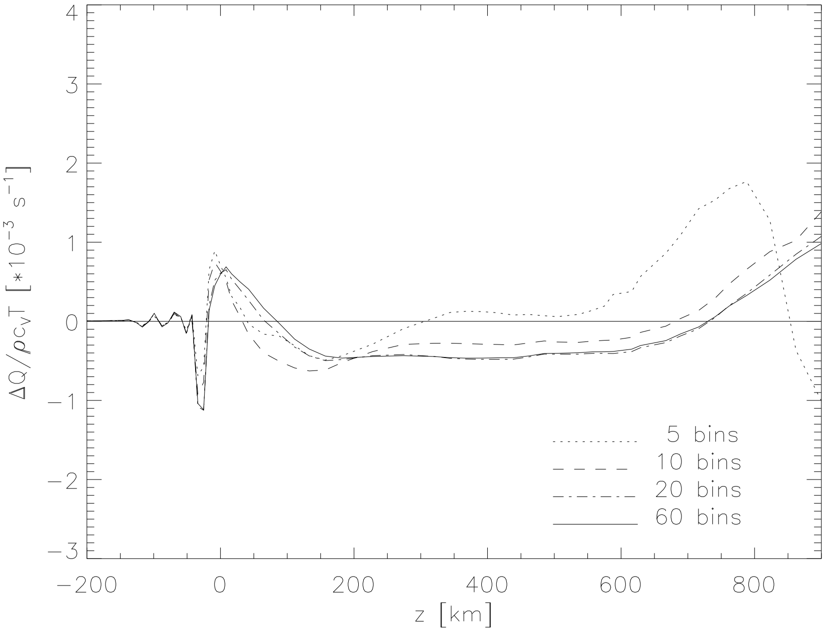

Figure 4.21: *Rate of change of the internal energy due deviations of Q from the ODF reference solution as a function of height. Shown are results for τ-sorted models with different numbers of bins.*

κ-sorted bins. As the reference optical depth (on the τ_{5000}-scale), for the opacity spectrum $\kappa_\nu(\tau_{\rm ref})$ on which sorting is based, we chose $\tau_{\rm ref} = 0.1$ (Ludwig 1992). In heights above 200 km, the 5-bin solution is clearly worse than the corresponding result for the 5-bin τ-sorted model. For larger numbers of bins, a pronounced advantage of the τ-sorted solutions is found only above 700 km.
A different picture is obtained when using $\tau_{\rm ref} = 0.01$ (Fig. 4.23). Here, for heights below 600 km the approximation is better than in the τ-sorted case. Again, as for τ-sorting, the 5-bin solution gives the best overall result.

All results shown so far, the τ-sorted model as well as the two κ-sorted ones, show a clear trend towards too strong heating in the uppermost regions ($z \gtrsim 700$ km). This behaviour is caused by using the Planck mean in the optically thin regime. In the regions $z \gtrsim 700$ km we have $J_\nu > B_\nu$ for a large part of the spectrum, since for the optically thin frequencies J_ν is determined by radiation coming from deeper and hotter regions around $\tau_\nu = 1$ (see Fig. 4.24 for an example). Consequently, $Q_{\rm rad} \propto \int \kappa_\nu \varrho \, (J_\nu - B_\nu) \, d\nu > 0$, i.e. some heating results from the absorption of the "hot" radiation. As the Planck mean tends to overestimate the line opacities, the factor $\kappa_{\rm bin}\varrho$ in the expression for $Q_{\rm rad}$ in opacity binning models becomes too large and the heating in the optically thin regions is overestimated. We have seen that this effect is more pronounced for the κ-sorted models. This

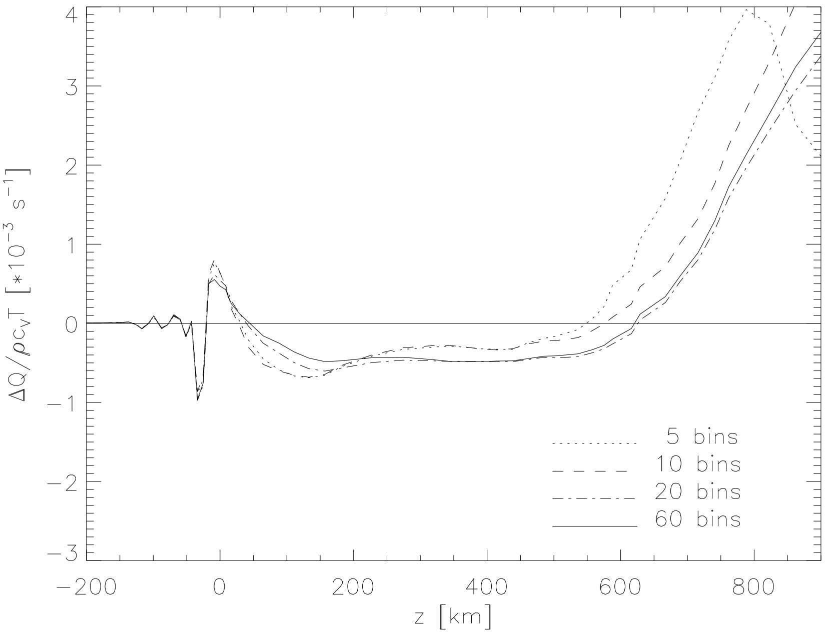

Figure 4.22: *Same as Fig. 4.21, but for κ-sorting with a sorting parameter of* $\tau_{\rm ref} = 0.1$.

may be explained by the fact that κ-sorting does not properly account for the line opacities above $\tau_{\rm ref}$. As a consequence, in regions above $\tau_{\rm ref}$, opacities of considerably varying magnitude may be collected in a given bin, resulting in a bad representation of opacities. This is not the case when τ-sorting is used, since here the integral $\int_0^{z(\tau=1)} \kappa_\nu \varrho \, dz$ contributes to the sorting process. Thus, a systematic advantage of τ-sorting over κ-sorting is found only for heights above 700 km. The quality of the 5-bin solution, both for τ-sorting and for κ-sorting, depends on the particular choice of the bin levels, so the results shown in Figs. 4.21 and 4.23 do not necessarily imply that a small number of bins always yields the best approximation.

As the systematic overestimation of the heating in the uppermost parts of the atmosphere is caused by the Planck mean, it might be worthwhile to look for a possible replacement which performs better in the optically thin regime. As already mentioned in Sec. 4.2.2, the derivation of the Planck mean is based on the assumption $J_\nu \approx B_\nu/2$ (implying $J_\nu - B_\nu \approx -B_\nu/2$), which is strictly correct only for the optically thin parts of an isothermal atmosphere (the factor 1/2 accounting for the fact that the uppermost parts of the atmosphere are only illuminated from the hemisphere underneath). However, upon inspection of Fig.4.24, which shows J_ν and B_ν for the ODF-calculation at the top of the reference atmosphere, it

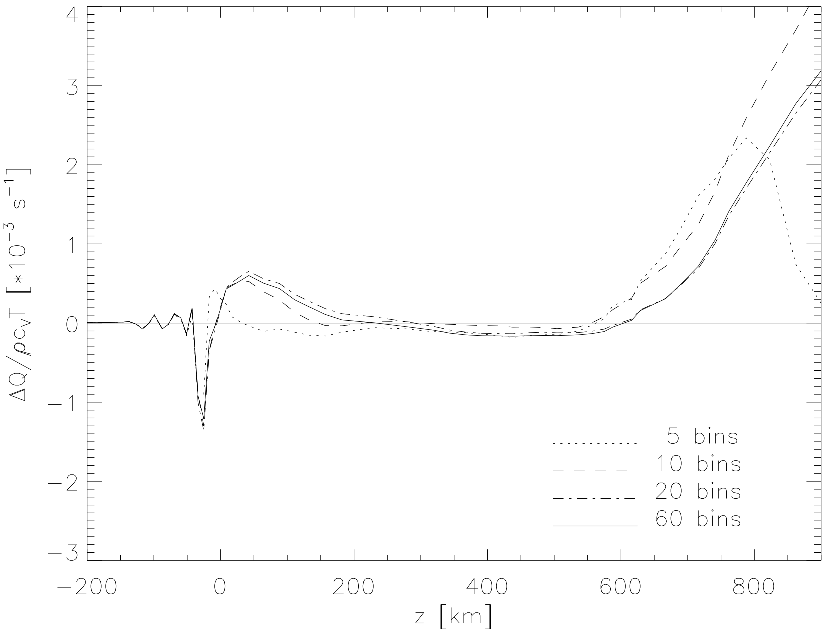

Figure 4.23: *Same as Fig. 4.22, for* $\tau_{\mathrm{ref}} = 0.01$

becomes immediately clear that this relation does not even approximately hold at great heights in the atmosphere.

In order to derive an alternative prescription for a bin average at small optical depths, we set out from Eq. (4.29) which gives the general definition of a bin-averaged opacity. Instead of replacing the weighting function $J_\nu - B_\nu$ with B_ν, one might try to obtain $J_\nu - B_\nu$ by using the *exact* radiation field $J_{\nu,\mathrm{ODF}}$ at the top of the atmosphere at $\tau = 0$, which results from an ODF reference calculation (plotted in Fig. 4.24). Two problems immediately arise:

(i) The opacity tables that result from the opacity binning approach must be applicable to atmospheres differing from the reference stratification. The intensity spectrum $J_{\nu,\mathrm{ODF}}(\tau = 0)$ may be correct for the optically thin regions of the reference atmosphere, but there is no guarantee that it is a good approximation in the higher regions of other atmospheres. On the other hand, the τ-sorting approach requires a reference atmosphere anyway, and there is no reason why the properties of this particular atmosphere should affect only the frequency-sorting procedure.

(ii) The weighting function $J_{\nu,\mathrm{ODF}} - B_\nu$ is not positive definite. Therefore, straightforward application of the averaging procedure may lead to negative mean opacities.

Dividing the frequency bin into those frequencies with $J_\nu - B_\nu \geq 0$ and those with $J_\nu - B_\nu < 0$, one obtains

$$Q_{\rm bin}/4\pi\varrho = \int_+ \kappa_\nu (J_\nu - B_\nu) d\nu + \int_- \kappa_\nu (J_\nu - B_\nu) d\nu \tag{4.44}$$

$$= \kappa^+ \int_+ (J_\nu - B_\nu) d\nu + \kappa^- \int_- (J_\nu - B_\nu) d\nu \tag{4.45}$$

with the positive-definite averages

$$\kappa^+ = \frac{\int_+ \kappa_\nu (J_\nu - B_\nu) d\nu}{\int_+ (J_\nu - B_\nu) d\nu} \tag{4.46}$$

and

$$\kappa^- = \frac{\int_- \kappa_\nu (J_\nu - B_\nu) d\nu}{\int_- (J_\nu - B_\nu) d\nu} \quad . \tag{4.47}$$

If κ^+ and κ^- are of the same magnitude, we may define

$$\overline{\kappa} = \frac{1}{2}(\kappa^+ + \kappa^-) \tag{4.48}$$

in cases, where straightforward use of $J_{\nu,{\rm ODF}} - B_\nu$ as the weighting function leads to negative results, since then

$$Q_{\rm bin}/4\pi\varrho \approx \frac{1}{2}(\kappa^+ + \kappa^-) \int_{\rm bin} (J_\nu - B_\nu) d\nu \tag{4.49}$$

and the heating rate is, approximately at least, recovered.

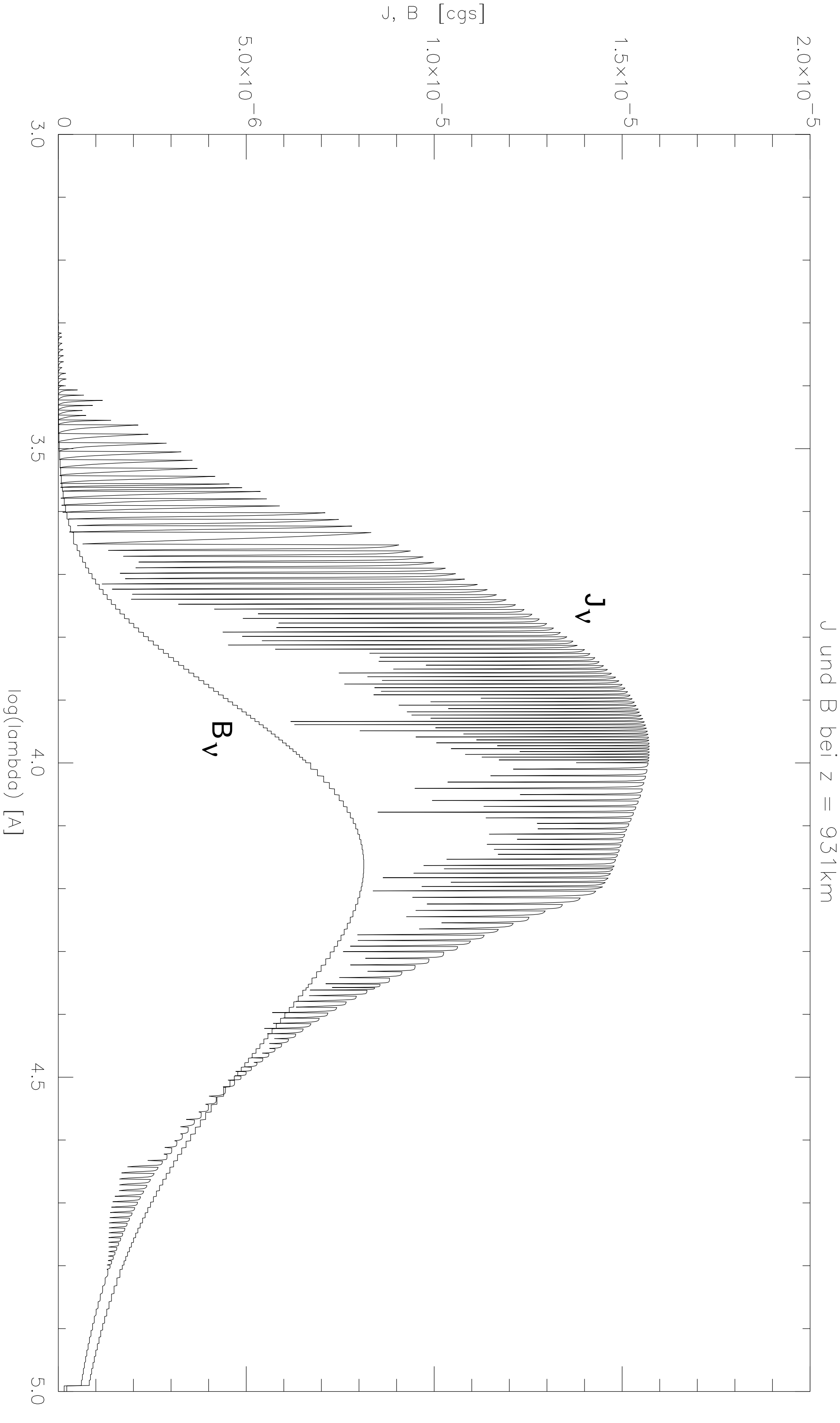

Figure 4.24: *J_ν from an ODF-calculation and B_ν (lower curve) at the top (z=931 km) of the reference atmosphere. At this height the atmosphere has a temperature of 3500 K.*

Fig. 4.25 shows the results of test calculations with the averaging procedure using $J_{\nu,\mathrm{ODF}}(\tau = 0) - B_\nu$ as weighting function. A transition depth $\tau_0 = 0.1$, below which the Rosseland mean is used, has been chosen. τ-sorting has been applied, collecting those frequencies in the same bin which reach $\tau_\nu = 0.5$ at the same height level. Whenever a negative opacity-value occured, it has been replaced by expression (4.48).

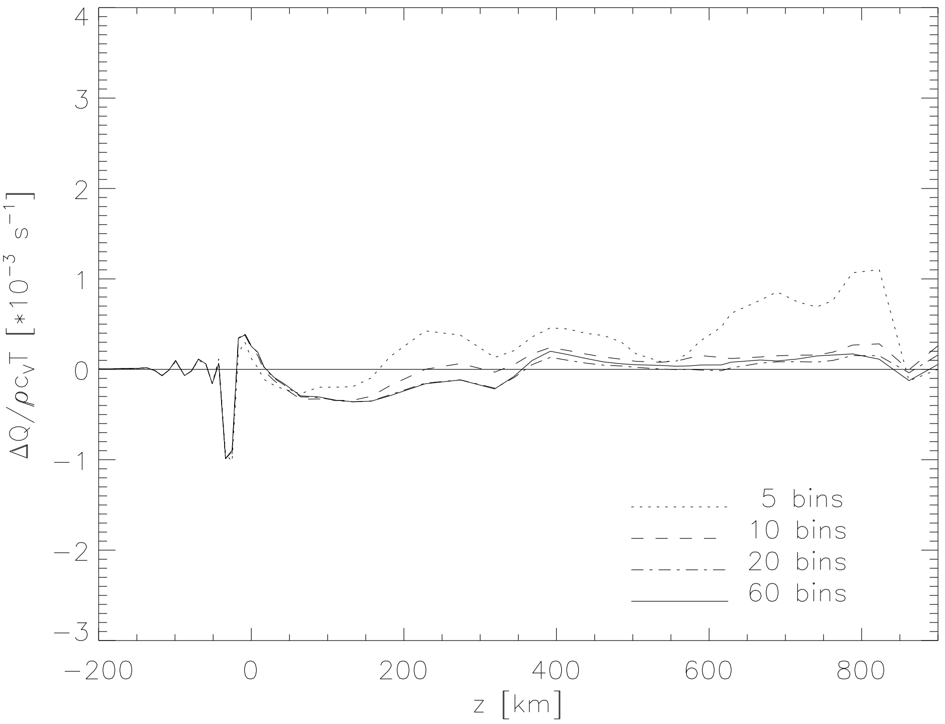

Figure 4.25: *Same as Fig.4.21, for a τ-sorted model where the Planck mean has been replaced in optically thin regions by the $J - B$ mean described in the text.*

The results shown in Fig. 4.25 indicate that the new averaging appears to work well for calculations with 10 or more bins. Here the agreement with the ODF-solution is excellent throughout the whole height range, including the regions $z > 700$ km. The quality of the 5-bin solution, however, is not that impressive, and while the accuracy of the 5-bin approximation depends rather sensitively on the particular values of the bin levels, we could not achieve a significant improvement with different choices of the bin levels. The advantage of the new method in optically thin regions is still observable in atmospheres which differ strongly from the reference atmosphere. Fig. 4.26 shows a horizontal cut at a height of approx. 700 km above $\tau_{5000} = 1$ through the 2D simulation snapshot that was used in Sec. 4.3.2. The solution obtained by using the $J - B$ mean is clearly closer to the reference solution for $x > 400$ km than the κ-sorted 5-bin solution using the Planck-mean.

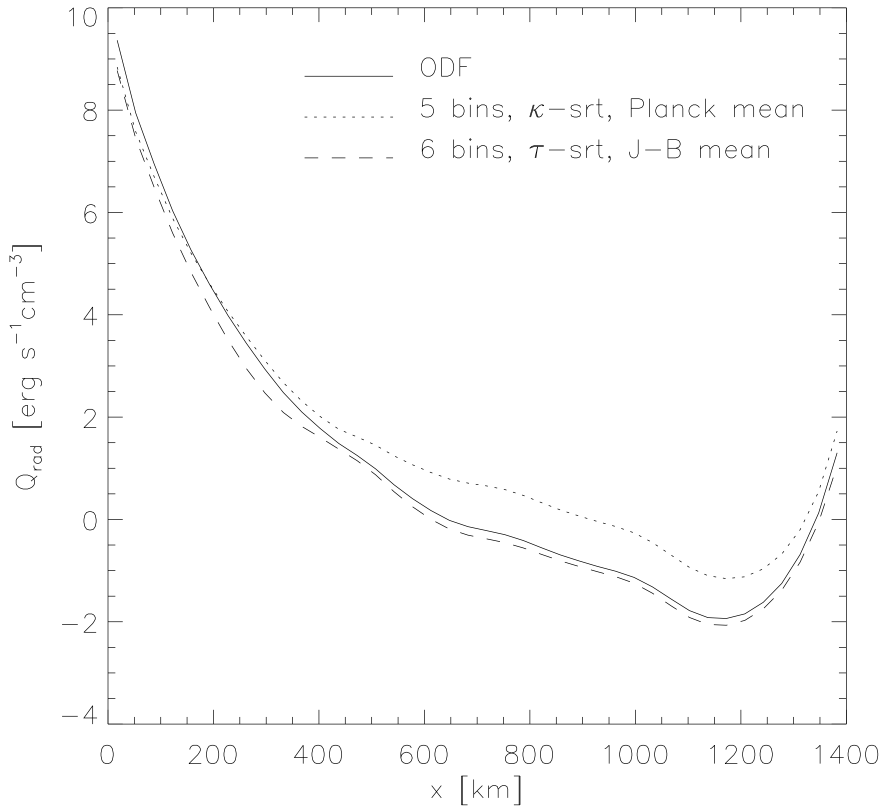

Figure 4.26: *Q_{rad} for a horizontal cut through a 2D snapshot at a height of approx. 700 km above $\tau_{5000} = 1$. For $x > 400$ km the $J - B$ mean improves the quality of the approximation.*

In principle, the new opacity averaging procedure seems to be superior to the use of the Planck-mean when a sufficiently large number of bins is used. This is particularly true for simulations which are extended to include chromospheric layers, since at these heights the advantage is most pronounced.[7] Since 2D/3D simulations are presently restricted to multi-bin calculations with 4 or 5 bins at best, the merits of the new averaging procedure appear to be rather academic. The improvement due to the modified average may, however, become relevant in the future, when the increase of computing power makes simulations with a larger number of bins feasible.

---

[7] In the chromosphere, the error incurred by the assumption of LTE might, however, outweigh this effect.

4.3.4 Error timescales

Having compared the accuracy of different opacity binning models, it is worthwhile to obtain an estimate of the importance of the errors which result from the various approaches. In the light of the results discussed in the previous sections, two questions seem to be of particular interest:

(i) Does the error of the grey solution make a nongrey treatment mandatory?

(ii) How severe is the systematic error at large heights ($z > 600$ km) introduced by the Planck mean?

As an indicator for the severity of the error we use the time scales on which the deviation from the reference Q_{ODF} affects the temperature structure of the atmosphere. In order to assess how important the error is, it is plausible to compare these scales with typical dynamical time scales in the photosphere, which give an estimate for the time span over which a volume element of the flowing plasma is exposed to the inaccuracies of Q_{rad} in a simulation with grey or mutlibin radiative transfer.

In order to isolate the effect of the error in Q, we assumed that the 1D reference atmosphere is kept in radiative equilibrium by a time-independent source term Q_s that represents the necessary non-radiative heating or cooling, i.e.

$$Q_{\mathrm{ODF}}(z) + Q_{\mathrm{s}}(z) \equiv 0. \tag{4.50}$$

Any heating or cooling is then solely caused by the error $\Delta Q = Q_{\mathrm{app}} - Q_{\mathrm{ODF}}$ introduced by the approximative treatment of the frequency dependence. Starting with the unperturbed temperature stratification $T_0(z)$ for $t = 0$, the time development of the temperature is assumed to be given by

$$\frac{\partial T}{\partial t}(z,t) = \frac{\Delta Q(z,t)}{c_V \varrho} \tag{4.51}$$

with $\Delta Q(z,t) = Q_{\mathrm{app}}(z,t) - Q_{ODF}(z, t = 0)$, allowing the temperature to relax to a new equilibrium $T_{\mathrm{eq}}(z)$ for which

$$\Delta Q(z)|_{\mathrm{eq}} = Q_{\mathrm{app}}(z)|_{\mathrm{eq}} - Q_{\mathrm{ODF}}(z, t = 0) \equiv 0 \tag{4.52}$$

or

$$Q_{\mathrm{app}}(z)|_{\mathrm{eq}} + Q_{\mathrm{s}}(z) \equiv 0. \tag{4.53}$$

holds.

Eq. 4.51 was solved by explicit forward integration in time. When computing $Q_{\mathrm{app}}(z,t)$ for each timestep, the changes of $p(z)$ and $\varrho(z)$ required by the condition of hydrostatic equilibrium have been neglected, so our calculation can be expected to give reasonable results only as long as the relative change in temperature remains small. Fig. 4.27 shows the time development of the temperature stratification for the Rosseland approximation (top), the 5-bin τ-sorted model used in Secs. 4.3.1 and 4.3.2 (middle), and a 20-bin τ-sorted model for which the Planck mean has been replaced by the $J - B$ mean described in the previous section (bottom). In the grey case, a strong cooling occurs below $z = 0$, which extends to deeper layers with increasing time. An even more drastic change in temperature occurs above 500 km, where the temperature drop exceeds 10^3 K after a few minutes. However, here the temperature runs out of the range, for which the violation of hydrostatic equilibrium is tolerable.

Using the photospheric pressure scale height of about 150 km as characteristic length scale and assuming typical flow velocities of $1 - 2$ km s^{-1}, one obtains a dynamical time scale of the order of 10^2 seconds. So, the Rosseland mean produces temperature disturbances of several hundred K on time scales that are comparable to typical dynamical time scales. Therefore, one expects these disturbances to have a significant effect on the temperature structure.

For the 5-bin case (middle panel), the situation is entirely different. Above $z = 0$ the temperature stratification settles to a new equilibrium within 30 s. The deviation of about 60 K from the initial state however is much smaller than in the grey case and should not have serious consequences for the physics in the atmosphere. For $z < 0$, the reaction of the atmosphere is much slower, owing to the diffusive character of radiative transfer in the optically thick regime. New equilibrium values for the temperatures have not been reached after $4 \cdot 10^3$ s simulated time and the changes in temperature that can be achieved on dynamical timescales are negligible.

The lower panel of Fig. 4.27 shows that replacing the Planck mean with the $J-B$ averaging procedure further reduces the temperature disturbance for $z > 0$, but considering the results for the 5-bin model, the Planck mean still seems to be an acceptable choice. Below $z = 0$ the impact on the temperature is stronger but remains smaller than 100 K within a time of 10^2 s.

These results of course can only serve as a rough guideline, since it is difficult to predict their relevance in multidimensional moving atmospheres. Nevertheless, they indicate that the error in Q_{rad} of a 5-bin model should have much less severe consequences for the atmospheric dynamics than that of a grey approximation, making a multi-bin approach to the radiative transfer problem appear very favorable.

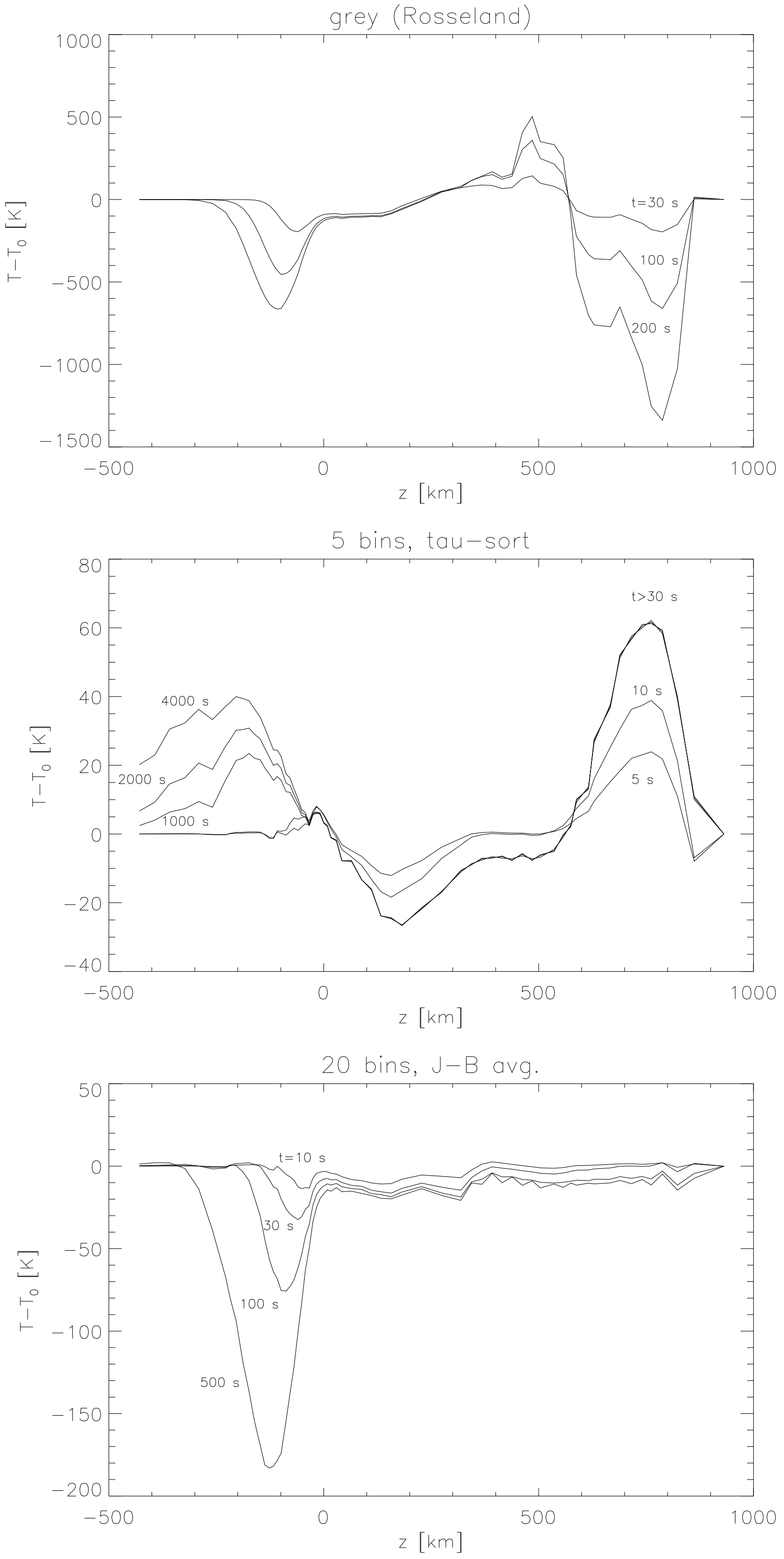

Figure 4.27: *Change in temperature for different times after the calculations started. The three panels refer to three different opacity binning models described in the text. Note the different ordinate scales for each panel.*

Chapter 5

Results of simulation runs

In this chapter, some results of the first full simulation runs carried out with the newly developed code are shown. The simulations are part of a parameter study to investigate the properties of photospheric magneto-convection and their dependence on the average magnetic field strength. Aspects which are of interest include the spatial redistribution of magnetic flux and the formation of intermittent magnetic structures, the interference of magnetic field with convective energy transport and its influence on the emergent intesity distribution as well as the dynamics related to the excitation of waves. Realistic simulations of the kind presented here also allow for a direct comparison with observations, and it is possible to use the simulation results as a basis for spectral line and polarization diagnostics. Such an analysis is, however, beyond the scope of this PhD project.

The basis for the results presented here are three simulation runs with average field strengths of 200 G, 50 G, and 10 G, corresponding to a strong solar plage region, a weak plage region, and a quiet Sun region, respectively. Except for the strength of the initial magnetic magnetic field, B_0, all simulations have the same geometrical setup and were run with the same set of parameters. The dimensions of the computational domain are 1400 km in the vertical direction and 6000 km in both horizontal directions, with a resolution of $100\times288\times288$ grid points. For the shock-resolving diffusivity a scaling factor $c_{\mathrm{shk}} = 1$ was used. The corresponding factor for the hyperdiffusivities was set to $c_{\mathrm{hyp}} = 0.03$. In order to stabilize the flow in the uppermost parts of the computational domain, c_{hyp} was increased in a layer of 200 km thickness immediately below the top of the box and reaches a maximum value of 0.2 on the upper boundary. For the magnetic diffusivity the constant value $\eta = 1.1\cdot10^{11}$ cm^2 s^{-1} was used. This choice of values for c_{shk}, c_{hyp}, and η is motivated by test runs which showed that this set of parameters keeps the solution stable and well resolved without overresolving it.

The simulations were started as purely hydrodynamical convection ($\mathbf{B}\equiv\mathbf{0}$) with a plane-parallel solar model-atmosphere (Spruit 1974), extending from 800 km below to 600 km above the level of continuum optical depth unity at 5000 Å, as initial condition. In the initial phase, a closed lower boundary condition was

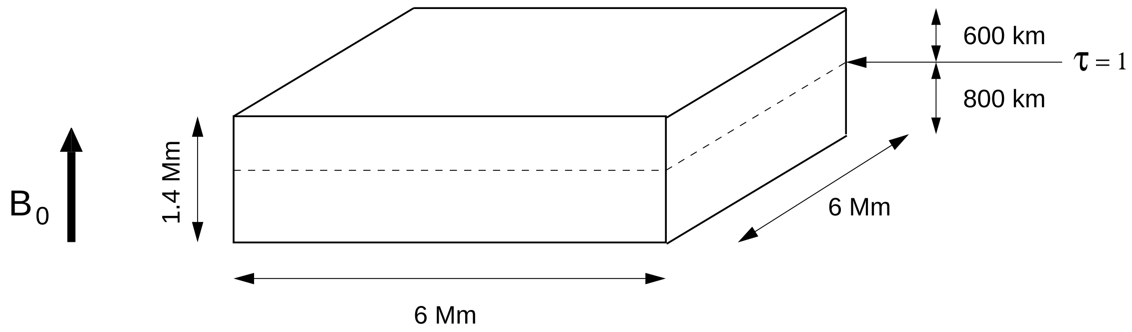

Figure 5.1: *Geometrical setup of the simulation runs. The vector* $\mathbf{B}_0$ *indicates the vertical homogeneous magnetic field introduced into the hydrodynamic convection at the beginning of the magnetic phase.*

used. As soon as the onset of convection had led to sufficiently large vertical velocities near the bottom of the box to allow for the control of mass flux to work efficiently, the lower boundary was opened. After the convection had fully developed and reached a statistically steady state (about one hour solar time after the start of the simulation), a homogeneous vertical initial magnetic field of field strength B_0 was introduced.

All simulations include non-grey radiative transfer in form of a four-bin τ-sorted opacity binning model using the hybrid opacities defined in Eq. (4.34). As already mentioned in Sec. 4.3.1, the minimum number of frequency bins required for a satisfactory modelling of the non-grey radiative transfer and the optimal values for the bin-levels depend on the particular choice of the atmosphere as well as on the vertical extent of the region above $\tau_{5000} = 1$ to be covered. Test calculations based on the initial plane-parallel atmosphere of the simulations suggested that a good approximation over the whole height range is obtained by using four bins with the bin levels on the $\log \tau_{5000}$ scale given by -0.5, -1.5, and -2.5.

In Sec. 5.1 the properties of the “Plage”-run with $B_0 = 200$ G are discussed. Special emphasis is placed on morphology, time development, and on the influence of magnetic fields on the emergent intensity. Sec. 5.2 briefly describes the simulations with $B_0 = 10$ G and 50 G. In Sec. 5.3 we discuss some consequences of the non-grey radiative transfer for the simulation results.

5.1 “Plage” run with $B_0 = 200$ G

5.1.1 Morphology and statistical properties

In this subsection the time evolution and the morphology of the simulation with a horizontally averaged vertical field of 200 G are described and some statistical properties are discussed.

Within a few minutes (approximately one turnover time of the convection) after the magnetic field has been introduced, the convective motions transport most of the magnetic flux into the intergranular downflow regions. During this initial phase the magnetic field forms a network structure with maximum field strengths around 2000 G a height of $z = 0$.[1] The time series shown in Fig. 5.2, which covers the first three minutes of the magnetic phase, illustrates this process of flux expulsion and field concentration. The magnetic network is organized on a “mesoscale”, which typically comprises 4-6 granules. As the simulation develops in time, this mesoscale-network turns out to be long-lived with a typical timescale of hours in contrast to the granule lifetime of approximately 10 min. The occurence of a mesoscale structure, the origin of which is not yet fully understood, is a common and robust feature of many convection simulations. It is observed in both idealized and realistic cases and seems to be largely unaffected by the details of such simulations (see e.g. Cattaneo et al. 2001). A comparison of the mesoscale structures in our simulations with observational indications for meso-granulation is, however, problematic since the horizontal extent of the computational domain is not significantly larger than the mesoscale.

Fig. 5.3 shows a map of the frequency-integrated emergent intensity (brightness) together with horizontal slices of temperature, vertical magnetic field, and vertical velocity at $z = 0$ for a snapshot taken after about two hours of simulated solar time after the start of the magnetic phase. The magnetic field forms elongated, sheet-like structures that extend along intergranular lanes as well as larger structures, comparable to small pores (“micropores”) on the sun, which are located at vertices where several downflow lanes merge and reach a size of up to 1000 km. The micropores appear dark in the intensity picture, while smaller structures are usually brighter than the non-magnetic downflow lanes, their brightness occasionally exceeding the brightness of granules. A large part of the simulated area shows “abnormal” granulation (Dunn & Zirker 1973) with reduced granule sizes compared to the “normal” granules in the upper right corner of the intensity map. The small pores are far from homogeneous; they show considerable small scale intensity fluctuations which are related to localized upflows in regions of reduced field strength. While the overall shape of the magnetic mesoscale network is stable, the magnetic features show a strong time dependence on small scales as magnetic flux is incessantly redistributed within the network. Consequently, the typical lifetime of the micropores is smaller than the timescale associated to the mesogranular length-scale and is comparable to the granule lifetime. The magnetic network itself is embedded in the network of granular downflows.

---

[1] While $z = 0$ corresponds to the $\tau_{5000} = 1$ level of the plane-parallel atmosphere used as initial condition for the simulation, the average $\tau_{5000} = 1$ level of the fully developed convection in its statistically steady state is shifted upwards by approximately 80-100 km. This effect is typical for HD/MHD simulations of convection and is a result of the turbulent pressure of the convective flows (see e.g. Stein & Nordlund 1998).

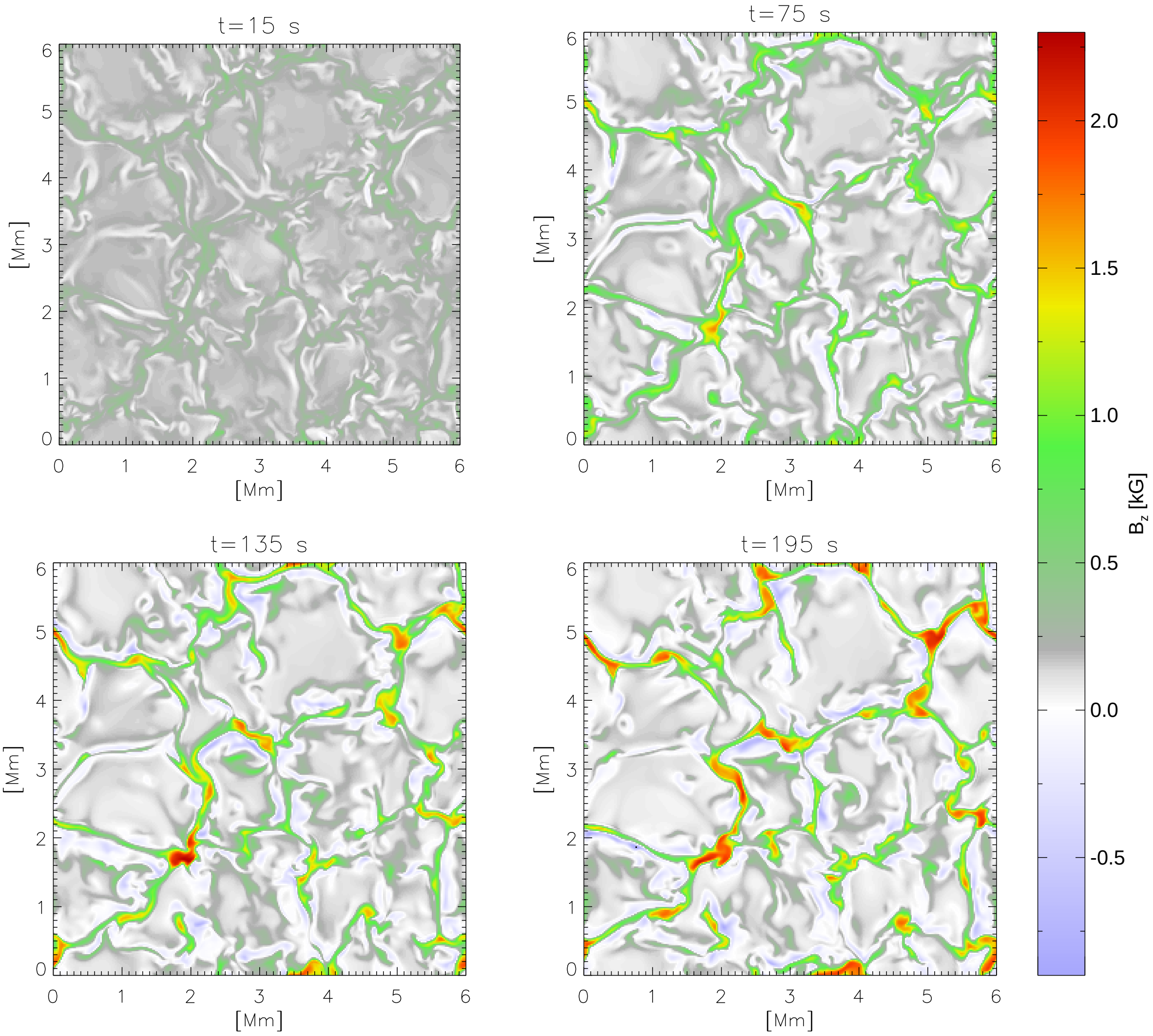

Figure 5.2: *Time series of the vertical magnetic field at $z = 0$, covering the first three minutes of the magnetic phase. After roughly one turnover time the magnetic flux is swept into the downflow regions and forms a slowly evolving "mesoscale" network of concentrated magnetic structures.*

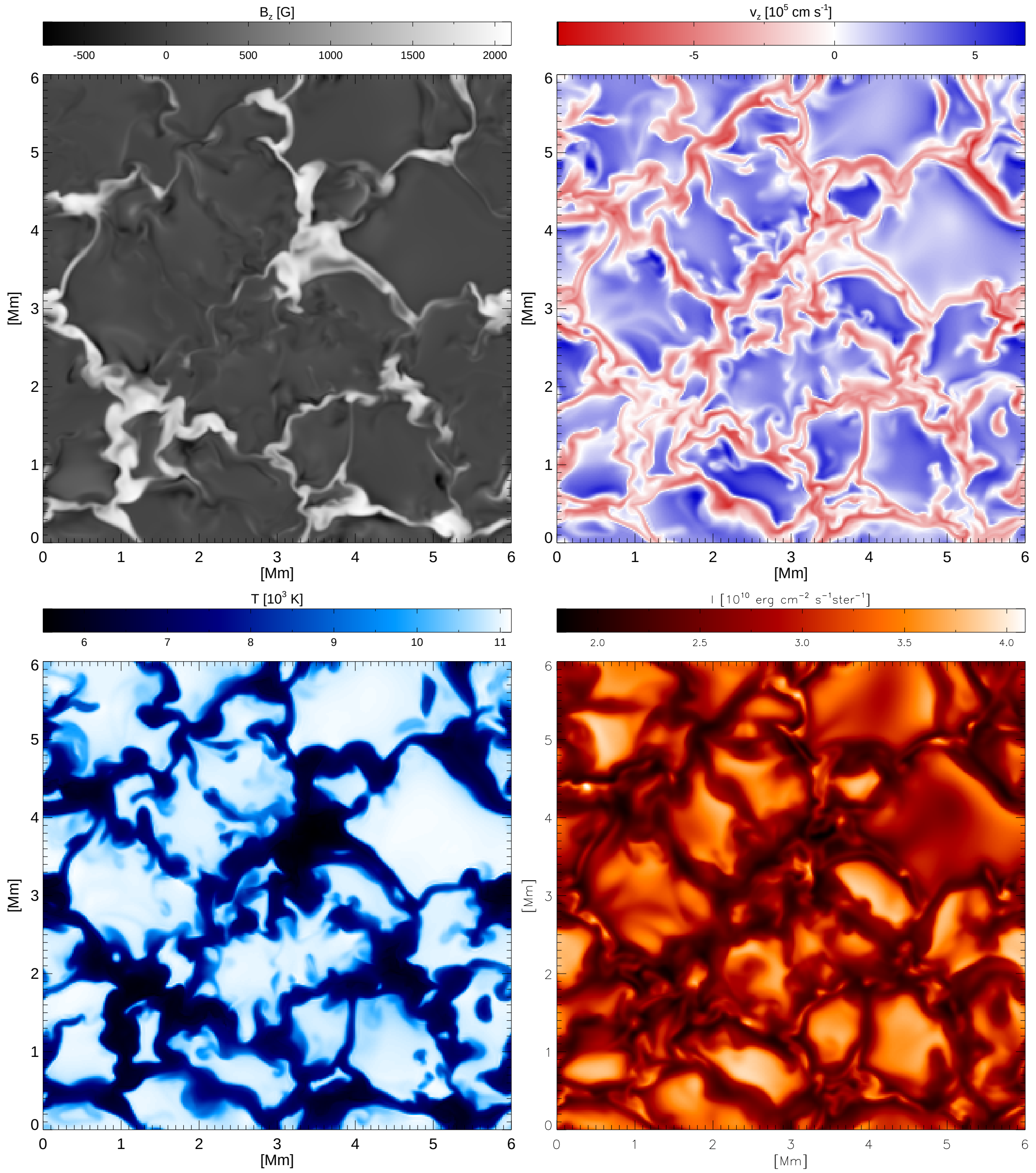

Figure 5.3: *Map of frequency-integrated intensity (radiance, lower right) and horizontal cuts at the the average geometrical height corresponding to optical depth unity of (clockwise from bottom left) temperature, vertical magnetic field and vertical velocity. The "mesoscale" network of magnetic field structures is embedded in the network of granular downflows. Larger field concentrations appear dark, while the brightness of small magnetic structures occasionally exceeds the brightness of granules. Most of the domain exhibits "abnormal" granulation with small granules (compared to the "normal" granules in the upper right corner).*

While convective motions are effectively supressed inside strong field features, downflows occur at their edges. Basically, this confirms the result of earlier MHD simulations (e.g. Deinzer et al. 1984a,b, Knölker et al. 1991), that influx radiation into a magnetic element drives a baroclinic flow in form of a strong downflow jet at its edge; it is also consistent with the observational finding that observed Stokes-V profiles in plage regions show a distinct area asymmetry in combination with a negligible redshift of the zero-crossing wavelength, a fact which can be understood in terms of non-magnetic downflows adjacent to static magnetic fields (Solanki 1989, Grossmann-Doerth et al. 1989, Sigwarth et al. 1999).

Fig. 5.4 shows some statistical properties of the simulation run. As the dataset for the statistics, a series of statistically independent snapshots (i.e. with a temporal cadence exceeding the granule lifetime) was used. A horizontal slice consisting of 8 grid layers (corresponding to a thickness of 112 km), which includes the average $\tau_{5000} = 1$ level, served as the basis for the analysis.

The probability distribution function (PDF) for the magnetic field, signed with the orientation of its vertical component is shown in the upper left panel. There appears to be a superposition of two components. Most of the volume considered is occupied by weak field, the probability density dropping off approximately exponentially with increasing field strength. The distribution reveals a pronounced local minimum at $B = 0$, indicating that magnetic fields, albeit mostly weak, permeate the whole volume, and *field free* regions are apparently avoided. Superimposed on this exponential distribution is a Gaussian "bulge" (the high field strength wing showing the characteristic parabolic shape on a logarithmic scale) with a maximum around 1500 G, which reflects the sheet- and pore-like structures in the network of concentrated magnetic field.

The correlation diagram (joint PDF) of magnetic field strength and inclination angle of the field vector with respect to the horizontal plane given in the upper right panel shows that most of the strong field above the kilogauss level is vertical and upward directed (which is the orientation of the homogeneous initial field), presumably as the result of buoyancy forces acting on the partially evacuated magnetic structures. The inclination angle of weak fields is much more evenly distributed. With decreasing field strength a slight preference for upward directed fields is observed.

The joint PDF of vertical magnetic field and flow velocity multiplied with the sign of its vertical component in the lower left panel (positive velocities correspond to upflows) shows the effect of strong fields on the fluid motions: while flow velocities up to 8 km s^{-1} can be found in weak field regions, the amplitudes of fluid motions are reduced in magnetic structures with field strengths above 1000 G. Fluid motions are not completely supressed, however, since the predominantly vertical fields leave vertical fluid motions largely unaffected. Downflows are preferred inside strong field features.

The lower right panel of Fig. 5.4 shows the joint PDF of the inclination angles of magnetic field vector and flow vector with respect to the horizontal plane. The pronounced diagonal lobe indicates that in most of the volume considered flow field and magnetic field are more or less aligned. In addition to this component, one observes a strong correlation of (strong) vertical magnetic field with downflows.

While we have so far dealt with the properties of the simulation near the visible surface, Figs. 5.5 and 5.6 give an impression of the height dependence of the magnetic field and the vertical velocities, respectively.
Fig. 5.5 shows horizontal slices of B_z at four geometrical height levels. With increasing depth, the network of magnetic field fragments and more isolated structures with high field strength (up to 4000 G in the deep layers close to the lower boundary of the simulation box) form. On the other hand, the outline of the meso-scale network is still recognizable even in the deeper regions. The horizontal location of strong field concentrations with field strengths above 2000 G at $z = 0$ varies only slightly with depth, which indicates that such structures are predominantly vertical. In the upper part of the computational domain ($z > 0$), the field structures expand horizontally and the field strength drops below kilogauss values as the external gas pressure decreases.
Fig. 5.6 shows that, similar to the magnetic field distribution, the the network of downflow lanes becomes fragmented with increasing depth. As a comparison with the downflow structure in the deep layers of pure hydrodynamic convection reveals, the presence of the magnetic field has a stabilizing effect on the downflows, and their tendency to merge into a few strong downdrafts is reduced. Fig. 5.7 shows maps of the vertical velocity at the bottom of the box, for the 200-G run (left) and for a snapshot of the hydrodynamic phase with $\mathbf{B} = \mathbf{0}$ (right). In the nonmagnetic case, the area of connected upflow regions is on average larger and the downdrafts are stronger (for the snapshot shown, they reach a maximum velocity of 10.0 km s^{-1} compared with 7.2 km s^{-1} for the 200-G case).
In the layers above $z = 0$, vertical velocities are strongly reduced (see top left panel of Fig. 5.6). The atmosphere above $\tau = 1$ is stably stratified and vertical velocities are thus decelerated by buoyancy forces.

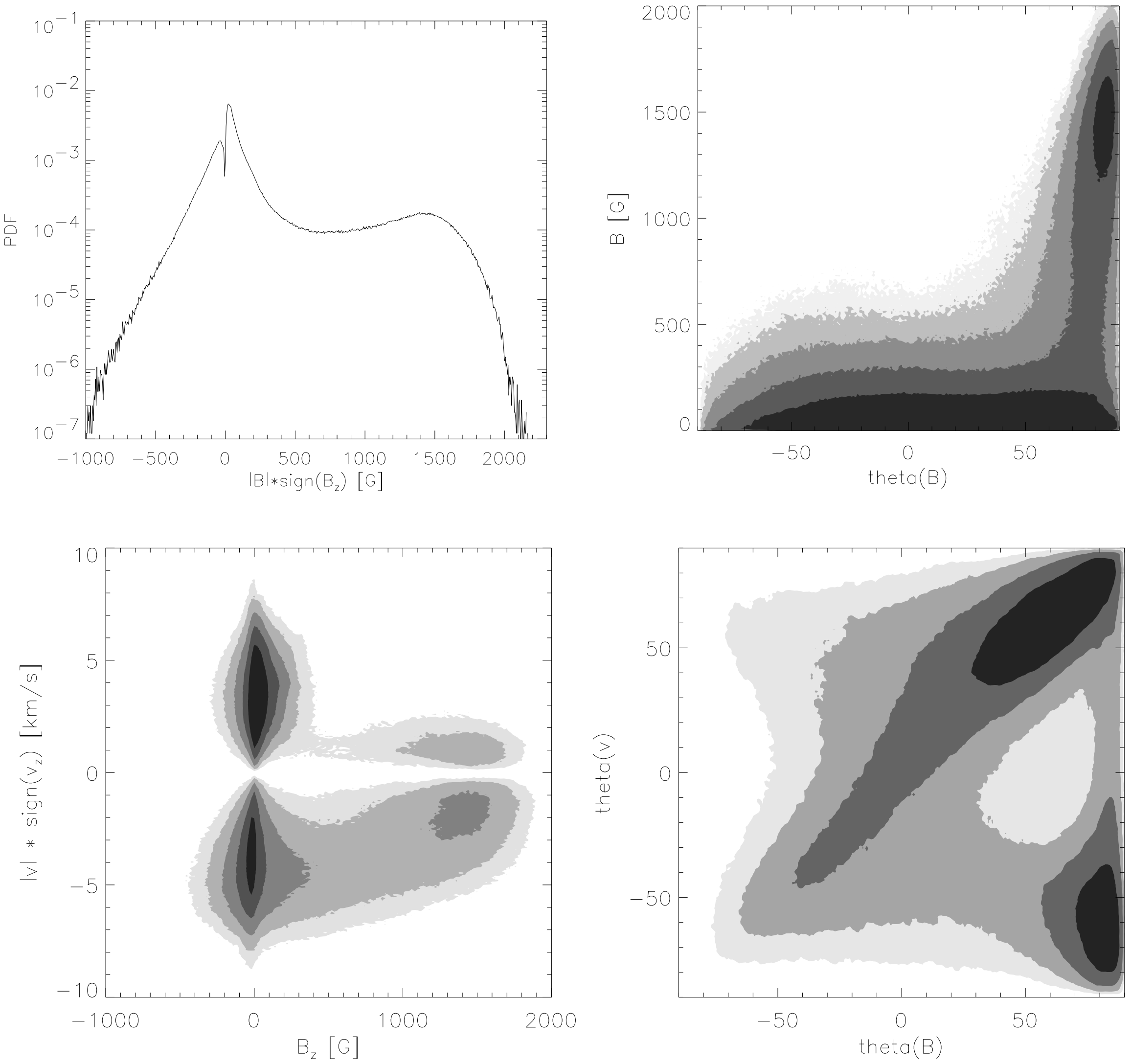

Figure 5.4: *Statistical properties of a layer of* 112 *km thickness around continuum optical depth unity. Upper left: probability distribution (PDF) of the field strength, signed with the vertical orientation of the field vector. Upper right: joint PDF of field strength and the inclination angle of* $\mathbf{B}$ *with respect to the horizontal,* theta(**B**)*. Lower left: joint PDF of flow velocity, multiplied with the sign of its vertical component (upflows are positive), and field strength. Lower right: joint PDF of the inclination angles of the flow,* theta(**v**)*, and of the magnetic field,* theta(**B**)*. The grey-scaling indicates the probability density on a logarithmic scale.*

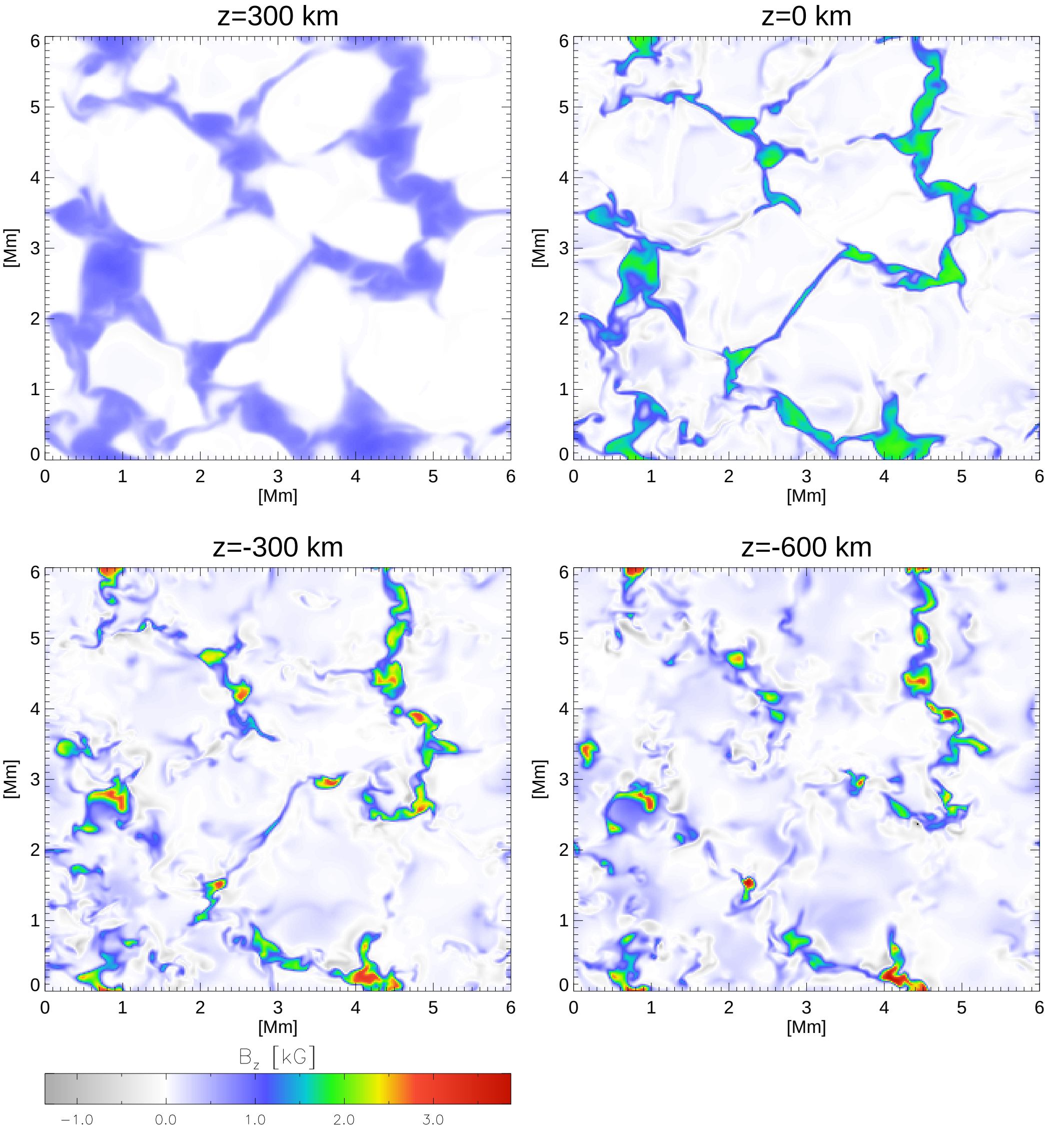

Figure 5.5: *Horizontal cuts of vertical magnetic field at four different height levels (z increases in the upward direction). With increasing depth the magnetic network becomes increasingly fragmented and the flux is concentrated in more isolated structures of high field strength. The mesoscale pattern persists throughout the complete height range.*

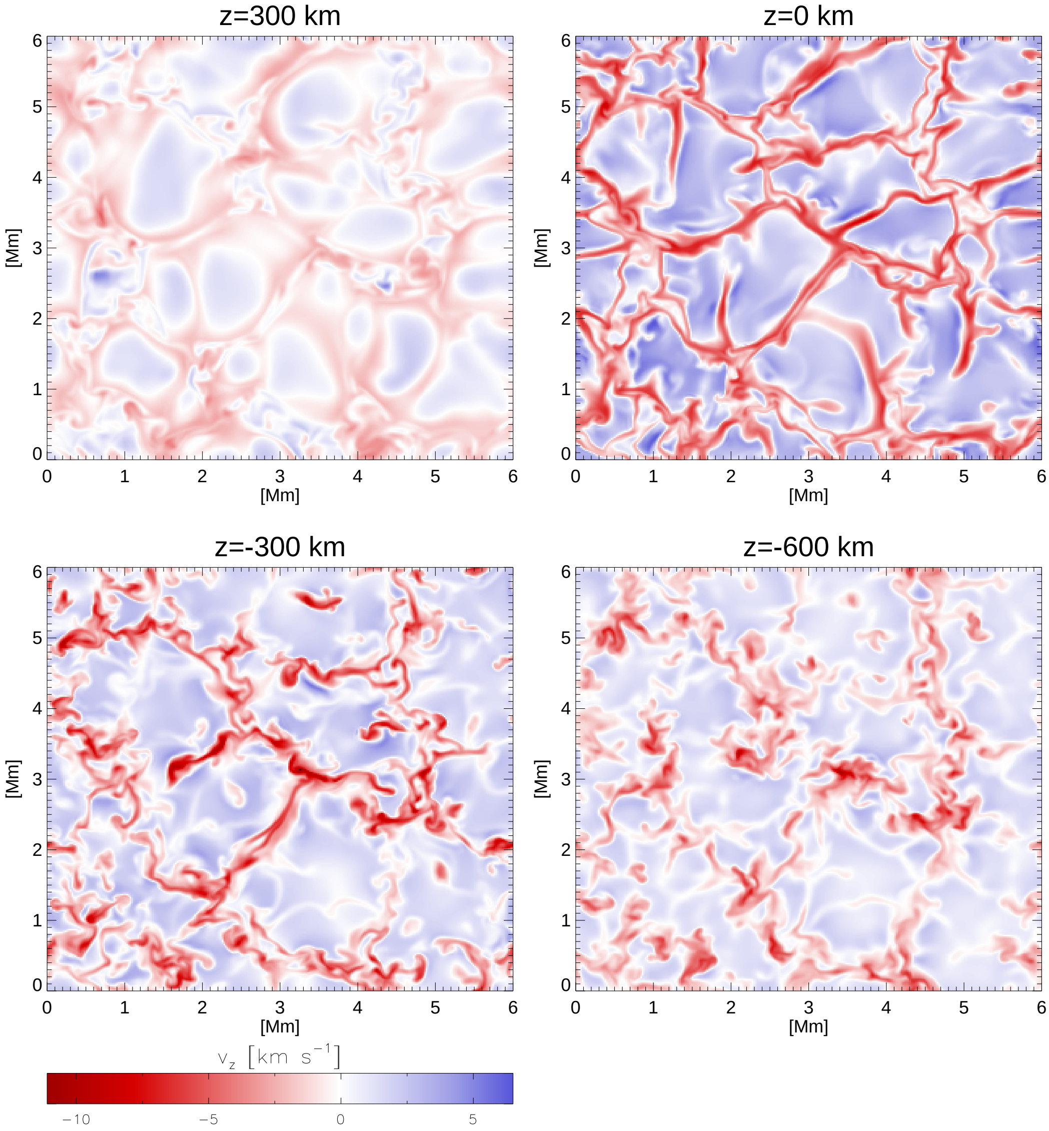

Figure 5.6: *Horizontal cuts of vertical velocity at four different height levels. With increasing depth the downflow lanes tend to fragment into more isolated downdrafts. On the whole, however, the meso-scale downflow network can be identified over the complete height range of the computational domain.*

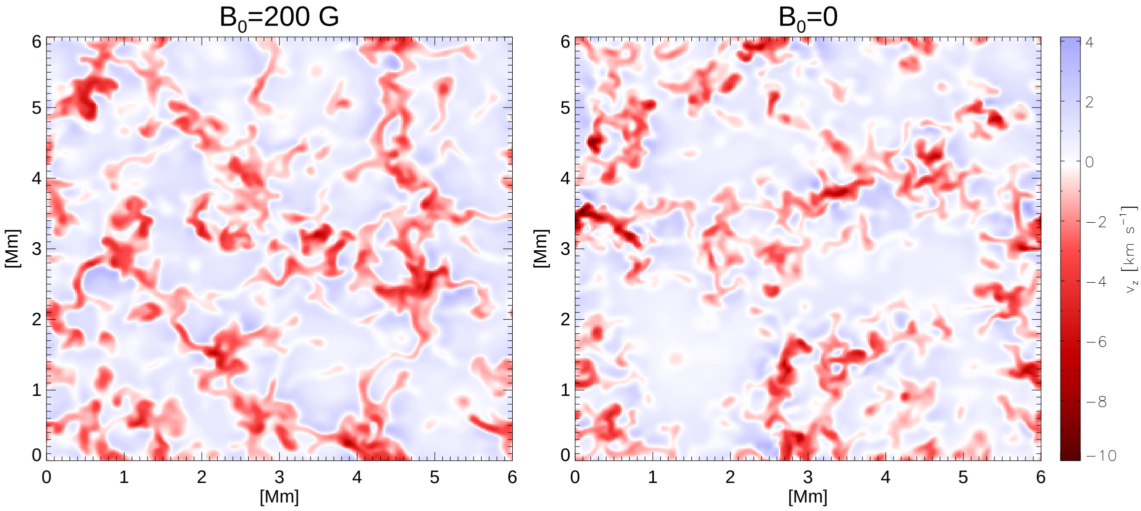

Figure 5.7: *Vertical velocity at the bottom of the box ($z = -800$ km), for the 200-G run (left panel) and purely hydrodynamic convection without magnetic field (right panel). In the non-magnetic case, downdrafts are stronger and more isolated, and on average the area of connected updrift-regions is larger.*

In the upper parts of the computational domain, the structure of horizontal flows undergoes a characteristic change with height. This is illustrated by Fig. 5.8, which shows horizontally averaged (root-mean-square) velocities of horizontal flows (left panel) and horizontal rms temperature fluctuations (right panel) as a function of height, in strong-field and weak-field regions, respectively: As the left panel shows, horizontal flows are stronger outside magnetic field concentrations than inside below $z = 400$ km, and reach a maximum around $z = 200$ km where the granular upflows turn over and converge horizontally towards the downflow lanes. Above $z = 400$ km a different picture is obtained: the rms horizontal velocity inside magnetic structures *increases* with height, while the velocities outside decrease significantly. As a result, horizontal flows have larger amplitudes *inside* magnetic fields. Above $z = 500$ km these flows are accompanied by strong temperature fluctuations (Fig. 5.8, right panel), which clearly exceed the fluctuations outside magnetic fields. Fig. 5.9 shows horizontal cuts at $z = 540$ km of an exemplary snapshot. Strong, predominantly vortical flows inside magnetic field concentrations with maximum velocities up to 10 km s^{-1} are closely correlated to temperature fluctuations. The fact that these fluctutations are also correlated to density fluctuations suggests that they are caused by adiabatic expansion and compression of the plasma due to the vortical flows. This appears plausible since the radiative energy exchange rates are very small at this height (the atmosphere being almost transparent) and the gas is expected to behave almost adiabatically. As the example shown in Fig. 5.10 illustrates, one observes a correlation between flows inside magnetic structures at large heights and converging granular flows

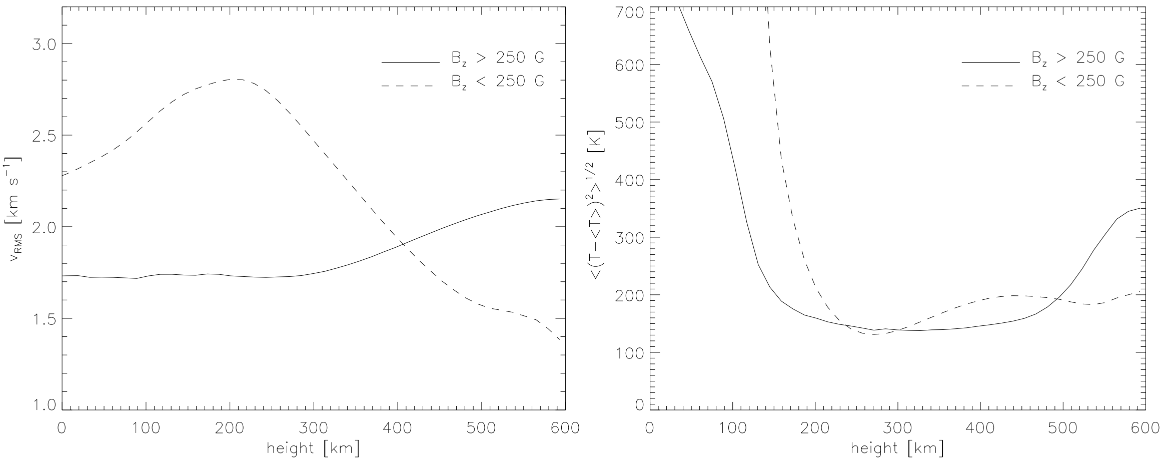

Figure 5.8: *Left panel: rms horizontal velocity in regions of strong and weak magnetic field as function of height. A height-independent threshold value of* 250 *G was chosen. Right panel: rms temperature fluctuations inside and outside strong field regions.*

immediately outside magnetic structures at deeper levels around $\tau_{5000} = 1$. The anticlockwise whirl flow at $z = 540$ km (upper panel) corresponds to a net circulation of granular flows around the magnetic element with the same orientation at $z = 100$ km (lower panel). It is conceivable that the shear due to such surrounding flows excites torsional Alfvén waves which propagate upward along field concentrations. With the reflecting boundary conditions presently used, however, we cannot expect to realistically describe the behaviour of these waves near the top of box. Therefore, a thorough analysis of the excitation mechanism and an assessment of its relevance for vertical energy transport into the upper parts of the solar atmosphere requires simulations with a more realistic upper boundary condition. Such simulations can be carried out with future versions of the code, which will include a transmitting upper boundary.

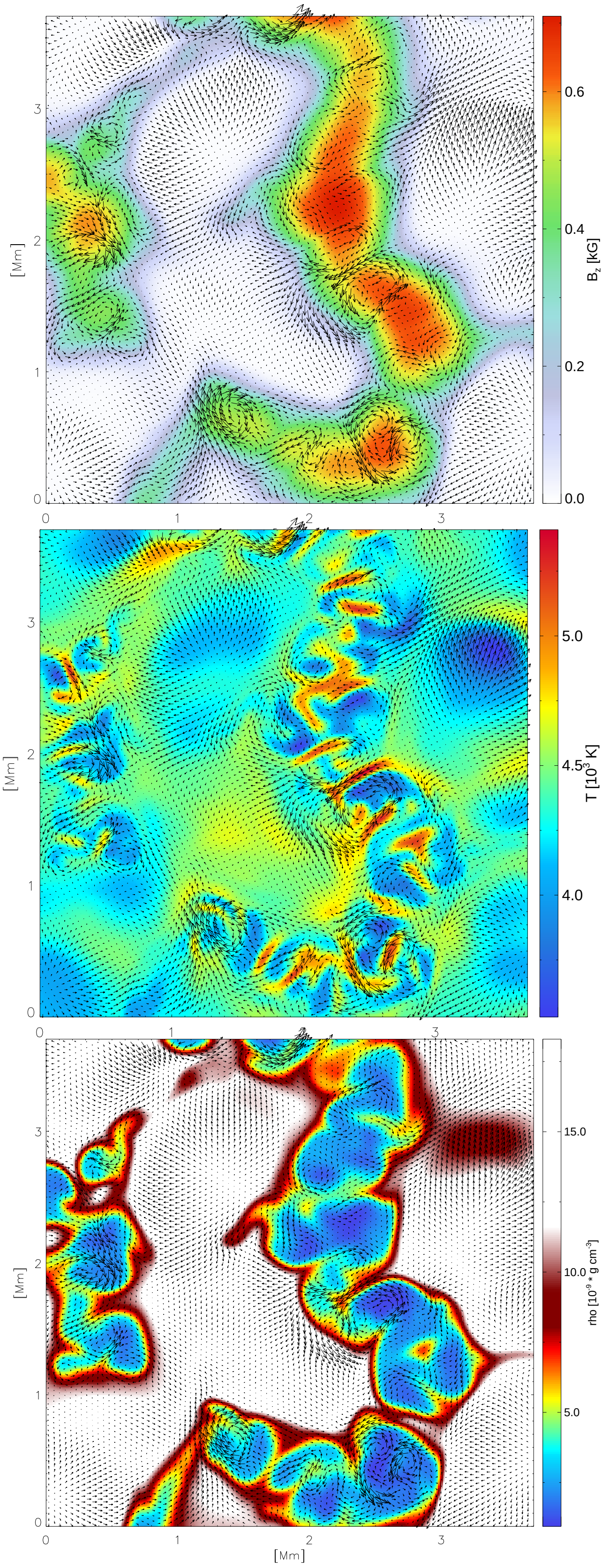

Figure 5.9: *Upper panel: vertical magnetic field (color-coded) with superimposed horizontal velocity field for a horizontal slice near the top of the box (z = 540 km). Only a part of the computational domain is shown. Middle panel: the same region with color-coded temperature. Lower panel: color-coded density. In the upper parts of the simulation box, strong horizontal whirl-flows with maximum amplitudes around 10 km s^{-1} occur inside magnetic field structures. They are accompanied by strong temperature fluctuations. These fluctuations are correlated with fluctuations of density, suggesting that they are caused by adiabatic expansion and compression.*

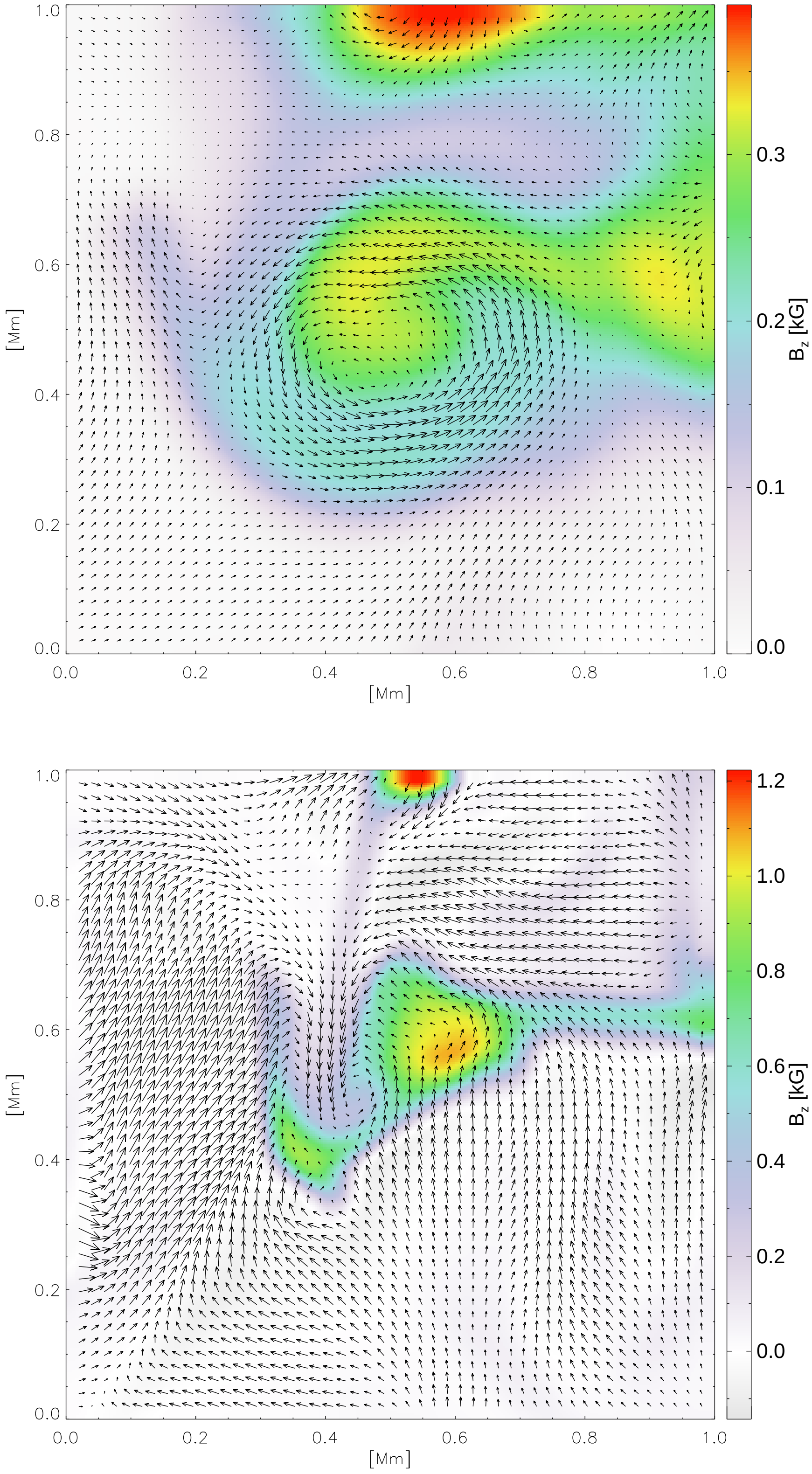

Figure 5.10: *Detailed view of the flow and magnetic structure of a flux concentration. Upper panel: velocity field and color-coded vertical magnetic field at* $z = 540$ km. *Lower panel: the same at* $z = 100$ km.

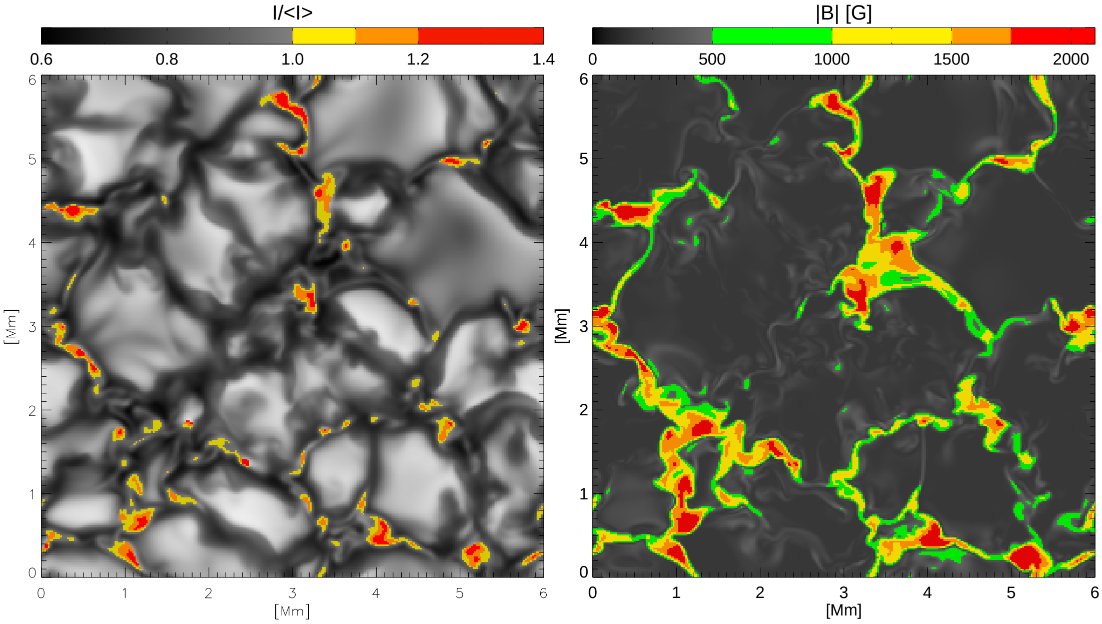

Figure 5.11: *Left: Intensity map. Magnetic structures with* $|\mathbf{B}| > 500$ G *and above-average intensity are colored. Right: colored map of magnetic field strength at* $z = 0$. *The brightest magnetic structures are preferentially associated with strong fields around* 2000 G.

5.1.2 Relation between magnetic field strength and emergent intensity

It is a well established observational fact that the brigthness of magnetic structures in the photosphere strongly depends on their size. While small field concentrations appear as bright points in intensity pictures, larger structures like pores and sunspots appear dark as a result of the reduced convective energy transport in their interior (see e.g. Zwaan 1987 for an overview of the hierarchy of magnetic elements). While the relation between brightness and magnetic field of small photospheric elements has been extensively studied theoretically in two-dimensional MHD simulations (e.g. Deinzer et al. 1984a,b, Steiner et al. 1998, Grossmann-Doerth et al. 1998), the simulation discussed here also includes the transition to the regime of darker pore-like structures with diameters of the order of 1000 km.

The intensity maps and diagrams shown in this chapter are based on the radiation intensity which is obtained as a result of the non-grey radiative transfer calculations and represents an approximate frequency-integrated ("bolometric") intensity. While the corresponding intensity maps are not directly comparable to observations, they should be reasonably close to broad-band images in the visual part of the spectrum, where most of the energy of the emergent radiation resides.

Fig. 5.11 shows colored maps of emergent intensity and vertical magnetic field for an exemplary snapshot. The brightest magnetic structures are typically found in regions of high field strength of the order of 2000 G at $z = 0$. However, not all strong-field features stand out as particularly bright; larger structures with extended regions of magnetic fields above 1000 G tend to appear darker than average. This impression is confirmed quantitatively by Fig. 5.12. The left panel shows the correlation diagram (joint PDF) of magnetic field strength at $z = 0$ against emergent intensity, based on simulation data of approximately one hour simulated time. While a large part of the magnetic regions has an intensity below the average value, the largest field strengths show a trend towards increased brightness, with maximum intensities exceeding those of bright nonmagnetic regions (i.e., granules). The right panel shows the probability distribution of magnetic field strength in bright (solid line) and dark (dashed line) magnetic regions, both curves being separately normalized to unity. While the fields with below-average brightness have rather a flat distribution up to fields of 1500 G, the distribution for the bright features shows a steep increase with increasing field strength and reaches a pronounced maximum at 1700 G.

In the remaining part of this section, the connection between magnetic field and emergent intensity is illustrated in more detail, considering as examples a bright magnetic sheet and a dark micropore.

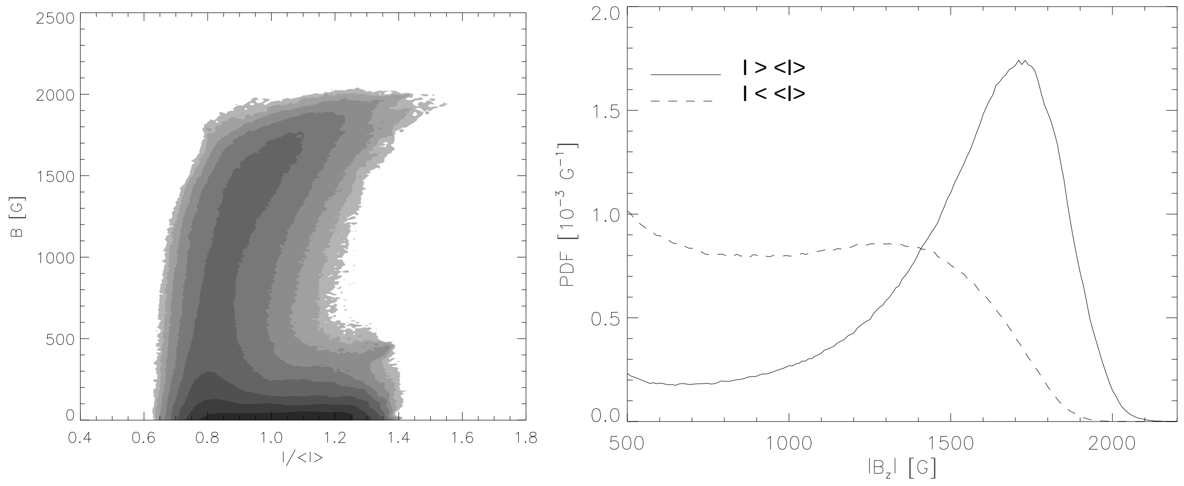

Figure 5.12: *Left: Correlation diagram (joint PDF) between magnetic field strength and brightness. The grey-shading indicates the probability density on a logarithmic scale (spaced apart by* 0.5 *on the* $\log_{10}$*-scale). Right: Probability distribution functions of the magnetic field strength inside the magnetic network* ($|B_z| > 500$ G)*, for regions brighter and darker than average, respectively.*

Vertical cut through a sheet-like structure

Fig. 5.13 shows magnetic field and intensity maps of a typical bright, elongated magnetic structure embedded in a dark downflow lane. The red line marks the position of the vertical cut through this structure shown in Fig. 5.14. As the upper left panel of Fig. 5.14 illustrates, the partial evacuation of the magnetic structure leads to a depression of the visible surface inside the sheet (the yellow line, indicating the level $\tau_{\mathrm{Ross}} = 1$). This results in radiation flowing in from the hot neighbouring granules through the sidewalls, heating up the interior of the sheet. While the net radiative heating inside the sheet is small (see the upper left panel), indicating an approximately steady state, the component of the heating rate due to horizontal energy exchange in the direction along the red line, $Q_{\mathrm{hor}} = -\partial_x(\mathbf{F}_{\mathrm{rad}})_x$ (x is the horizontal coordinate along the cut), reveals a significant heating of the sheet, which is strongest in a layer of roughly 100 km thickness immediately underneath the visible surface. As the lower right panel shows, the sheet approximately maintains radiative equilibrium by vertical cooling, $Q_{\mathrm{vert}} = -\partial_z(\mathbf{F}_{\mathrm{rad}})_z$, i.e., the energy coming in horizontally is radiated in the upward direction. This example confirms the basic mechanism for brightness enhancement that was already found in earlier, more simplified models of photospheric magnetic elements (e.g. Deinzer et al. 1984a,b, Knölker et al. 1988) and demonstrates that results of idealized, two-dimensional models are indeed relevant for the explanation of some aspects of three-dimensional magnetoconvection.

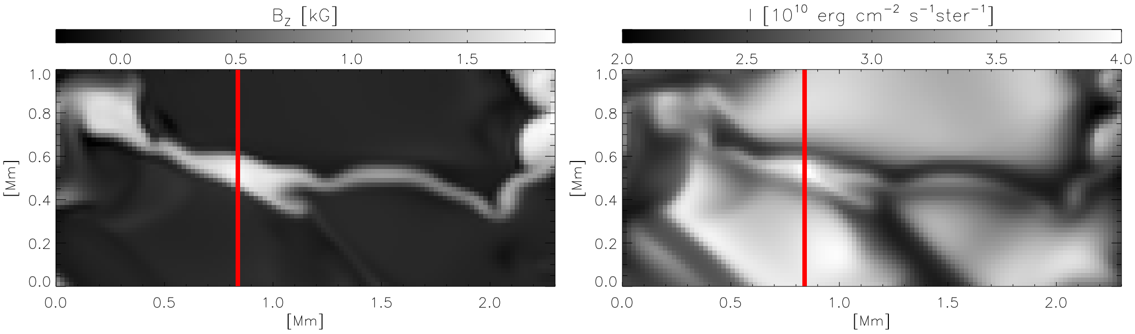

Figure 5.13: *Vertical field strength at $z = 0$ (left) and intensity map (right) for a sheet-like magnetic structure. The red line indicates the position of the cut shown in Fig. 5.14.*

Fig. 5.15 illustrates how the differences in temperatur e structure inside the magnetic element and in the surrounding downflows lead to intensity variations. Shown are vertical profiles of the frequency-integrated Planck function $\sigma T^4/\pi$ for the intensity maximum inside the sheet at $x = 520$ km and for the adjacent dark lane at $x = 630$ km (see Fig. 5.16, upper panel, for the intensity profile along the cut). As a result of radiative heating, the temperature gradient is flatter and temperatures are higher around $\tau_{\rm Ross} = 1$ inside the sheet. As the diagram shows, the optical depth range which shows the strongest temperature excess in the interior coincides with the maximum of the contribution function for the emergent intensity,[2] resulting in a pronounced intensity contrast between the sheet and its immeditate surroundings.

Another heating mechanism is Joule dissipation near the edges of the magnetic sheet, where the gradients in field strength are large. In the photosphere, this effect is expected to be small compared to the radiative heat influx because of the high electric conductivity. Since the value of the conductivity in this simulation is unrealistically low (which is an inevitable consequence of the limited spatial resolution), Joule heating tends to be overestimated. The lower panel of Fig. 5.16 shows joule and lateral radiative heating across the sheet at $z = -80$ km, where the latter is most pronounced. Obviously, the radiative effect dominates over Joule dissipation, which indicates that the effects of limited grid resolution do not seriously affect the temperature structure obtained from the simulation.

---

[2] Strictly, in the non-grey simulations the calculated emergent intensity is the sum of the contributions from the different opacity bins, each with a contribution function localized around $\tau_{\rm bin} = 1$. However, since the contribution of the continuum dominates, the depth level $\tau_{\rm Ross} = 1$ is relevant for the total radiance.

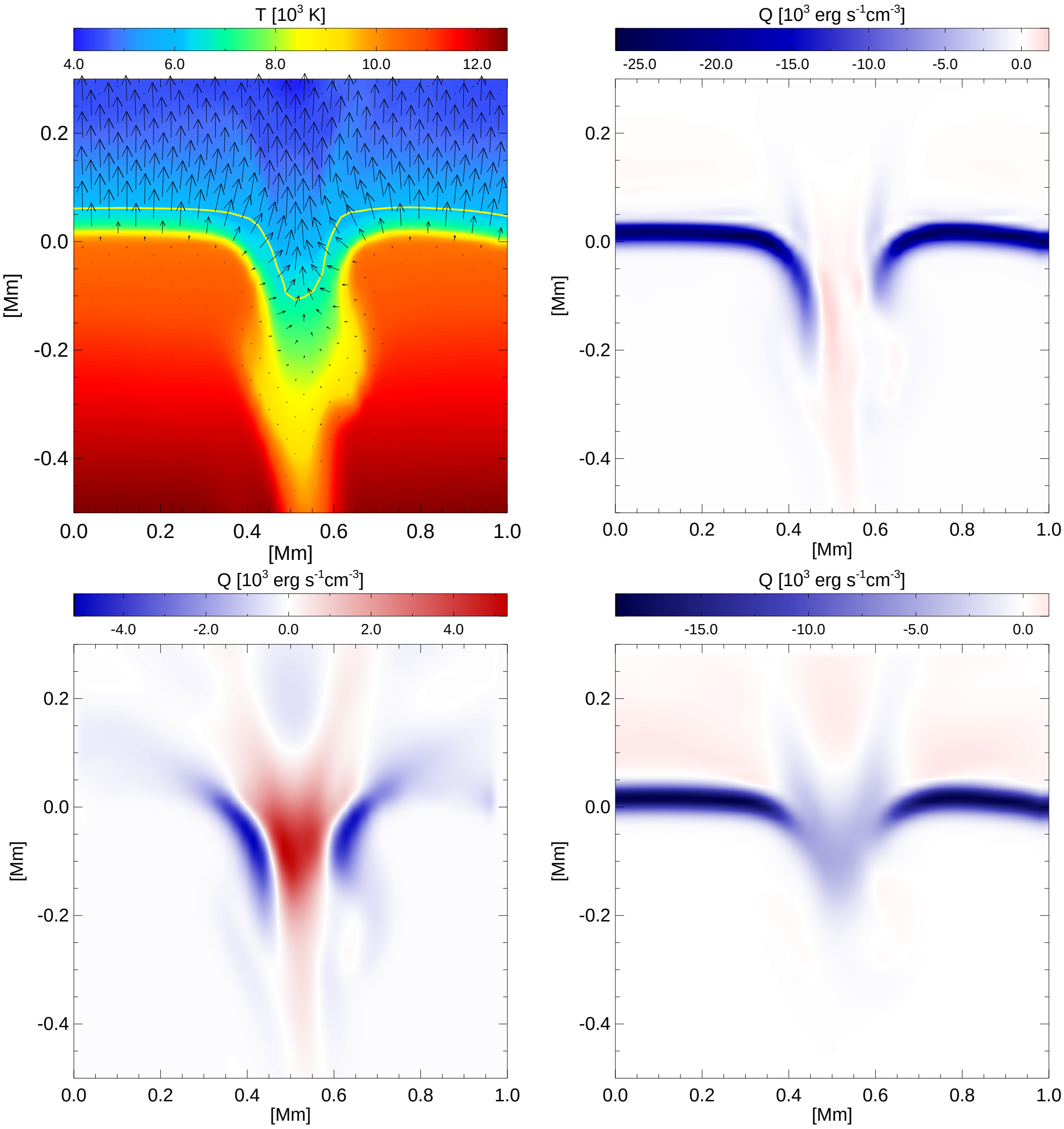

Figure 5.14: *Vertical cut through the sheet-like magnetic structure shown in Fig. 5.13. Top left: color-coded temperature and radiative flux vectors; the yellow line indicates the level* $\tau_{\text{Ross}} = 1$. *Top right: radiative heating rate,* Q_{rad}. *Bottom left: horizontal radiative energy exchange. Bottom right: vertical radiative energy exchange.*

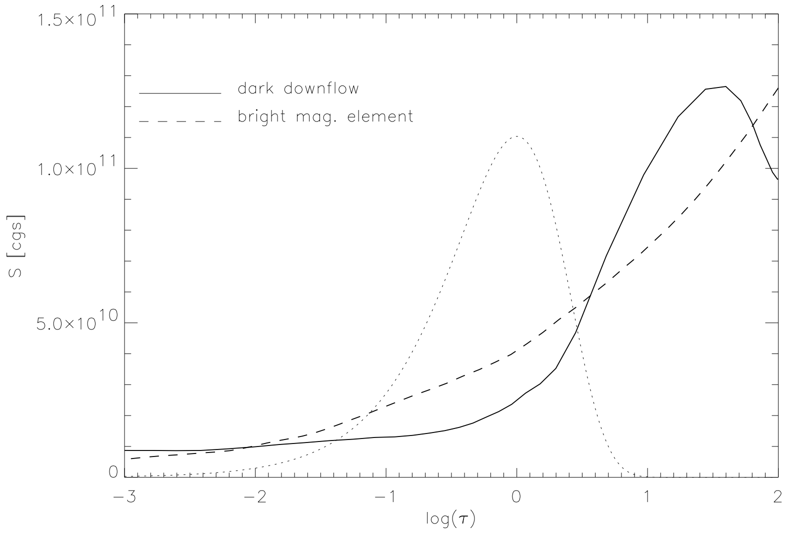

Figure 5.15: *Solid line: Vertical profile of the frequency-integrated Planck function (on the* $\log \tau_{\mathrm{Ross}}$ *scale) for the dark lane (*x *=* 630 km *in Figs. 5.13 - 5.16) next to the magnetic sheet. Dashed line: same for the intensity maximum inside the sheet at* $x = 520$ km. *The dotted line shows the contribution function for the vertically emergent intensity in arbitrary units.*

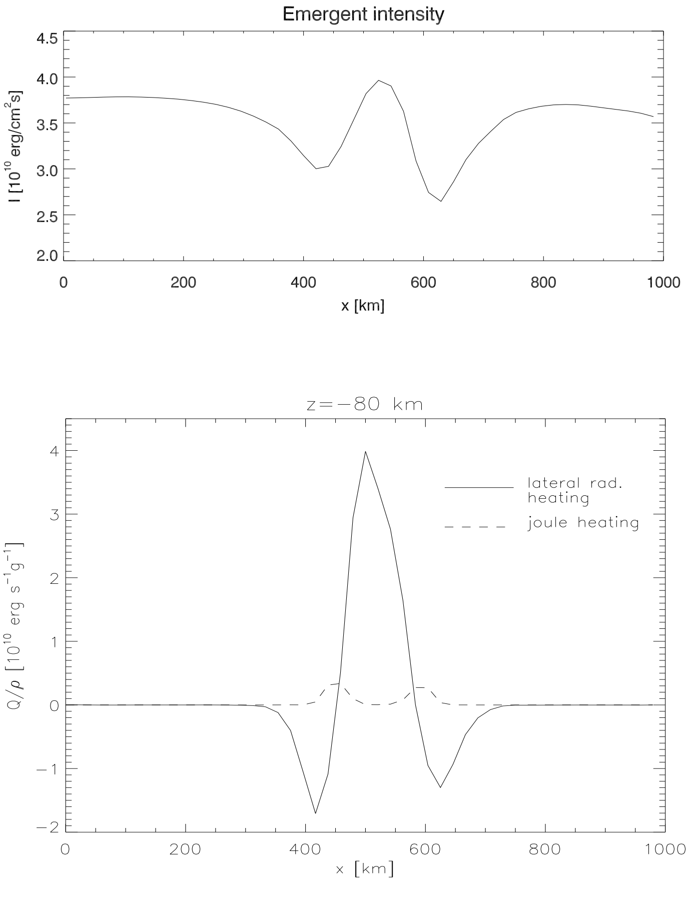

Figure 5.16: *Radiative properties of the magnetic sheet shown in Fig. 5.13. Upper panel: Emergent intensity along the cut marked in Fig. 5.13. Lower panel: The solid line shows along the same cut the heating rate due to horizontal influx of radiation energy into the sheet,* Q_{hor}, *at a depth of* 80 km *below* $z = 0$. *The dashed line shows the joule heating occuring at the sheet boundaries at the same depth.*

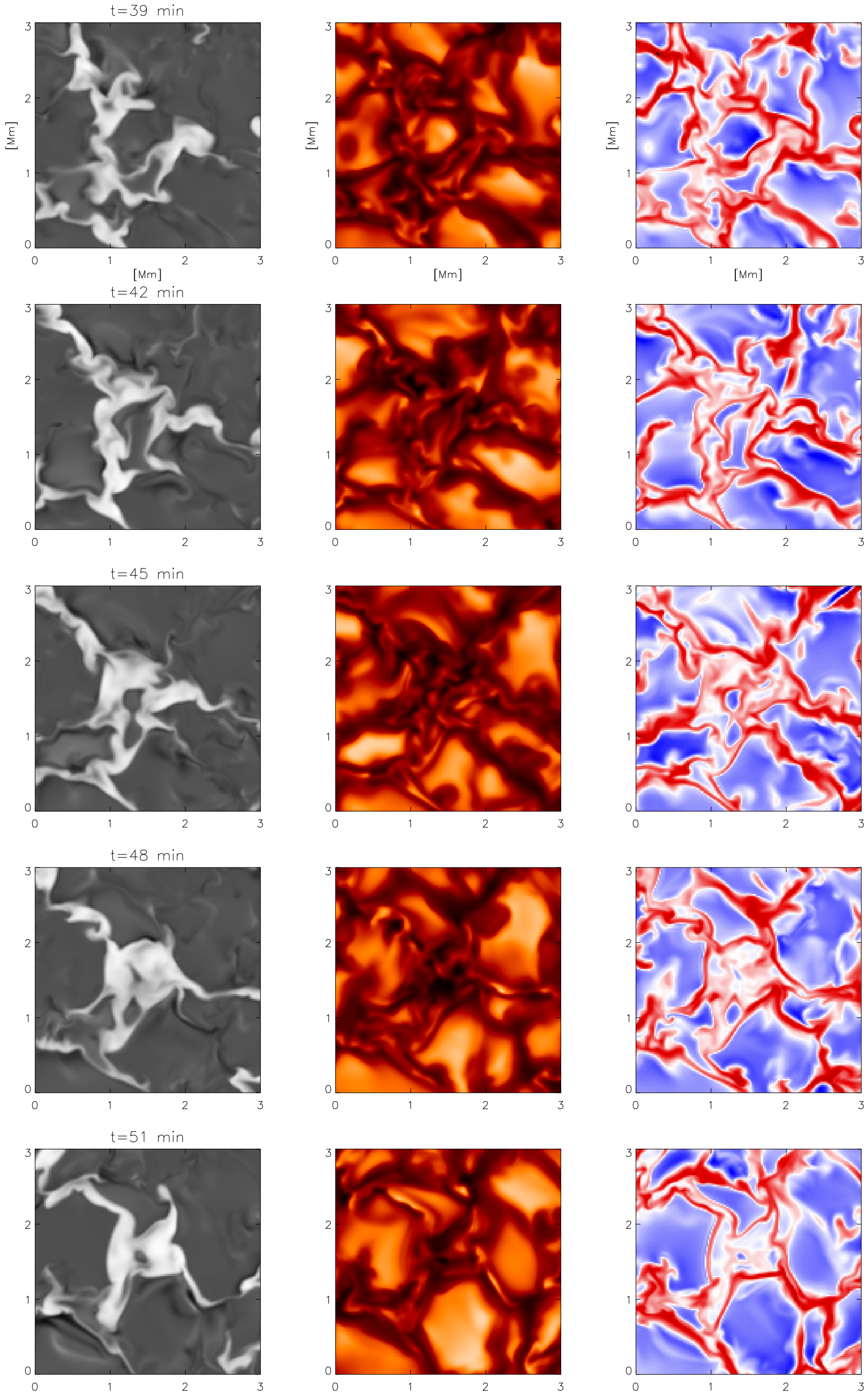

Figure 5.17: *Time series of vertical magnetic field (left), intensity (middle), and vertical velocity (right) during the formation of a micropore. An initially bright, small granule is squeezed out of existence by its neighbours. As it shrinks, the magnetic field surrounding it forms a small pore which appears dark in the intensity picture.*

Formation of a micropore

Fig. 5.17 illustrates the formation process of a micropore. At the beginning of the time sequence shown, a small granule is surrounded by magnetic field, which is embedded in a complex structure of downflows and forms a ring around the granule. Subsequently, the initially bright granule is squeezed out of existence by its neighbours; the surrounding magnetic flux converges to form a dark micropore with a diameter of approximately 1000 km. In its interior, vertical motions are strongly reduced, which implies that convective energy transport is almost completely supressed. The micropore is, however, punctuated by small, hot, non-magnetic upwellings, which penetrate it from below, carrying hot plasma to the surface. While the shape of the micropore changes continuously, it more or less retains its position. Roughly 15 minutes after the end of the sequence shown, most of the magnetic flux of the micropore has been carried away into the magnetic network and the pore has dissolved. Apparently, the size of the micropores which are formed in this simulation is too small to structure the convective flow around them in a way that would stabilize them and extend their lifetime beyond about 1-2 convective turnover times.

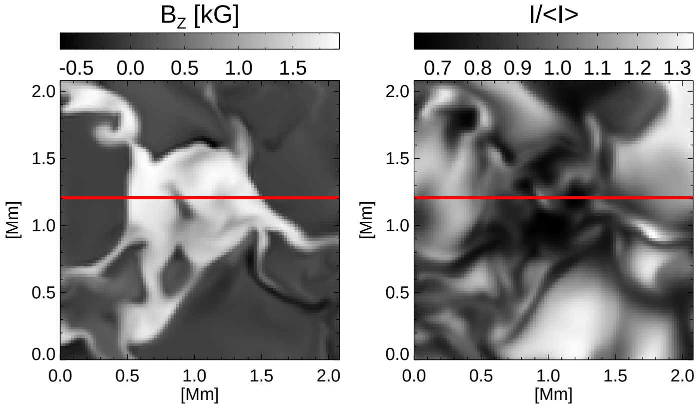

Figure 5.18: *Vertical field strength at $z = 0$ (left) and intensity map (right) of a micropore. The red line indicates the position of the cut shown in Fig. 5.19*

More insight into the internal structure of the pore and the relation between magnetic field strength and intensity can be gained from Fig. 5.19, which shows a vertical cut across the pore at t=48 min along the red line shown in Fig. 5.18. As the magnetic field plot (second from top in Fig. 5.19) indicates, the distribution of the field strength within the micropore is quite inhomogeneous. Variations in magnetic field strength on a given geometrical height level are accompanied by variations in gas pressure that keep the total pressure approximately constant. As a result, regions of reduced field strength have higher density, which in turn raises the level of optical depth unity relative to the neighbouring stronger fields. These variations in the height of the $\tau = 1$ level translate into intensity fluctuations along the horizontal coordinate of the cut (Fig. 5.19, top panel). The intensity minimum at $x = 1.2$ Mm corresponds to a region with relatively weak field

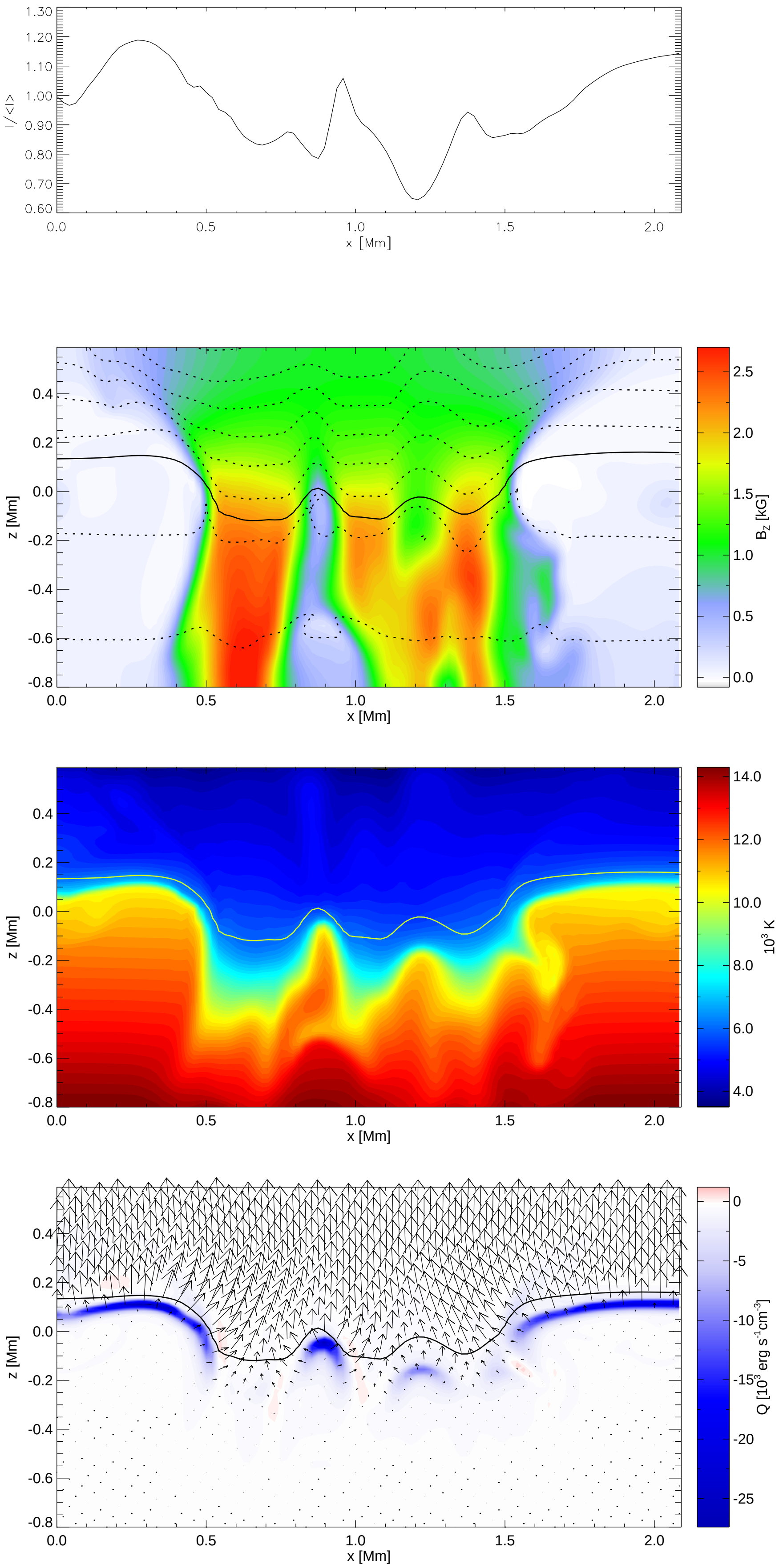

Figure 5.19: *Vertical cut through a micropore. From top to bottom: Emergent radiation intensity along the horizontal coordinate; color-coded vertical magnetic field strength with superimposed iso-density lines (dotted); color-coded temperature; color coded radiative heating rate with superimposed vectors of the radiative energy flux, projected onto the vertical plane; in the lower three panels, the solid line marks the level* $\tau_{\rm Ross} = 1$.

around 1200 G at $\tau_{\mathrm{Ross}} = 1$. Accordingly, the $\tau_{\mathrm{Ross}} = 1$ level is located at lower temperatures compared with the adjacent regions of high field strength around 2000 G, making it appear darker. At $x = 0.9$ Mm, the remnant of the bright granule that shrunk during the formation process appears as hot, weakly magnetized region inside the pore, extending from the bottom to the visible surface. The intensity maximum at $x = 0.95$ Mm coincides with its upper right edge where hot gas has risen close to the surface. As the bottom panel shows, this hot plume is strongly cooling there, emitting radiative energy both upwards and horizontally. In the strong field regions, the net radiative heating rate is close to zero and no conversion from convective to radiative energy flux takes place. The radiative flux vectors in the bottom panel of Fig. 5.19 indicate that almost all the radiative energy leaving the strong-field regions in the upward direction is provided by its hot, non-magnetic surroundings by means of lateral heating. In comparison with smaller, sheet-like structures, the micropore appears darker since the energy which is supplied by the hot walls is radiated upwards over a larger area, while the lateral energy input only scales as the diameter of the structure.

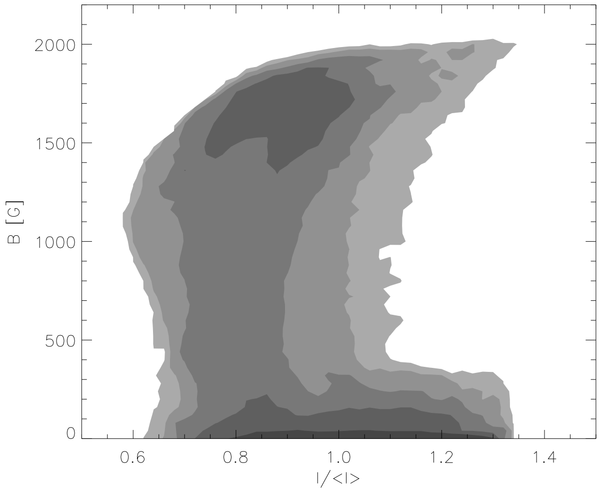

Figure 5.20: *Correlation diagram between magnetic field and emergent intensity in the micropore shown in Fig. 5.17, based on a 10-minute time interval starting at $t = 48$ min.*

Fig. 5.20 shows the correlation between intensity and magnetic field at $z = 0$ for the micropore, averaged over a ten-minute period after it has formed at $t = 48$ min. The smallest intensity values are obtained for field strengths between 1000 and 1200 G. For higher field strengths, the minimum intensity increases systematically. The pronounced high-intensity “tail” of the distribution at $B \approx 2000$ G is a result of bright, thin filaments, which extend from the edges of the pore and are included in the area on which the joint PDF is based. Altogether, the diagram corroborates the impression gained from the cross section of Fig. 5.19, namely that the darkest parts of the pore correspond to intermediate field strengths, while the strongest field concentrations, radiating at deeper, hotter layers, are brighter.

5.2 Simulation runs with $B_0 = 10$ G and 50 G

In comparison with the 200-G run, the “network run” with an average field of 10 G (see Fig. 5.21 for horizontal slices) forms smaller, more isolated magnetic structures. The total magnetic flux of this run is not sufficient to form a coherent magnetic network at $z = 0$, although the more elongated thin structures along the intergranular lanes still outline parts of a “mesoscale” network. On the whole, however, the magnetic field is too weak and localized to seriously inhibit the convective motions, and, in contrast to the 200-G run, abnormal granulation with reduced granule sizes is not observed. Small, intense magnetic structures with field strengths up to 1500 G at $z = 0$ are found at downflow vertices and appear as bright dots in the intensity picture. Larger, dark pore-like structures are not formed. Accordingly, the joint PDF of magnetic field and intensity (Fig. 5.22) shows a clear trend towards higher brightness with increasing field strength. The temporally averaged rms intensity contrast is approximately 18 percent and exceeds the contrast of the 200-G run (15 percent). This difference in contrast is mainly caused by the brightness enhancement within the magnetic network of the 200-G run, which lifts the brightness of a considerable part of the area between granules above the intensity level of the dark non-magnetic downflow lanes of the 10-G run. The lifetime of strong flux concentrations with field strengths around 1500 G varies between 30 and 200 seconds. A precise definition of the lifetime is, however, difficult since the magnetic flux is permanently redistributed, with strong, isolated features and weaker, elongated structures being continuously transformed into each other.

Fig. 5.23 shows horizontal slices of the vertical magnetic field at four different geometrical height levels. Similar to the 200-G run, the magnetic field undergoes some fragmentation into irregular small-scale structure. Strong field concentrations remain identifiable throughout the whole height range of the computational domain and have the form of predominantly vertical flux tubes.

The simulation run with an inital magnetic field of 50 G shown in Fig. 5.24 shares several properties with both of the simulation runs already discussed. As in the 10 G case, no coherent magnetic network at $z = 0$ is formed, and the largest magnetic structures with diameters around 500-700 km are too small to appear as dark features in intensity maps. The maximum field strength at $z = 0$ is around 2200 G, as in the 200-G run. The intensity picture appears to be more irregular than for the 10-G run and a trend towards reduced granule sizes can be observed.

Fig. 5.25 shows the probability distribution functions for all three simulation runs. The PDF for the 10-G run is mainly a stretched exponential with an extended wing of the dominant polarity, which reflects the magnetic structures in the kilogauss range. The shape of a stretched exponential is reminiscent of the

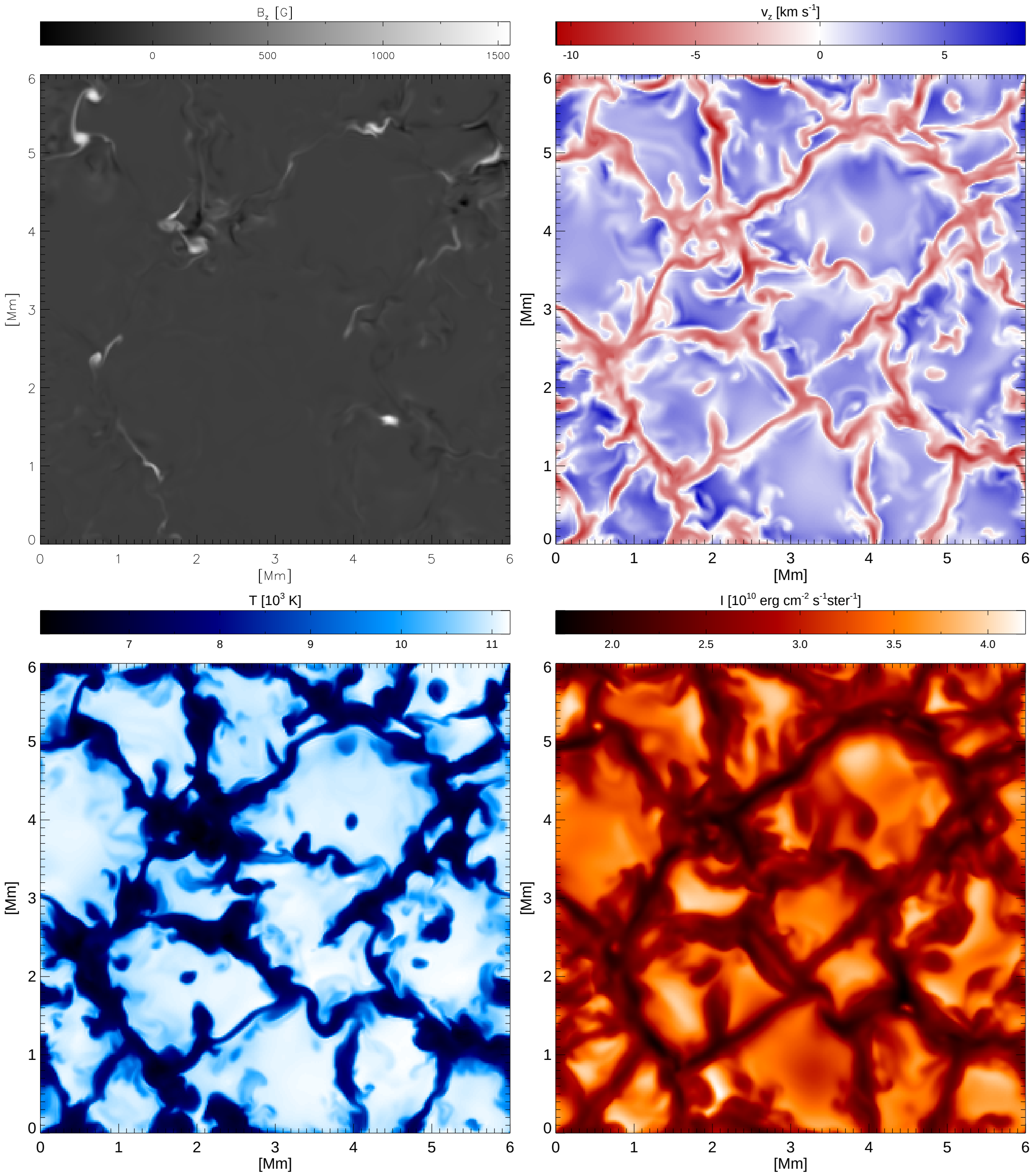

Figure 5.21: *Map of frequency-integrated intensity (lower right) and horizontal cuts at the the average geometrical height corresponding to optical depth unity of (clockwise from bottom left) temperature, vertical magnetic field and vertical velocity for the run with an average vertical field strength of 10 G.*

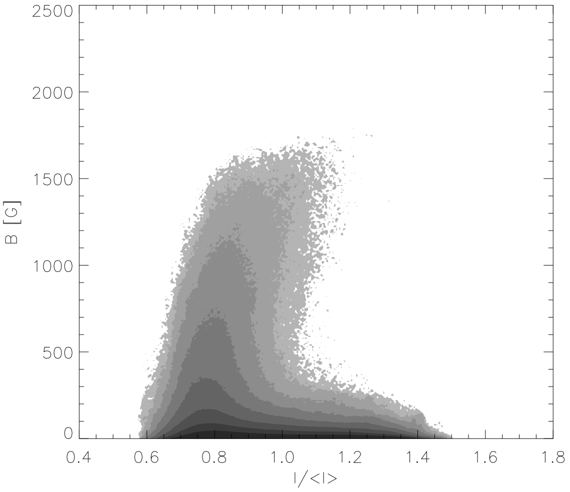

Figure 5.22: *Correlation diagram of emergent intensity and magnetic field strength at $z = 0$ for the simulation run with an average vertical field of 10 G. The intensity systematically increases with field strength, reflecting the absence of particularly dark flux concentrations.*

distribution obtained by Emonet & Cattaneo (2001) for a zero mean field (dynamo) simulation of magneto-convection in the (incompressible) Boussinesq approximation and is apparently a robust feature of weak-field magneto-convective simulations. It is indicative of high intermittency of the magnetic field, i.e. the probability of very strong and very weak fields is higher than if the field were distributed by a random process with a Gaussian probability distribution function.

In the plage runs the wing of positive (dominant) polarity grows and shows a pronounced local maximum for the 200-G case. For the 50-G run, the wing corresponding to the opposite polarity also is a stretched exponential, while it becomes a pure exponential in the 200-G run. Possibly, the interaction between convective motions and the Gaussian hump of strong fields creates a negative-polarity components which is superimposed on the stretched exponential. The different shapes of the weak- and strong-field components suggest that the intensification of the initial field and the generation of weak fields are the result of different processes.

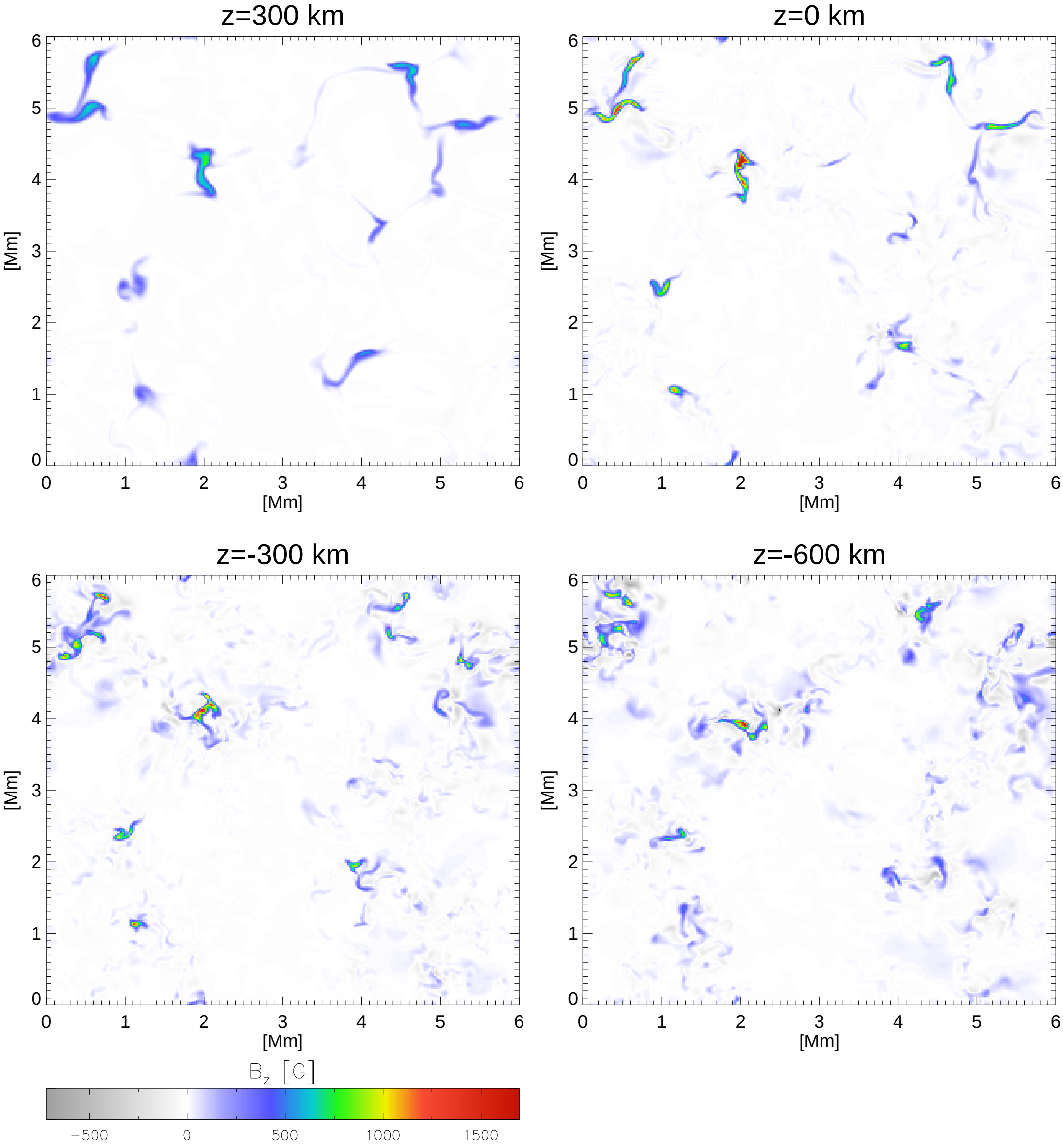

Figure 5.23: *Horizontal cuts of vertical magnetic field at four different height levels for the 10-G run. The isolated magnetic field concentrations visible at* $z = 0$ *approximately maintain their horizontal positions throughout the whole depth of the computational box.*

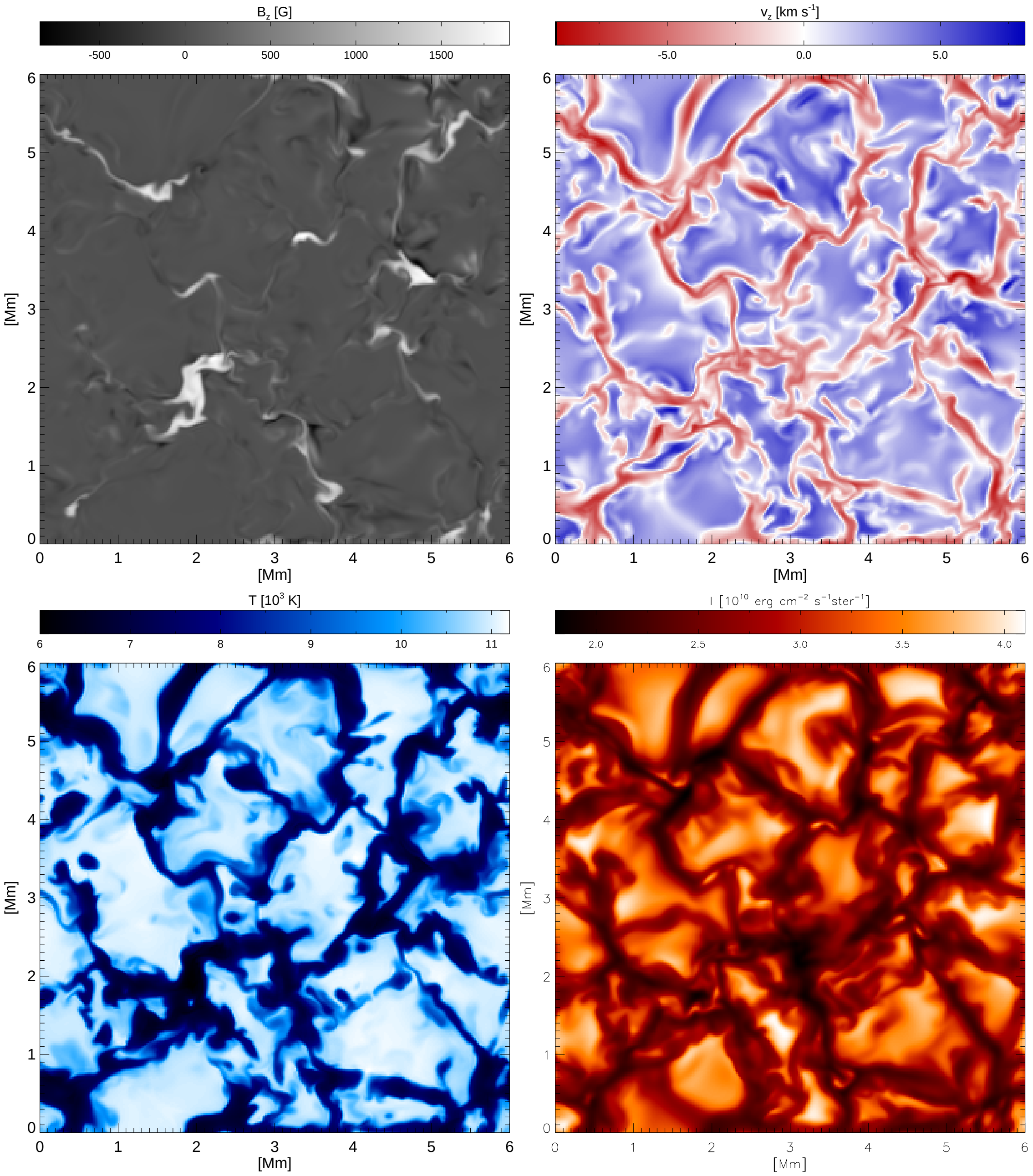

Figure 5.24: *Map of frequency-integrated intensity (lower right) and horizontal cuts at the the average geometrical height corresponding to optical depth unity of (clockwise from bottom left) temperature, vertical magnetic field and vertical velocity for the run with an average field strength of 50 G.*

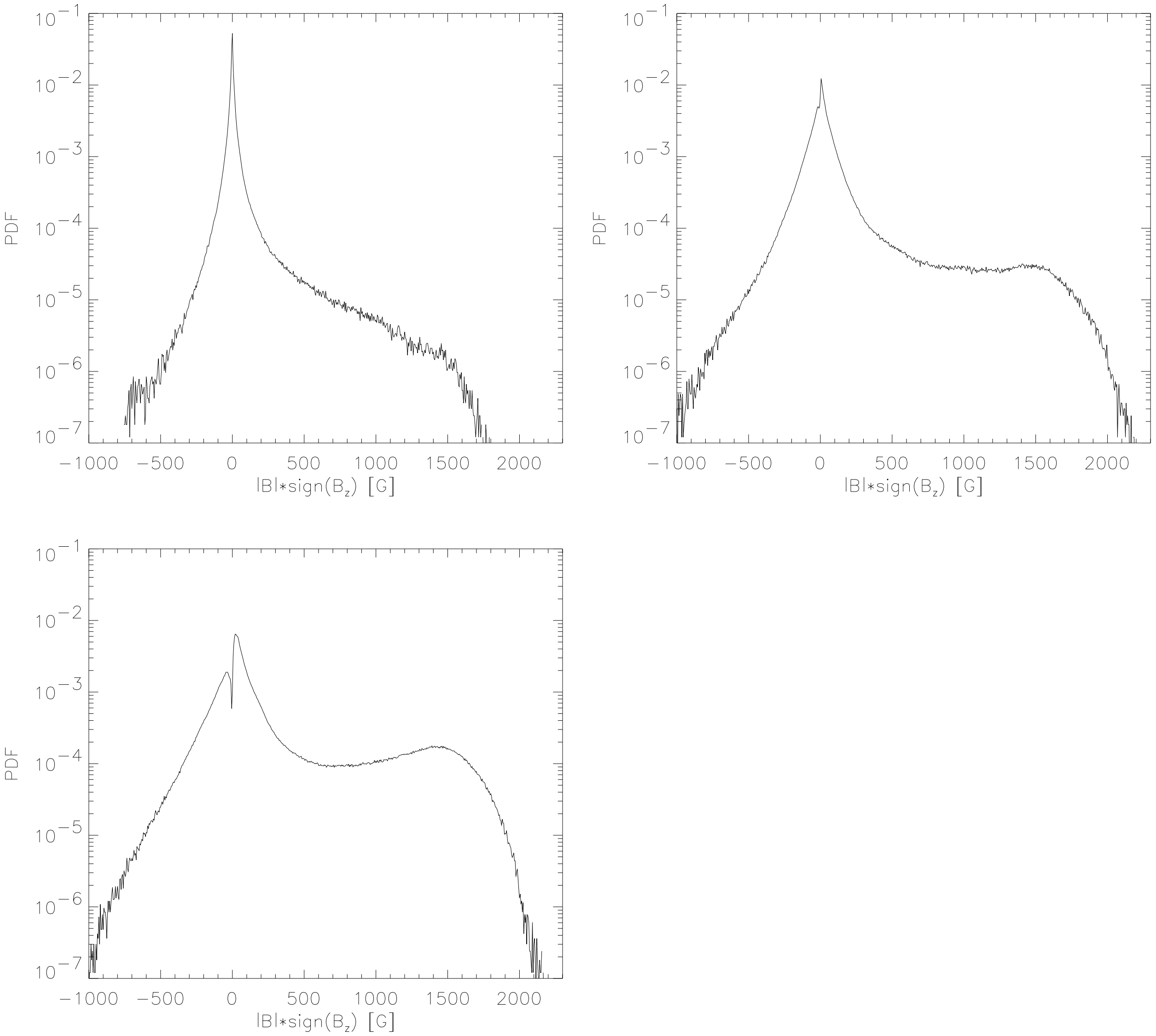

Figure 5.25: *Probability distribution functions for the magnetic field, for all three magnetoconvection runs. Top left: 10-G run; Top right: 50-G run; Bottom left: 200-G run.*

5.3 Effects of non-grey radiative transfer

Since a large part of the total computational resources required by the simulation code is consumed by the calculation of the non-grey radiative heating rate (roughly 80 percent of the total computing time is spent in the radiative transfer routines), it seems worthwhile to assess the significance of the non-grey treatment for the simulation results. For this purpose, this section discusses some differences between grey and non-grey simulation results. The comparison is based on the 200-G case which was simulated once using the four-bin model (the results of which have been presented in Sec. 5.1) and once using a grey radiative transfer with the Rosseland mean opacity All other simulation parameters are identical.

When comparing the two simulations, it turns out that the morphology and time evolution of the magnetic field and the granular pattern are very similar in both runs. This is plausible since the structure of the magnetic field is mainly determined by its interaction with the convective flows in the layers around and below the surface ($z \lesssim 0$), where the differences between the two radiative transfer models are marginal. In both cases the radiative cooling at the surface level around $z = 0$ acts in similar ways as the main driver of convection, resulting in similar convective flow fields.

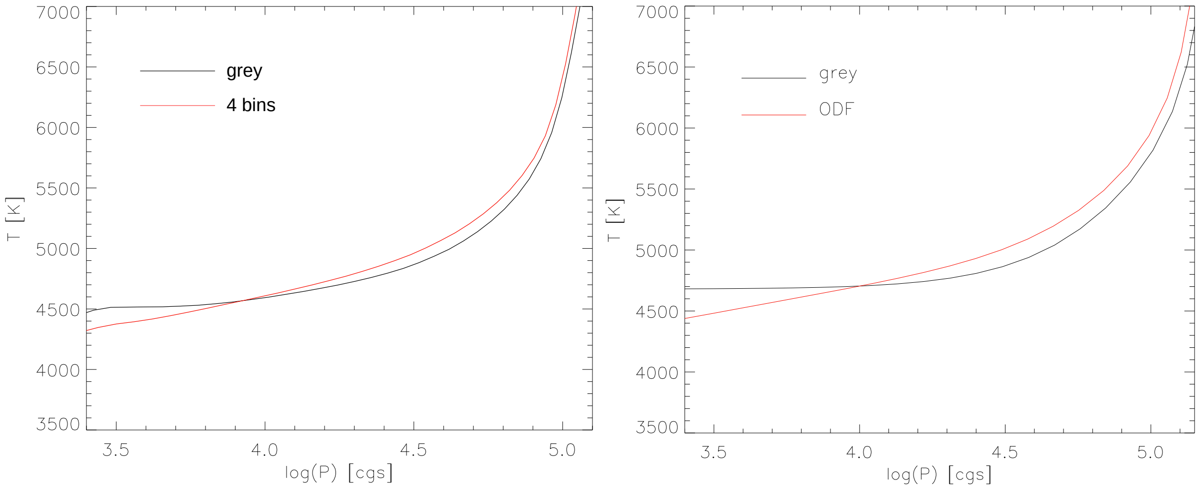

Figure 5.26: *Left panel: Average vertical temperature profiles for the 200-G simulation runs with grey and four-bin radiative transfer, respectively. Right panel: temperature profiles of plane-parallel solar model atmospheres obtained from the ATLAS9 code, using Rosseland opacities and Opacity Distribution Functions, respectively.*

Significant differences are expected to occur in the upper part of the computational domain above $\tau_{\mathrm{Ross}} = 1$, where the frequency bins corresponding to line opacities contribute strongly to the total radiative heating rate. As mentioned in Chapter 4, the essential non-grey effects in plane-parallel model atmospheres are the "line-cooling" and "backwarming" effects. Fig. 5.26 (left panel) shows the horizontally averaged temperature profiles of the grey and non-grey simulation runs, with the corresponding profiles from ATLAS9 plane-parallel atmospheres (right panel) for comparison. The simulations show the same qualitative difference due to the non-grey treatment as the 1D models, the transition from backwarming to line-cooling occuring in both cases at the height level corresponding to $p = 10^4$ dyn cm^{-2}. However, in the uppermost 4-5 grid layers of the simulation box (lying outside the height range covered in Fig. 5.26) the tempertature profile of the grey run does not remain constant as in the corresponding 1D model, but drops to a temperature of 4300 K at the top of the box. This is probably caused by the rather unrealistic closed upper boundary condition, since adiabatic expansion and compression of the gas occuring near the boundary can be expected to have a strong influence on the temperature structure there.

As Fig. 5.27 shows, the non-grey treatment strongly affects the temperature fluctuations in the upper parts of the computational domain. For the grey case, the rms temperature fluctuations on a given geometrical height level increase significantly with height above $z = 300$ km; in magnetic flux concentrations (right panel) the effect is more pronounced than in less magnetized regions (left panel). The fluctuations of the non-grey case remain more or less constant for $z \geq 300$ km, with a slight increase in more strongly magnetized regions above $z = 500$ km. Fig. 5.28 shows the temperature distributions of both simulation runs at a height of 400 km above $z = 0$, in weak-field (left panel) and strong-field (right panel) regions, respectively. The difference between the two models can be explained by the fact that the Rosseland approximation underestimates the effect of line opacities, resulting in radiative energy exchange rates which are much too small in the optically thin parts of the photosphere. On the other hand, the opacity binning yields a much more adequate representation of line opacities. In this case, radiation field and plasma are much more strongly coupled in the upper parts of the simulation box and radiative energy exchange smoothes temperature fluctuations more efficiently. The stronger fluctuations in the grey case *inside* magnetic flux concentrations are a result of the partial evacuation which further reduces the radiative energy exchange. The increase of temperature fluctuations above $z = 500$ km for the non-grey simulation run (right panel of Fig. 5.27) could be related to the strong vortical flows occuring inside magnetic structures at that height, which were discussed in Sec. 5.1.1. On the other hand, the $\tau = 1$ level of the highest opacity bin – which is located near the top of the box in non-magnetic regions – is significantly depressed inside magnetic flux concentrations. Therefore, those strong lines, which reach $\tau = 1$ in the partly evacuated magnetic regions near the top boundary, might not be well represented by the four-bin model. For this reason, it tends to underestimate the radiative energy exchange there, which in turn may explain the increase of temperature fluctuations.

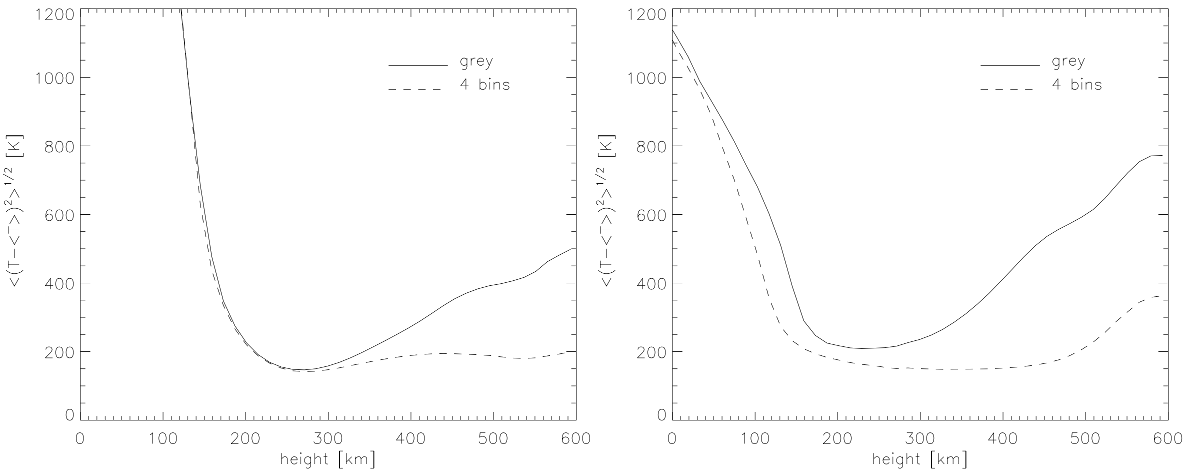

Figure 5.27: *Vertical profiles of horizontal temperature fluctuations for the grey and non-grey simulation runs for the height range above $z = 0$. Left: fluctuations in weak-field regions with $|\mathbf{B}| < 250$ G; Right: same in strong-field regions with $|\mathbf{B}| > 250$ G. The non-grey radiative energy exchange strongly reduces temperature fluctuations in the upper layers of the computational domain, particularly so in regions of strong magnetic field.*

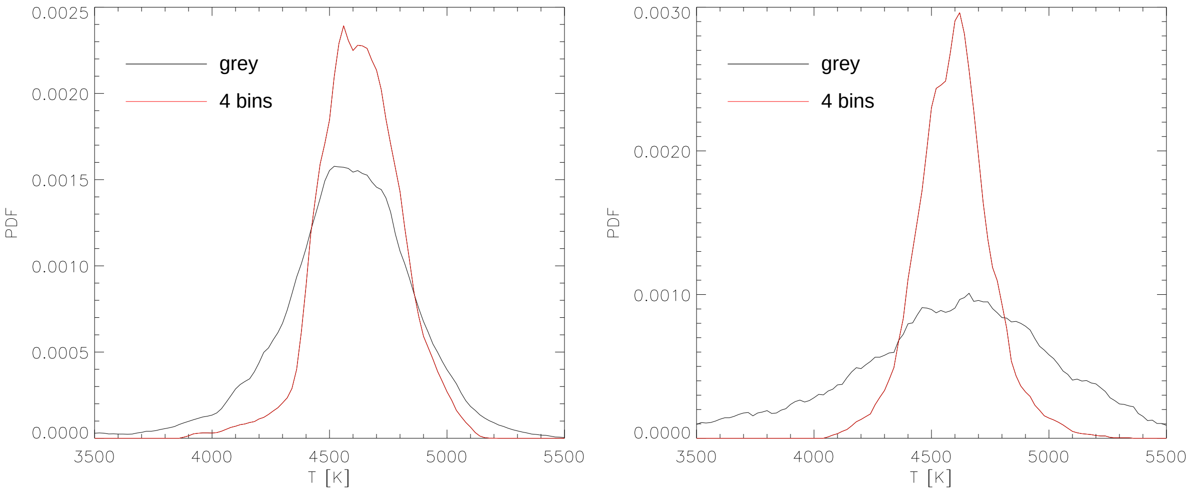

Figure 5.28: *Temperature distribution (PDF) at a height of 400 km above $z = 0$. Left: distribution in weak-field regions with $|\mathbf{B}| < 250$ G; Right: same in strong-field regions with $|\mathbf{B}| > 250$ G.*

It is plausible that the choice of the radiative transfer model affects the appearance of the simulated structure in intensity pictures. The average rms intensity contrast of the four-bin simulation is reduced to 15 percent compared to the value of 18 percent for the grey run. As the comparison of radiance maps in Fig. 5.29 suggests, the lower contrast is mainly the result of a reduced brightness of granules.[3] Since the intensities of the bright magnetic structures are largely unaffected, these features gain in contrast relative to the non-magnetic regions and thus stand out much more clearly against the granular pattern. This impression from a single snapshot is corroborated by Fig. 5.30, which shows the correlation diagrams of intensity versus magnetic field strength at $z = 0$ for both runs, each based on one hour of simulated solar time. Owing to the smaller intensity variations in the weak-field part of the non-grey distribution (right panel), the brightest magnetic features with field strengths around 2000 G are brighter than the granules, while this is not true in the grey case.

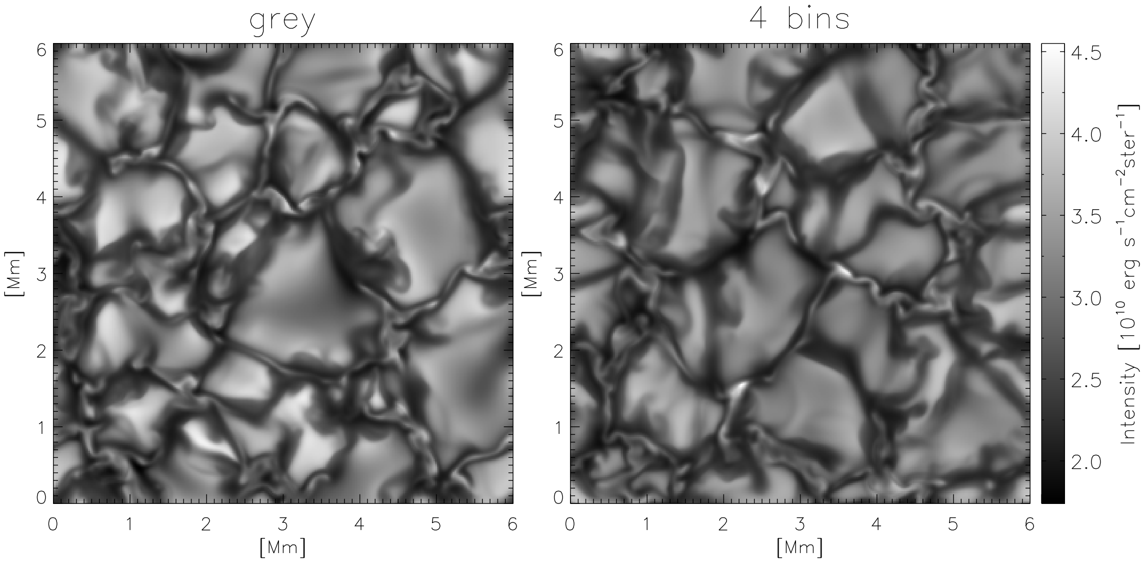

Figure 5.29: *Maps of frequency-integrated intensity for the grey (left) and non-grey (right) simulation runs, using the same greyscale table for both pictures. In the non-grey case granules are darker and the overall contrast is reduced. As a result, bright magnetic features stand out more prominently.*

The finding that the effect of non-grey radiative transfer on the intensity of granules is stronger that its effect on magnetic elements can be understood in terms of the respective temperatures, at which the gas radiates. Fig. 5.31 shows a

---

[3] While the non-grey intensity map of *vertical* rays is clearly darker, this does not necessarily imply that less energy is radiated away at the top of the box, since oblique rays also contribute to the total energy flux. In fact, in both simulation runs the same value for the radiative energy flux is obtained.

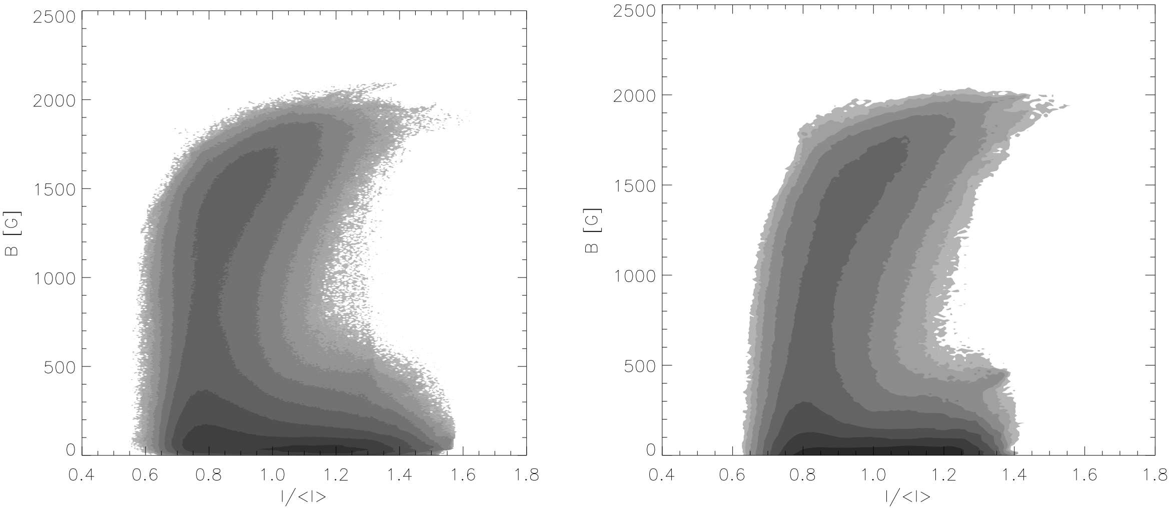

Figure 5.30: *Correlation diagrams (joint PDFs) of magnetic field strength at* $z = 0$ *versus emergent intensity for the 200-G runs. Left: simulation run with grey radiative transfer. Right: run with four-bin opacity binning. The non-grey radiative transfer reduces the contrast of the nonmagnetic regions, thus enhancing the contrast of magnetic elements relative to the granules.*

scatterplot of temperature versus magnetic field strength on the $\tau_{\mathrm{Ross}} = 1$ isosurface for the grey run. Since it is the temperature distribution on this isosurface, which basically determines the radiance, this diagram is similar to the left panel of Fig. 5.30. In the non-grey case, the emerging intensity originates from four different height ranges defined by the respective $\tau = 1$ levels for the four opacity bins. As can be seen from the corresponding scatterplots (Fig. 5.32), the lowest ("continuum") bin (BIN0, top left) radiates with a temperature distribution that is similar to the grey Rosseland case, except for a roughly uniform temperature increase of approximately 200 K, which reflects the backwarming effect. The temperature distributions on the $\tau = 1$ isosurfaces of the line-opacity bins (BIN1 to BIN3), however, show that the temperature at which the bright non-magnetic granules radiate drops drastically from 6900 K for BIN0 to 5000 K for the strongest bin (BIN3), summing up to a total intensity which is lower than in the grey case. Inside magnetic structures, however, the vertical temperature gradient is significantly smaller (see Fig. 5.15 in Sec. 5.1.2), so the brightest magnetic elements radiate at much higher temperatures for the higher opacity bins. The resulting integrated intensity therefore exceeds that of the granules.

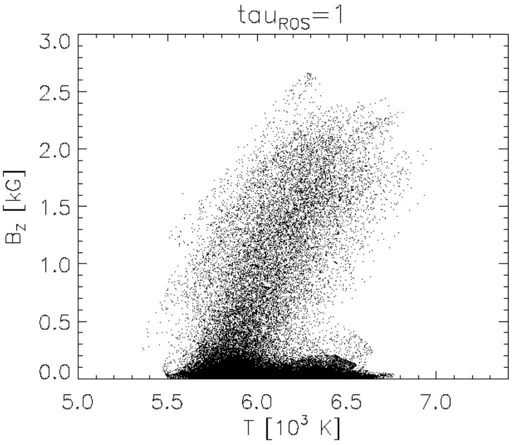

Figure 5.31: *Scatterplot of temperature against magnetic field strength on the isosurface $\tau_{\rm Ross} = 1$ for the simulation run with grey radiative transfer.*

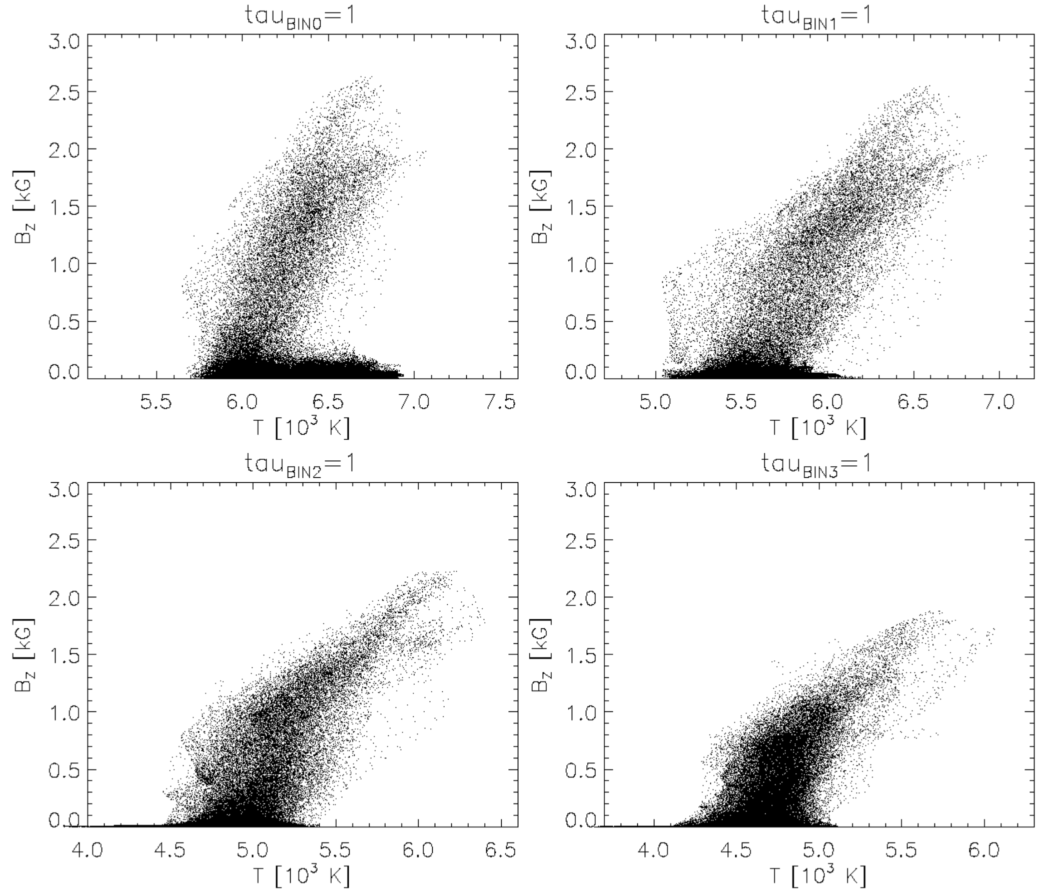

Figure 5.32: *Scatterplots of temperature against magnetic field strength on $\tau = 1$ isosurfaces for the four opacity bins of the non-grey simulation run. Top left: frequency bin representing continuum opacities ("BIN0"). The other three panels correspond to the line-opacity bins named "BIN1" to "BIN3" in ascending order of strength.*

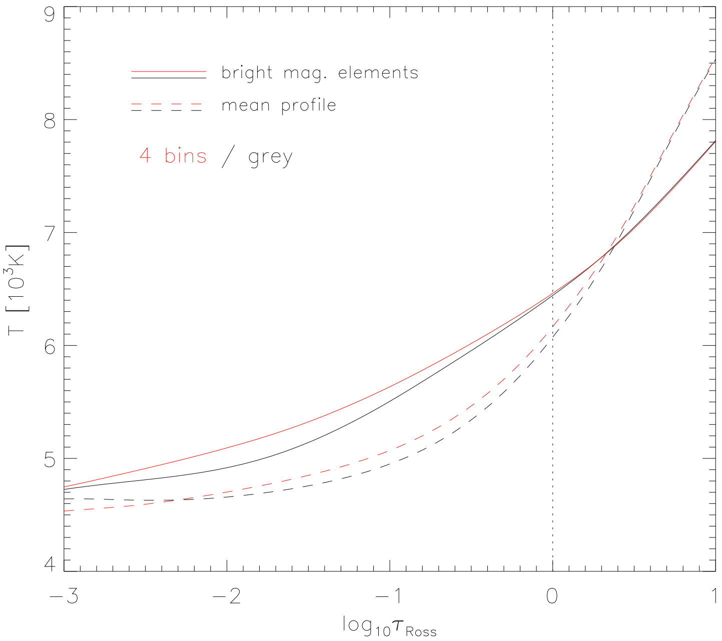

Figure 5.33: *Solid lines: vertical temperature profiles inside magnetic structures with above-average brightness. Dashed lines: mean temperature profiles of the whole simulated domain. Red lines correspond to the non-grey simulation run, black ones to the grey run.*

The increase in temperature in the upper layers of magnetic structures relative to non-magnetic regions at the same optical depth level is a result of heating by radiation from the hot bottom and walls of the magnetic flux concentrations. This effect, termed *radiative illumination*, was already described by Knölker et al. (1991), who carried out simulations of two-dimensional magnetic flux sheets including a grey radiative transfer. Fig. 5.33 illustrates the influence of the non-grey radiative transfer on the radiative illumination in the 200-G simulations. The solid lines show the mean vertical temperature profiles inside bright magnetic elements as function of the Rosseland optical depth; the mean profiles of the whole domain (dashed lines) are shown for comparison. In the optical depth range between $\log_{10}\tau_{\rm Ross} = 0$ and $\log_{10}\tau_{\rm Ross} = -3$, the average temperature inside magnetic field concentrations of the non-grey simulation is clearly higher than in the grey case. The effect is most pronounced around $\log_{10}\tau_{\rm Ross} = -1.5 \sim -2.0$, where the temperature difference between the two cases reaches 200 K. It is caused by the enhanced absorption of incident "hot" radiation in the layers above $\tau = 1$ due to the line opacities accounted for in the non-grey model (i.e., the "backwarming" effect inside magnetic structures). As a result, the temperature increase of bright magnetic structures relative to the mean temperature profile (dashed lines) around $\log_{10}\tau_{\rm Ross} \approx -2.0$ of approximately 400 K for the non-grey case is considerably larger than the corresponding temperature contrast of 250 K for the grey case. Therefore one expects that the non-grey radiative transfer will enhance the intensity contrast of bright magnetic elements relative to the average brightness in intensity maps obtained from the spectral line diagnostics of temperature-sensitive absorption lines originating at an optical depth of about $\log_{10}\tau_{\rm Ross} = -2.0$.

Chapter 6

Outlook

The first simulation results of the newly developed code look promising and suggest that this code can be used to tackle a variety of problems connected with magneto-convective processes in the solar photosphere and convection zone:

- One obvious further step is the extension of the magneto-convection simulations discussed here to the strong- and weak-field regimes. In the strong-field regime, simulations of magnetically dominated convection can clarify the dynamics and energy transport in sunspot umbrae and may help to understand the nature of umbral dots.

- Simulations in the dynamo regime with zero mean field should provide us with some insight as to whether the turbulent fast-dynamo action observed by Cattaneo et al. (2003) in idealized Boussinesq magneto-convection can be expected to work in the strongly stratified surface layers of the convection zone. This problem is, however, numerically challenging, since magnetic Reynolds numbers of the order of 10^3 are necessary to sustain fast dynamo action, and accordingly high spatial resolution is required.

- Numerical experiments of strong, isolated magnetic flux concentrations embedded in convection can possibly give insight into the formation and structure of penumbrae and into the processes which determine the transition from a pore to a small sunspot with increasing size of the magnetic structure.

- Simulations in boxes of greatly extended horizontal dimensions of the order of 50 Mm, possibly at a reduced grid resolution, can be used to study the properties of the "meso-granular" network, which invariably forms in magneto-convective simulations, and possibly identify the mechanisms behind it.

Furthermore, the code serves as a basis for modified and enhanced versions, which will extend the applicability of the code to the layers above and below the photosphere.

- The code presently uses an equidistant grid in all directions. The vertical resolution is determined by the requirement to resolve the small pressure scale heights in the photsphere. Thus, the significantly larger pressure scale heights in the underneath layers are effectively overresolved. The development of a version with a non-equidistant grid in the vertical direction, with the vertical grid spacing scaling as the pressure scale height, will allow to extend the simulation into deeper subphotospheric layers. A possible application is the consistent simulation of the rise of a magnetic flux tube through the upper convection zone and its subsequent eruption into the atmospheric layers.

- The extension of the simulations to chromospheric heights is a somewhat more challenging task. Since the radiative energy exchange is dominated by a few strong specral lines, it will be necessary to modify the radiative transfer to include non-LTE effects. Furthermore, the time scales of ionization and dissoziation are large compared to the dynamical time scales. As a result, the assumption of statistical equilibrium is no longer valid, and the time dependent rate equations, which determine the population numbers of the excitation states of the ions, need to be solved explicitly. Since the uppermost layers of the computational domain are strongly influenced by the choice of the boundary conditions at the top of the box, the development of a transmitting upper boundary condition is mandatory.

References

Baschek, B., Grueber, C., von Waldenfels, W., and Wehrse, R. (1997). Radiation hydrodynamics with many spectral lines. Analytical expressions for a differentially moving slab. *Astron. Astrophys.*, 320:920–928.

Bercik, D. J., Basu, S., Georgobiani, D., Nordlund, A., and Stein, R. F. (1998). Solar Magneto-Convection. In *ASP Conf. Ser. 154: Cool Stars, Stellar Systems, and the Sun*, pages 568–572.

Bruls, J. H. M. J., Vollmöller, P., and Schüssler, M. (1999). Computing radiative heating on unstructured spatial grids. *Astron. Astrophys.*, 348:233–248.

Carlson, B. G. (1963). The numerical theory of neutron transport. In *Alder B., Fernbach S. (eds.) Methods in Computational Physics*, pages 1–42.

Cattaneo, F. (1999). On the Origin of Magnetic Fields in the Quiet Photosphere. *Astrophys. J., Lett.*, 515:L39–L42.

Cattaneo, F., Emonet, T., and Weiss, N. (2003). On the interaction between convection and magnetic fields. *Astrophys. J.*, 588:1183–1198.

Cattaneo, F., Lenz, D., and Weiss, N. (2001). On the Origin of the Solar Mesogranulation. *Astrophys. J., Lett.*, 563:L91–L94.

Caunt, S. E. and Korpi, M. J. (2001). A 3D MHD model of astrophysical flows: Algorithms, tests and parallelisation. *Astron. Astrophys.*, 369:706–728.

Chandrasekhar, S. (1961). *Hydrodynamic and hydromagnetic stability.* International Series of Monographs on Physics, Oxford: Clarendon, 1961.

Choudhuri, A. R. (1998). *The physics of fluids and plasmas : an introduction for astrophysicists.* Cambridge University Press.

Dedner, A. and Vollmöller, P. (2002). An Adaptive Higher Order Method for Solving the Radiation Transport Equation on Unstructured Grids. *Journal of Computational Physics*, 178:263–289.

Deinzer, W., Hensler, G., Schüssler, M., and Weisshaar, E. (1984a). Model calculations of magnetic flux tubes. I - Equations and method. *Astron. Astrophys.*, 139:426–434.

Deinzer, W., Hensler, G., Schüssler, M., and Weisshaar, E. (1984b). Model Calculations of Magnetic Flux Tubes. II - Stationary Results for Solar Magnetic Elements. *Astron. Astrophys.*, 139:435–449.

Dunn, R. B. and Zirker, J. B. (1973). The Solar Filigree. *Sol. Phys.*, 33:281–304.

Emonet, T. and Cattaneo, F. (2001). Small-Scale Photospheric Fields: Observational Evidence and Numerical Simulations. *Astrophys. J., Lett.*, 560:L197–L200.

Gadun, A. S., Solanki, S. K., Sheminova, V. A., and Ploner, S. R. O. (2001). A formation mechanism of magnetic elements in regions of mixed polarity. *Sol. Phys.*, 203:1–7.

Galloway, D. J., Proctor, M. R. E., and Weiss, N. O. (1977). Formation of intense magnetic fields near the surface of the sun. *Nature*, 266:686–689.

Grossmann-Doerth, U., Knölker, M., Schüssler, M., and Solanki, S. K. (1994). The deep layers of solar magnetic elements. *Astron. Astrophys.*, 285:648–654.

Grossmann-Doerth, U., Schüssler, M., and Solanki, S. K. (1989). Stokes V asymmetry and shift of spectral lines. *Astron. Astrophys.*, 221:338–341.

Grossmann-Doerth, U., Schüssler, M., and Steiner, O. (1998). Convective intensification of solar surface magnetic fields: results of numerical experiments. *Astron. Astrophys.*, 337:928–939.

Gustafsson, B., Bell, R. A., Eriksson, K., and Nordlund, A. (1975). A grid of model atmospheres for metal-deficient giant stars. I. *Astron. Astrophys.*, 42:407–432.

Hirsch, C. (1988). *Numerical Computation of Internal and External Flows.* John Wiley & Son Ltd.

Hurlburt, N. E. and Toomre, J. (1988). Magnetic fields interacting with nonlinear compressible convection. *Astrophys. J.*, 327:920–932.

Irwin, A. W. (1981). Polynomial partition function approximations of 344 atomic and molecular species. *Astrophys. J., Suppl. Ser.*, 45:621–633.

Knölker, M., Grossmann-Doerth, U., Schüssler, M., and Weisshaar, E. (1991). Some developments in the theory of magnetic flux concentrations in the solar atmosphere. *Advances in Space Research*, 11:285–295.

Knölker, M. and Schüssler, M. (1988). Model calculations of magnetic flux tubes. IV - Convective energy transport and the nature of intermediate size flux concentrations. *Astron. Astrophys.*, 202:275–283.

Knölker, M., Schüssler, M., and Weisshaar, E. (1988). Model calculations of magnetic flux tubes. III - Properties of solar magnetic elements. *Astron. Astrophys.*, 194:257–267.

Komm, R., Mattig, W., and Nesis, A. (1991). The height dependence of velocity-intensity fluctuations and several non-dimensional parameters in the solar photosphere. *Astron. Astrophys.*, 252:812–820.

Kunasz, P. B. and Auer, L. H. (1988). Short characteristic integration of radiative transfer problems - Formal solution in two-dimensional slabs. *Journal of Quantitative Spectroscopy and Radiative Transfer*, 39:67–79.

Kunasz, P. B. and Olson, G. L. (1988). Short characteristic solution of the non-LTE line transfer problem by operator perturbation. II - The two-dimensional planar slab. *Journal of Quantitative Spectroscopy and Radiative Transfer*, 39:1–12.

Kurucz, R. (1993). ATLAS9 Stellar Atmosphere Programs and 2 km/s grid. *ATLAS9 Stellar Atmosphere Programs and 2 km/s grid. Kurucz CD-ROM No. 13. Cambridge, Mass.: Smithsonian Astrophysical Observatory, 1993.*, 13.

Lowan, A. N., Davids, and Levenson (1942). . *Bull. Amer. Math. Soc.*, 48:739.

Ludwig, H. G. (1992). *Nichtgrauer Strahlungstransport in numerischen Simulationen stellarer Konvektion.* PhD thesis, Universität Kiel.

Ludwig, H.-G., Jordan, S., and Steffen, M. (1994). Numerical simulations of convection at the surface of a ZZ Ceti white dwarf. *Astron. Astrophys.*, 284:105–117.

Maltby, P., Avrett, E. H., Carlsson, M., Kjeldseth-Moe, O., Kurucz, R. L., and Loeser, R. (1986). A new sunspot umbral model and its variation with the solar cycle. *Astrophys. J.*, 306:284–303.

Mihalas, D. (1967). The calculation of model stellar atmospheres. In *Alder B., Fernbach S. (eds.) Methods in Computational Physics*, pages 1–51.

Mihalas, D. (1978). *Stellar atmospheres (2nd edition).* San Francisco, W. H. Freeman and Co., 1978. 650 p.

Mihalas, D., Auer, L. H., and Mihalas, B. R. (1978). Two-dimensional radiative transfer. I - Planar geometry. *Astrophys. J.*, 220:1001–1023.

Nordlund, A. (1982). Numerical simulations of the solar granulation. I - Basic equations and methods. *Astron. Astrophys.*, 107:1–10.

Nordlund, A. (1983). Numerical 3-D simulations of the collapse of photospheric flux tubes. In *IAU Symp. 102: Solar and Stellar Magnetic Fields: Origins and Coronal Effects*, pages 79–83.

Nordlund, Å. and Stein, R. F. (1990). Solar Magnetoconvection. In *IAU Symposium No. 138*, pages 191–211.

Olson, G. L. and Kunasz, P. B. (1987). Short characteristic solution of the non-LTE line transfer problem by operator perturbation. I. *Journal of Quantitative Spectroscopy and Radiative Transfer*, 38:325.

Parker, E. N. (1963). Kinematical Hydromagnetic Theory and its Application to the Low Solar Photosphere. *Astrophys. J.*, 138:552–575.

Parker, E. N. (1978). Hydraulic concentration of magnetic fields in the solar photosphere. VI - Adiabatic cooling and concentration in downdrafts. *Astrophys. J.*, 221:368–377.

Ploner, S. R. O., Solanki, S. K., and Gadun, A. S. (1999). The evolution of solar granules deduced from 2-D simulations. *Astron. Astrophys.*, 352:679–696.

Proctor, M. R. E. (1992). Magnetoconvection. In *NATO ASIC Proc. 375: Sunspots. Theory and Observations*, pages 221–241.

Proctor, M. R. E. and Weiss, N. O. (1982). Magnetoconvection. *Reports of Progress in Physics*, 45:1317–1379.

Rast, M. P., Nordlund, A., Stein, R. F., and Toomre, J. (1993). Ionization effects in three-dimensional solar granulation simulations. *Astrophys. J., Lett.*, 408:L53–L56.

Rast, M. P. and Toomre, J. (1993a). Compressible Convection with Ionization. I. Stability, Flow Asymmetries, and Energy Transport. *Astrophys. J.*, 419:224–239.

Rast, M. P. and Toomre, J. (1993b). Compressible Convection with Ionization. II. Thermal Boundary-Layer Instability. *Astrophys. J.*, 419:240–254.

Schüssler, M. (2001). Numerical Simulation of Solar Magneto-Convection. In *ASP Conf. Ser. 236: Advanced Solar Polarimetry – Theory, Observation, and Instrumentation*, pages 343–354.

Sigwarth, M., Balasubramaniam, K. S., Knölker, M., and Schmidt, W. (1999). Dynamics of solar magnetic elements. *Astron. Astrophys.*, 349:941–955.

Sneden, C., Johnson, H. R., and Krupp, B. M. (1976). A statistical method for treating molecular line opacities. *Astrophys. J.*, 204:281–289.

Solanki, S. K. (1989). The origin and the diagnostic capabilities of the Stokes V asymmetry observed in solar faculae and the network. *Astron. Astrophys.*, 224:225–241.

Spruit, H. C. (1974). A model of the solar convection zone. *Sol. Phys.*, 34:277–290.

Spruit, H. C. (1979). Convective collapse of flux tubes. *Sol. Phys.*, 61:363–378.

Steffen, M. (1990). A Simple Method for Monotonic Interpolation in One Dimension. *Astron. Astrophys.*, 239:443–450.

Stein, R. F., Bercik, D., and Nordlund, A. (2002). Solar convection and magneto-convection simulations. *Nuovo Cimento C Geophysics Space Physics C*, 25:513–522.

Stein, R. F. and Nordlund, A. (1998). Simulations of Solar Granulation. I. General Properties. *Astrophys. J.*, 499:914–933.

Steiner, O., Grossmann-Doerth, U., Knölker, M., and Schüssler, M. (1998). Dynamical Interaction of Solar Magnetic Elements and Granular Convection: Results of a Numerical Simulation. *Astrophys. J.*, 495:468–484.

Stix, M. (1989). *The Sun. An Introduction.* Springer-Verlag Berlin Heidelberg New York.

Strom, S. E. and Kurucz, R. (1966). Statistical Procedure for Computing Line-Blanketed Model Stellar Atmospheres. *Astron. J.*, 71:181.

Tao, L., Weiss, N. O., Brownjohn, D. P., and Proctor, M. R. E. (1998). Flux Separation in Stellar Magnetoconvection. *Astrophys. J., Lett.*, 496:L39–L42.

Wehrse, R., Baschek, B., and von Waldenfels, W. (2000). The diffusion of radiation in moving media. I. Basic assumptions and formulae. *Astron. Astrophys.*, 359:780–787.

Weiss, N. O. (1966). The Expulsion of Magnetic Flux by Eddies. *Royal Society of London Proceedings Series A*, 293:310–328.

Weiss, N. O. (1997). Magnetoconvection. In *ASP Conf. Ser. 118: 1st Advances in Solar Physics Euroconference. Advances in Physics of Sunspots*, pages 21–33.

Zwaan, C. (1987). Elements and patterns in the solar magnetic field. *Ann. Rev. Astron. Astrophys.*, 25:83–111.

Danksagung

Die vorliegende Arbeit wurde am Max-Planck-Institut für Aeronomie in Katlenburg-Lindau angefertigt. Den Direktoren des Instituts danke ich für die Bereitstellung eines Arbeitsplatzes und die Gewährung eines Stipendiums.

Mein besonderer Dank gilt Herrn Prof. M. Schüssler für die ausgezeichnete Betreuung der Arbeit, das Zustandekommen der Kooperation mit den "Chicago boys", sowie für die zahlreichen Gespräche, für die er sich stets viel Zeit genommen hat und in denen auch menschliche Belange ihren Platz hatten. Herrn Prof. F. Kneer danke ich für die Übernahme der Betreuung seitens der Universität Göttingen.

Bedanken möchte ich mich bei den Herren Doktores Holzwarth, Preuss, Rempel und Vollmöller sowie allen anderen derzeitigen und ehemaligen Mitgliedern der Kaffeerunde für viele interessante und unterhaltsame Gespräche, die nicht unwesentlich zur Auflockerung des Arbeitsklimas beigetragen haben.

Bei Herrn Dr. J. Bruls möchte ich mich für seine fachliche Unterstützung in sämtlichen Belangen des Strahlungstransports bedanken. Herrn S. Shelyag sei gedankt für die Bereitstellung der Tabellen für die Zustandsgleichung.

I would like to thank Fausto Cattaneo and Thierry Emonet for the opportunity to spent an interesting time at the University of Chicago as well as for many interesting and illuminative discussions about magneto-convection and the turbulent dynamo. Furthermore, I would like to thank Timur Linde for allowing me to build onto his 3D-MHD code, and for answering my numerous questions regarding the code.

Mein größter Dank gilt allerdings meinen Eltern, die mir das Physikstudium ermöglicht haben und mich während all der Jahre unentwegt durch ihren Rat und ihre Anteilnahme unterstützt haben.

Lebenslauf

Geburt:	Am 29.03.1975 in Fulda	
Eltern:	Armin Vögler Gudrun Vögler, geb. Kuh	
Staatsbürgerschaft:	deutsch	
Schulbildung:	8/1981 bis 7/1984	Domschule (Grundschule)
	8/1984 bis 6/1993	Rabanus-Maurus-Schule (Gymnasium)
	6/1993	Abitur
Studium:	10/1993 bis 10/1999	Physikstudium an der Georg-August-Universität Göttingen
	10/1995	Vordiplomprüfung
	9/1998 bis 9/1999	Diplomarbeit: “Zur Wirkung nichtaxialsymmetrischer Geschwindigkeitsfelder auf den Galaxiendynamo”
	10/1999	Diplomprüfung
	11/1999 bis 1/2000	Wissenschaftlicher Mitarbeiter and der Universitäts-Sternwarte Göttingen
	2/2000 bis 6/2003	Doktorarbeit Während dieser Zeit Tätigkeit als wissenschaftlicher Mitarbeiter am Max-Planck-Institut für Aeronomie in Katlenburg-Lindau